DESIGN OF A NOVEL CONDUCTION HEATING BASED STRESS-THERMAL CYCLING APPARATUS FOR COMPOSITE MATERIALS AND ITS UTILIZATION TO CHARACTERIZE COMPOSITE MICROCRACK DAMAGE THRESHOLDS

A Dissertation

by

JAEHYUNG JU

Submitted to the Office of Graduate Studies of
Texas A&M University
in partial fulfillment of the requirements for the degree of

DOCTOR OF PHILOSOPHY

August 2005

Major Subject: Mechanical Engineering

DESIGN OF A NOVEL CONDUCTION HEATING BASED STRESS-THERMAL CYCLING APPARATUS FOR COMPOSITE MATERIALS AND ITS UTILIZATION TO CHARACTERIZE COMPOSITE MICROCRACK DAMAGE THRESHOLDS

A Dissertation

by

JAEHYUNG JU

Submitted to the Office of Graduate Studies of
Texas A&M University
in partial fulfillment of the requirements for the degree of

DOCTOR OF PHILOSOPHY

Approved by:

Chair of Committee,	Roger J. Morgan
Committee Members,	Terry Creasy
	Junuthula N. Reddy
	Michael A. Bevan
Head of Department,	Dennis L. O'Neal

August 2005

Major Subject: Mechanical Engineering

ABSTRACT

Design of a Novel Conduction Heating Based Stress-Thermal Cycling Apparatus for Composite Materials and Its Utilization to Characterize Composite Microcrack Damage Thresholds. (August 2005)

Jaehyung Ju, B.S., Korea Aviation University;

M.S., Korea University

Chair of Advisory Committee: Dr. Roger J. Morgan

The objective of this research was to determine the effect of thermal cycling combined with mechanical loading on the development of microcracks in M40J/PMR-II-50, the second generation aerospace application material. The objective was pursued by finding the critical controlling parameters for microcrack formation from mechanical stress-thermal cycling test.

Three different in-plane strains (0%, 0.175~0.350%, and 0.325~0.650%) were applied to the composites by clamping composite specimens (M40J/PMR-II-50, $[0,90]_s$, a uni-tape cross-ply) on the radial sides of half cylinders having two different radii (78.74mm and 37.96mm). Three different thermal loading experiments, 1) 23^{o}C to –196^{o}C to 250^{o}C, 2) 23^{o}C to 250^{o}C, and 3) 23^{o}C to -196^{o}C, were performed as a function of mechanical in-plane strain levels, heating rates, and number of thermal cycles. The apparatus generated cracks related to the in-plane stresses (or strains) on plies. The design and analysis concept of the synergistic stress-thermal cycling experiment was simplified to obtain

main and interaction factors by applying 2^k factorial design from the various factors affecting microcrack density of M40J/PMR-II-50.

Observations indicate that the higher temperature portion of the cycle under load causes fiber/matrix interface failure. Subsequent exposure to higher stresses in the cryogenic temperature region results in composite matrix microcracking due to the additional stresses associated with the fiber-matrix thermal expansion mismatch.

To my parents, for always being there and having faith in me

To my wife and my daughter, for their love and patience

ACKNOWLEDGEMENTS

I would like to express my deep gratitude and great respect to my chair, Dr. Roger J. Morgan, for providing me with generous financial support, constant academic guidance, and encouragement during the course of my Ph.D. research. I am also grateful to my dissertation committee, Dr. Terry S. Creasy and Dr. J. N. Reddy, for their helpful discussions, suggestions, and technical guidance. Thanks are also extended to Dr. Michael Bevan, Dr. Jaime C. Grunlan, and Dr. Sai Lau for their helpful suggestions and encouragement.

I would like to express my thanks to Dr. Eugene E. Shin at the NASA Glenn Research Center for his assistance in supplying the composite panels. The research funding by the Air Force Office of Scientific Research (Contract No. FA 9550-04-1-0137), under the auspices of Dr. Charles Lee, is also greatly appreciated

I am truly thankful to Dr. Yoonchan Oh, Parag Ravindran, and Suveen Mathaudhu, friends in need, for their constant support and understanding. They have always been there when I needed friends to talk to on almost any topic.

Most of all, I would like to express my gratefulness to all my family members for their support and encouragement. I am deeply thankful to my parents and my sister for their unwavering encouragement and understanding. My loving thanks always go to my beloved wife, Jihyun, and daughter, Haesah, for their everlasting love and support.

TABLE OF CONTENTS

CHAPTER Page

CHAPTER Page

LIST OF TABLES

LIST OF FIGURES

FIGURE Page

FIGURE Page

FIGURE Page

FIGURE Page

CHAPTER I

INTRODUCTION

1.1 Background

Single stage to orbit (SSTO) launch vehicles, used for future space transportation systems, require light weight, low cost structures. Cryogenic fuel, such as liquid hydrogen and liquid oxygen containment structures manufactured by new, high performance polymeric matrix fibrous composites will make the SSTO lighter in weight [1-3]. However, the containment structure will be filled with low temperature fuel (e.g. liquid oxygen: -183^{o}C, liquid hydrogen: -253^{o}C) and drained hundreds of times during testing and flights [4,5]. In addition, these structures may be heated drastically upon reentry due to the friction. With these operational necessities, the fuel and oxidizer storage and transport components were required to sustain an extensive combination of cryogenic and elevated temperature up to 125^{o}C as shown in Figure 1.1 [6].

Moreover, under mechanical loading by fuel pressure and launch gravity force, the cryogenic fuel tanks should endure both large stresses through the layers of the composite in addition to thermal cycling. Therefore, thermal exposure such as thermal cycling combined with mechanical loading can produce significant damage in polymer composites that can change their mechanical properties.

This dissertation follows the style of *Journal of Composite Materials*.

If materials are applied to a satellite structure, they would undergo periods of solar eclipse and sun illumination within a service temperature range from -150 to 150^{o}C as shown in Figure 1.2 [3].

High temperature fiber reinforced composites are used in the fabrication of aerospace structural components due to their excellent thermal performance. One of the examples is a high performance propulsion rocket engine. These composites can encounter thermal cycling exposure during their service lifetime. Typically the components are exposed to rapid heat-up rate (up to 93^{o}C/sec) and to a maximum temperature around 316^{o}C as shown in Figure 1.3 [7].

Therefore, fundamental understanding of the damage mechanism in the fiber reinforced composites under stress-thermal cycling is critical because thermal cycling can result in microcracking of the resin matrix or the interface of matrix and fiber, caused by combined applied stresses and inherent thermal residual stresses that arise from the anisotropy of coefficient of thermal expansion (CTE) in 1) the composite ply and 2) matrix and fibers (Figure 1.4). Degradation of stiffness in the matrix by thermal cycling induced fatigue can be an important factor accelerating microcracking.

In this study, the microcrack susceptibility of fiber reinforced composites used for the cryogenic fuel containment will be characterized for a range of synergistic exposure conditions.

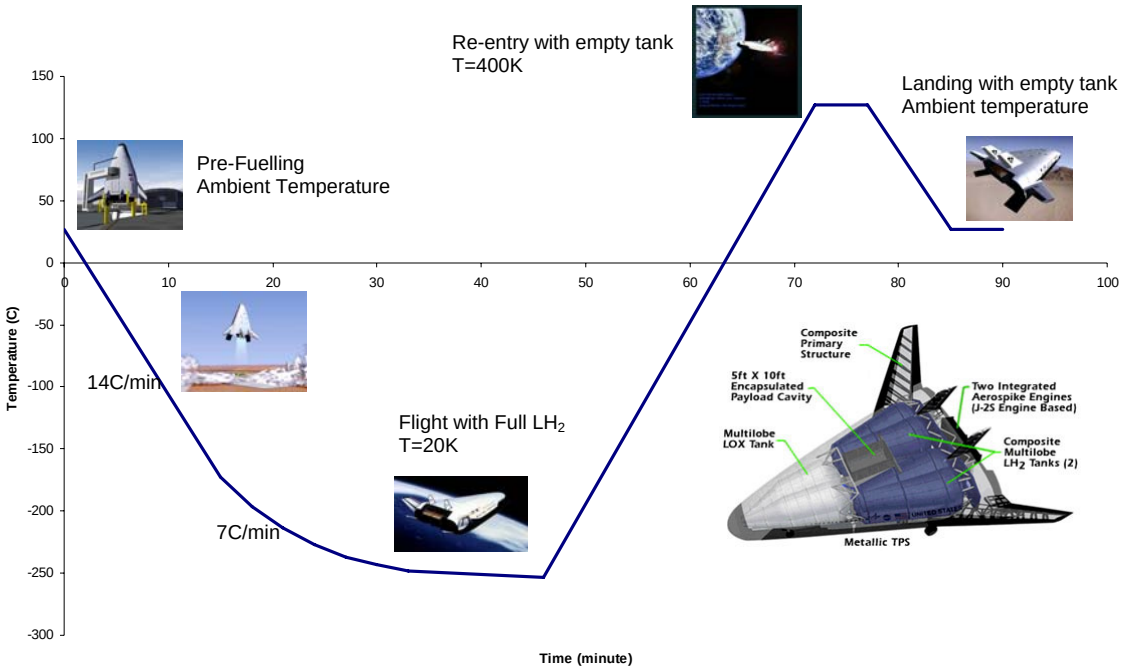

Figure 1.1. *Temperature profile of Reusable Launch Vehicle (RLV)'s fuel tank during its flight cycle [6]*

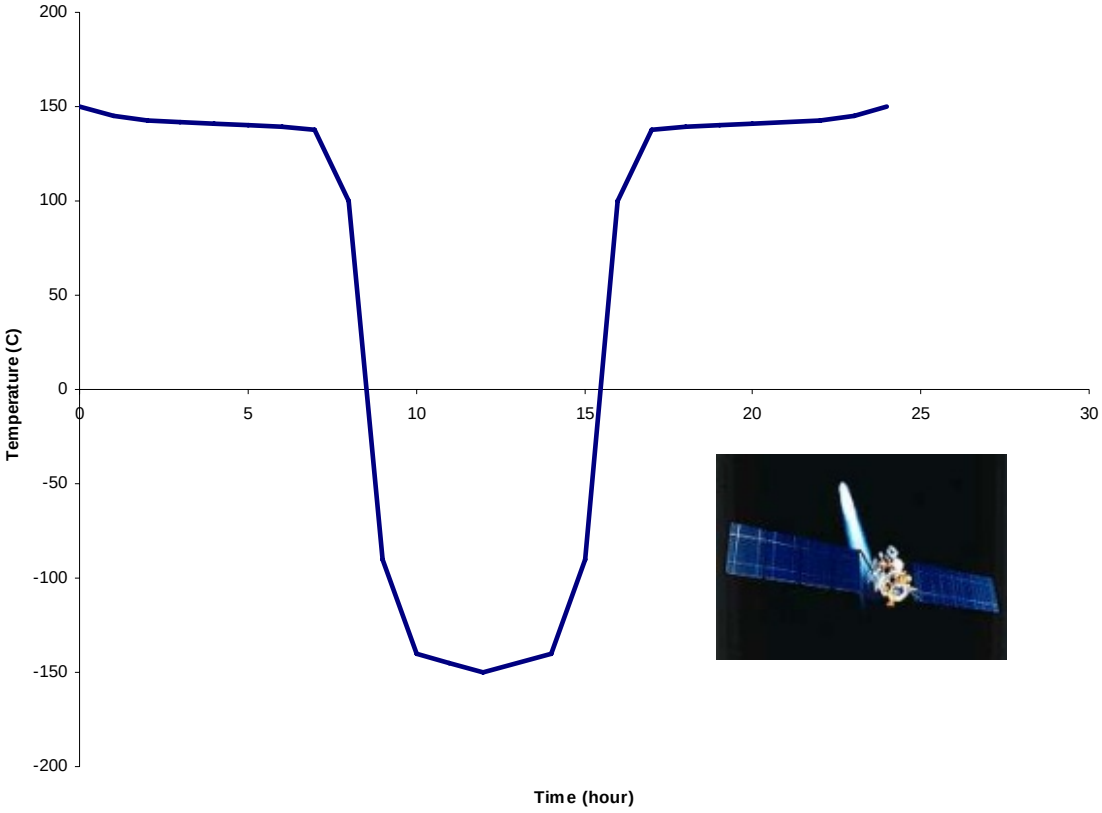

Figure 1.2. *Satellite surface temperature variation [3]*

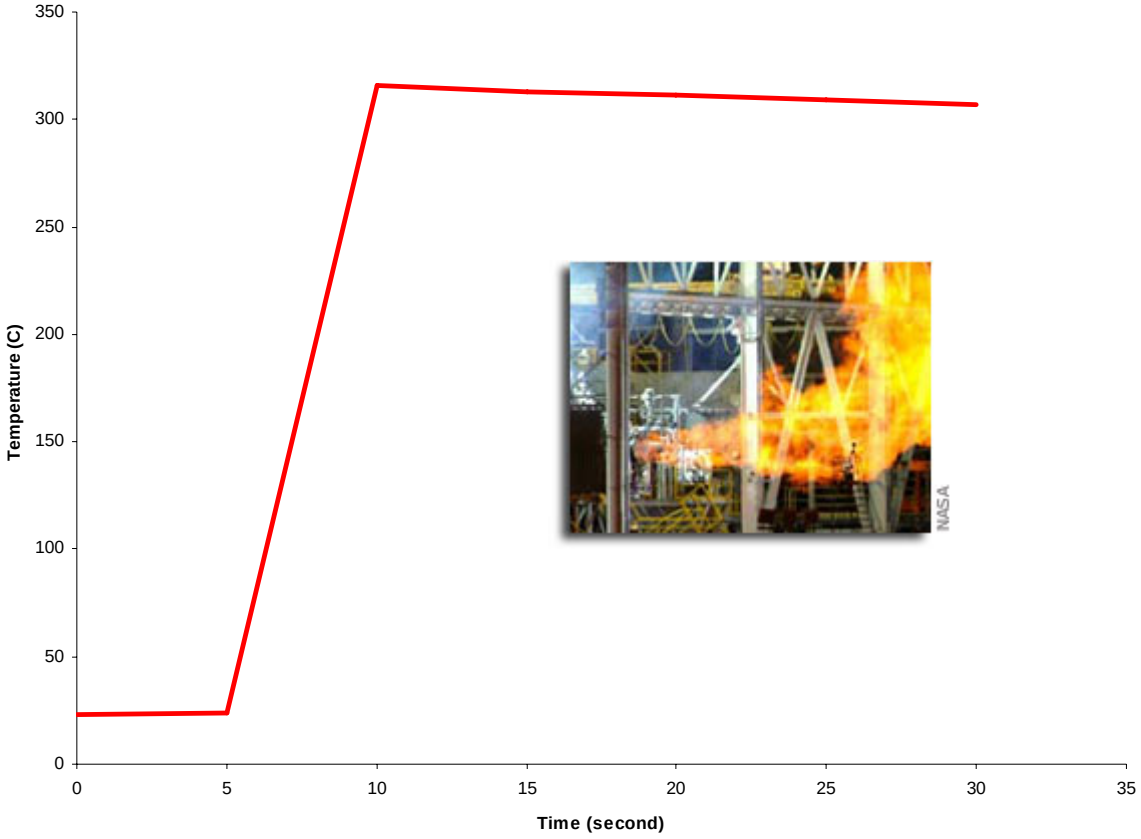

Figure 1.3. *Temperature variation of high performance propulsion rocket engine [7]*

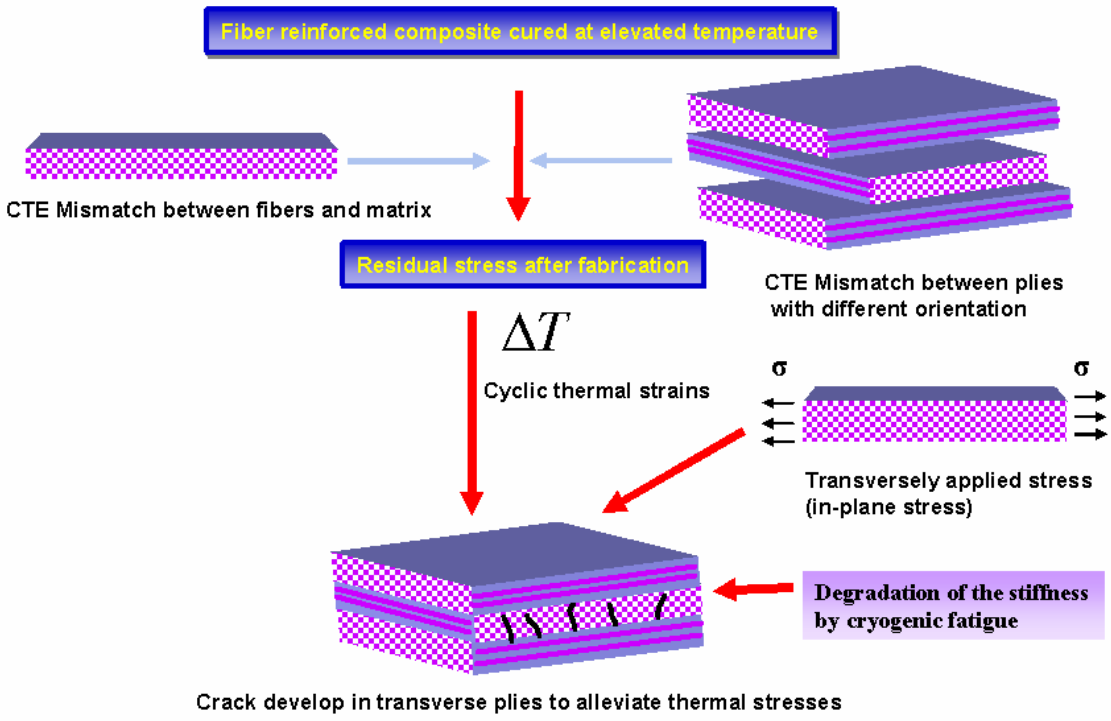

Figure 1.4. *Schematic of damage initiation under thermal exposure combined with mechanical loading*

1.2 Objectives and Scopes

The objectives of this research are 1) design and development of a novel conduction heating based mechanical loading combined thermo-cycling apparatus, and 2) its investigation of utilization to characterize composite microcrack damage thresholds as a function of:

- Thermo-cycling temperature profiles
- The number of thermo-cycles
- The applied in-plane strain level imposed on the composites
- Temperature heating rate

which are vitally needed to ascertain design and materials criteria for future aerospace applications, 3) optimal experimental design of the mechanical loading combined thermo-cycling to identify the initial damage increase with minimum number of the experiments, and its analysis using statistical response surface methodology, 4) development of a methodology and its application to define a precise crack density of composite microstructure, 5) mechanical and thermal analysis for lamina scale levels, and 6) development of the water immersion based non-destructive evaluation (NDE) of crack density for rapid measurement of crack densities.

Characterization of the effect of mechanical loading combined thermal cycling on the initiation and propagation of microcracks in polyimide carbon uni-tape composite materials is outlined in Figure 1.5.

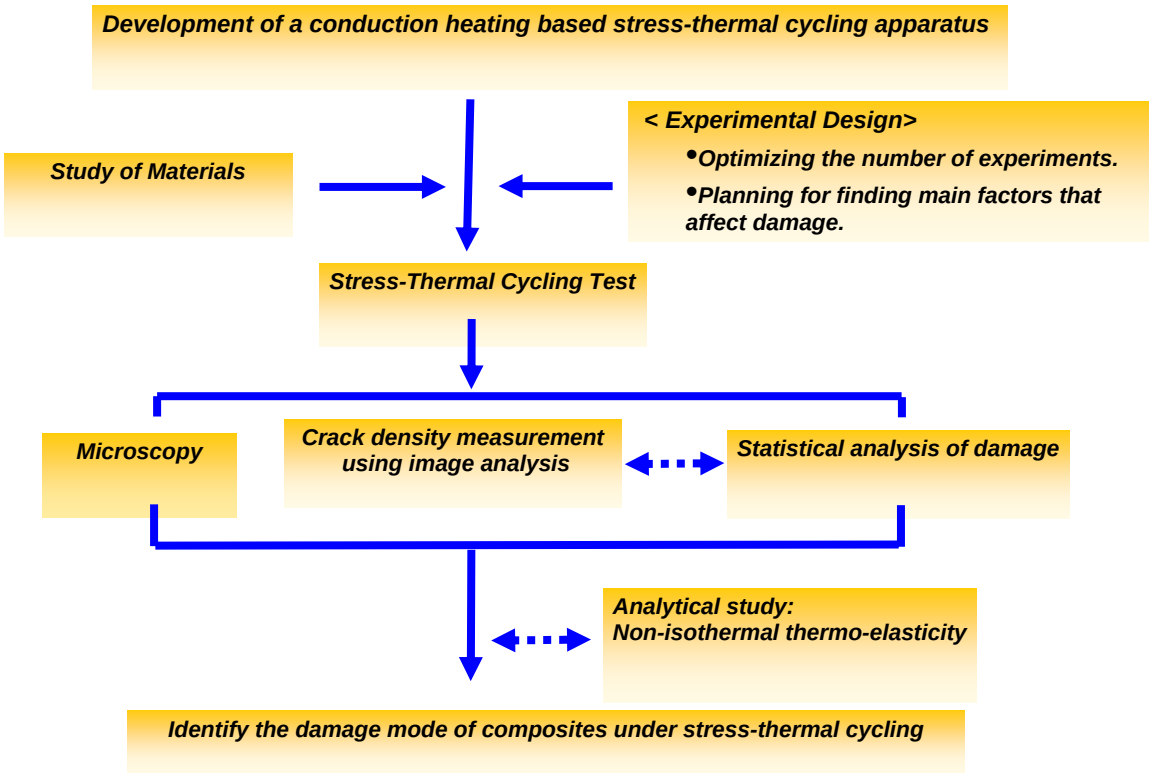

Figure 1.5. *Outline of the research for identifying crack initiation mode under stress-thermal cycling*

CHAPTER II

LITERATURE REVIEW

2.1 Composite Microcracking

Fiber-reinforced composites cured at elevated temperatures contain residual stresses after fabrication because of a mismatch in coefficient of thermal expansion between the fiber and matrix and a mismatch in the coefficient of thermal expansion between plies with different orientations [8,9]. The residual stresses increase as the difference between the operating temperature and the stress-free temperature increases [8]. Initial oxidative and hydrolytic degradation of the exterior surface of the composite matrix can also result in microcracks at the exterior matrix surface [6, 7], whose growth is enhanced by applied load. The synergistic action of thermal and chemical degradation at the microcrack tips with applied load results in propagation of damage further into the composite interior causing interfacial failure between fiber and matrix, resin microcracking and ultimately macroscopic delamination [10-12]. Dmm Microcracking can facilitate oxidation, hydrolytic degradation, and accelerate the degradation of mechanical strength of polymer-matrix composites, by allowing the diffusion of oxygen and moisture to the crack tip.

Thermo-cycling [13-31], mechanical fatigue [32-34], and hygrothermal aging [35-38] on microcrack initiation and growth of polymeric composite materials have been studied. Under uniaxial [39-43] and biaxial [44,45] tensile loading, microscopic stress analysis, to study the microcrack development in laminates, was conducted. While investigating

microcracks under uniaxial or biaxial loading conditions, a study addressing the effects of residual stress on crack propagation has also been performed [9,46,47]. Damage evolution upon loading under thermo-cycling conditions has been characterized [48-50].

2.2 High Temperature Polymer Matrix Composites

Thermosetting composite matrixes have an important role in high temperature composite applications such as both structure and sub-structural components in supersonic aircrafts and missile airframes. Widely used thermosets are i) Epoxy ii) Bismaleimide (BMI) and iii) Polyimide.

Epoxy resins offer high strength, low shrinkage, excellent adhesion to various substrates, effective electrical insulation, chemical and solvent resistance, low cost, and low toxicity. Epoxy resins are of particular interest to the structural engineer because they provide a unique balance of chemical and mechanical properties combined with extreme processing versatility [51].

BMI resins are relatively a young class of thermosetting polymers gaining interest and popularity because they combine a number of unique features including excellent physical properties at elevated temperature (exhibiting good wet and damage tolerance through 177^{o}C) and in wet environments, almost constant electrical properties over a wide range of temperatures, non-flammability properties, excellent processability, and a balance of thermal, mechanical and electrical properties [51].

The addition type polyimide, derived from preformed oligomers, undergo thermal cross linking or chain extension to form a thermoset [51]. A legendary example of the

addition type of polyimide is PMR (*in situ* polymerization of monomer reactants). Due to the durability at high temperature, PMR resins are used in supersonic aircrafts and missile airframes. Anticipated service temperatures of the polyimide are 300 to 350^{o}C or more. They can be employed for up to 1000 hours at 300^{o}C for non-critical and lightly loaded components.

PMR-15 is the first generation PMR type polyimide developed by NASA and is recognized as a state of the art high temperature matrix for service temperatures of up to 300^{o}C for the long times. PMR-15 has many advantages in having overall balance of processing, behavior, thermo-oxidative stability, and retaining of mechanical properties at high temperatures.

Second generation of PMR, PMR-II, was developed to meet the requirements for higher service temperature in advanced supersonic aircrafts structures, tactical missile airframes and jet engines. PMR-II polyimide resins exhibit enhanced service temperature in the range of 360 to 380^{o}C. However, difficulties to process due to high viscosities, volatile by-products, and limited scope of high temperature processing materials and expensive tooling, are shortcomings of PMR-II [52]. PMR-II-50 has been considered for high temperature and high stiffness space propulsion composite applications, such as a face-sheet of various sandwich structures with high stiffness carbon fibers [52]. However, PMR series' high crosslink densities make them fairly brittle and microcracking under repeated heat cycles prone to occur. The microcracking is expected to arise more under a cryogenic temperature exposure because of the accelerated brittle condition at the low temperature.

2.3 Statistical Experimental Design

The methodology of statistical experimental design has been developed for such problems where multiple and many interacting variables make interpretation of the data complex and difficult [53]. Originally, Fisher developed the methodology in the field of agricultural research [54]. The statistical experimental design approach has been successfully applied in many other fields, especially product design, production engineering and quality control [55]. The method is being broadly used in the chemical and drug production field. For example, Wroblewska *et al* used rotatable uniform design for optimizing parameters of epoxidation of allyl alchol [56]. First order factorial design experiment was applied to optimize production of poly (γ-glutamic acid) and the experimental results were fitted with a second order polynomial equation by a multiple regression analysis [57]. Central composite design was applied to both physical-chemical analysis for drug and drug delivery systems; Chacon *et al.* optimized the preparation of cyclosporine-loaded poly D,L (lactide-glycolide) (PLAGA) nanoparticles and microspheres [58]. Gupta *et al.* developed a statistical model by simultaneously studying the effect on various formulation factors using experimental design to predict the release properties of the drug from the delivery system [59].

The experimental design has also been applied in various composite manufacturing and design fields to identify the dominant parameters [60-64]. Baeten *et al* used the experimental design method to establish a useful processing technique and to control those parameters which lead to the production of good quality composites parts [60]. They also used the experimental design method to develop a statistical model which

provided response surfaces of the effects of the processing parameters on the mechanical performance of the final composite part.

In addition to the manufacturing parts, the experimental design method was used to characterize the damage on composite materials with various damage parameters. Southerland *et al* found out the effects of test parameters on the impact response of a glass reinforced plastic using the experimental design approach [65].

2.4 Application of Image Analysis for Crack Density Calculation

Image processing has been used for two different purposes [66]: i) improving the visual appearance of an image and ii) preparing images for measurement of the features and structures. The image processing and analysis has been broadly used especially in the biomedical engineering. In the materials science, the measurements of images has been done using image processing techniques such as feature definition, edge detection, and control of brightness and color.

A main application of image analysis on composite materials has been for the observation of the fiber volume ratio. A few endeavors for measuring damage, such as crack density, in polymer composites using image analysis have been made. In most cases, the crack density has been defined to be the number of cracks per unit specimen length or unit area instead of considering crack lengths. Some attempt to measure voids and cracks using image analysis on x-ray microtomography has been done for fracture mechanics calculations. Landies *et al.* measured the internal crack growth in small mortar cylinders using a three-dimensional scanning technique [67-69]. Muller *et al.* used optical

method based on image correlation to characterize the cracks that develop in the concrete when tensile tests were carried out [70]. Chermant *et al.* quantified the damage in ceramic matrix composites using classical tools of automatic image analysis [71].

2.5 Quantification of Damage Using Water Absorption

The water absorption can be attributed largely to the water affinity for specific functional groups of the cured polyimide resin of a highly polar nature. According to the study of Apicella *et al.* on water absorption properties of polymers, there are three modes of sorption: i) bulk dissolution of water in the polymer network, ii) moisture absorption onto the surface of holes that define the excess free volume of the glassy structure, and iii) hydrogen bonding between hydrophilic groups of the polymer and water [72,73] (Figure 2.1).

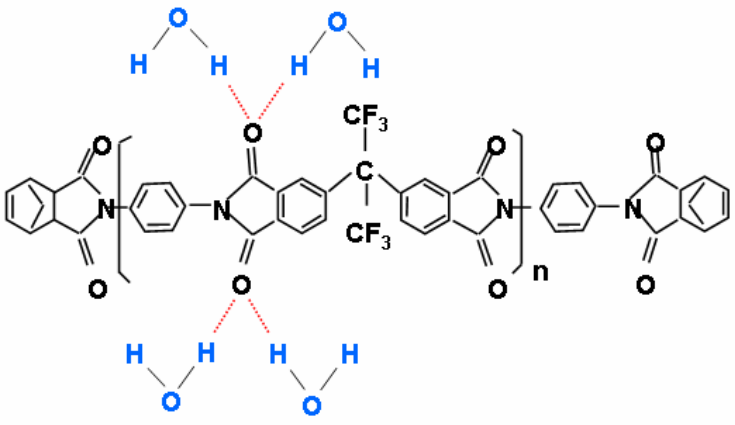

Figure 2.1. *Hydrogen bonding between hydrophilic groups of PMR-II-50 and water*

Water absorption of PMR-II-50 resin is considered in terms of the bulk dissolution in the polymer network (permeation through the matrix), percolation along the interface between the resin and fiber, or the holes such as voids and microcracks, and the hydrogen bonding between polymer hydrogen bond sites and water molecules.

In spite of a number of studies on water transport of polymers and polymer composite materials (PMCs), quantitative studies on exact diffusion model of anomalous viscoelastic polymers and PMCs have not been actively done yet. Few literatures could be found especially for a polymer's and PMC's diffusion model related to initial damage, such as cracks. Roy *et al.* tried to modify the basic diffusion model from Fick's law [74,75]. They showed that both diffusivity and saturation level can be expressed in term of a quadratic crack density function.

CHAPTER III

MATERIALS

High temperature polymer composites are required to increase thrust to weight ratios for various propulsion applications and graphite fiber polymer composite materials have been considered to be a good candidate for those applications. NASA Glenn Research Center, a leading research group in developing the high temperature polymer composites, selected PMR (*in situ* polymerization of monomer reactants) polyimide as a candidate resin of the high temperature composites. PMR-II-50, a second generation PMR, was considered to be a candidate resin for these high temperature and high stiffness space propulsion applications [51,52,76]. In this chapter, structural, mechanical, thermal, and chemical properties of resin, fiber and composites will be introduced.

Thermal and mechanical properties of the resin, fiber and composite were obtained from the data obtained by NASA Glenn research center. Basically the microstructure of the composite is a cross ply configuration of $[90/0]_s$, but individual layer can be somewhat waved as shown in Figure 3.1 because single fiber glass yarns are crossing over carbon fiber tows to keep them in fabric form.

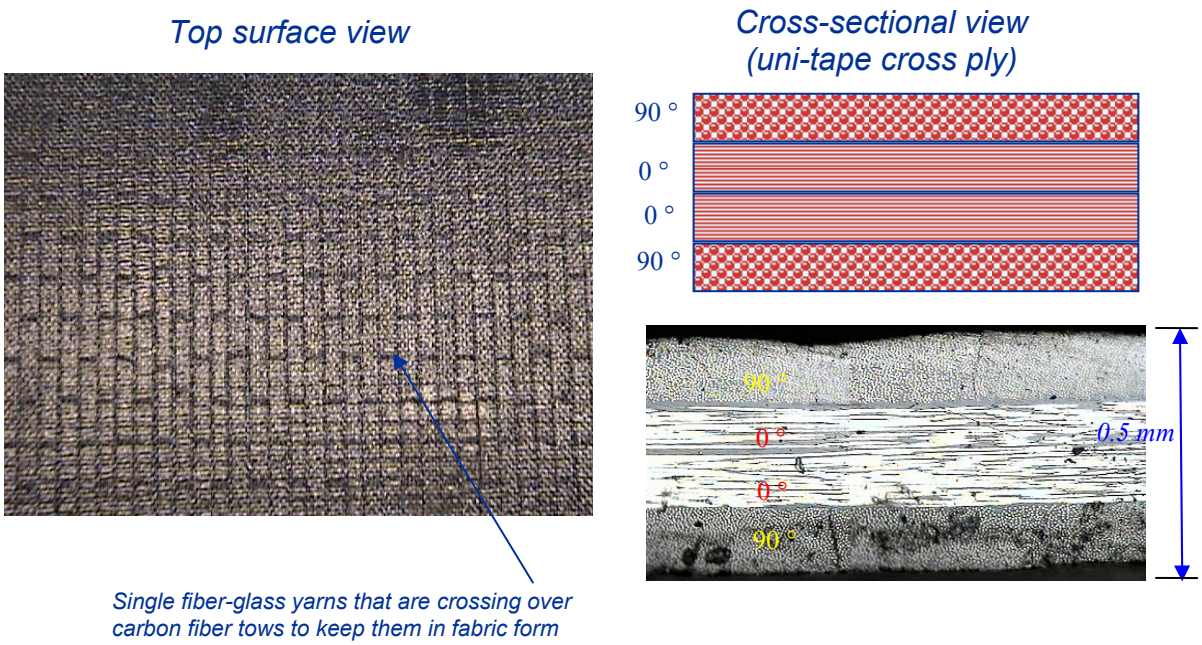

Figure 3.1. *Configuration of two layer uni-tape (uni-fabric) cross ply composite laminate*

3.1 Resin (PMR-II-50)

There are two different types of polyimide. One is derived from condensation reaction and the other is derived from addition type reaction (Figure 3.2). Addition-type of polyimide is generally derived from preformed oligomers that undergo thermal crosslinking or chain extension to form a thermoset.

One of the most prominent materials for next generation aerospace applications is PMR-II-50, a polyimide derived from addition type reaction and that includes Nadic End-Caps (Figure 3.2), that is also called a reverse Diels-Alder polyimide. The Nadic end-capped polyimides not only undergo the amidation and imidization reactions to form a low molecular weight oligomer of typical condensation polyimides, but also undergo an

irreversible Diels-Alder reaction leading to a high molecular weight crosslinked polyimide [51].

In terms of chemical structure, PMR-II-50 has an excellent thermo-oxidative stability up to 400^{o}C service temperature thanks to the carbon fluoride (CF) group in backbone. Three benzenes having PI-bonding in the backbone make the resin strong. When heated, the polymers are thermally cross linked. PMR-II-50 normally has an initial T_g of 350^{o}C. After 16 hours of postcuring at 370^{o}C, the resin has a T_g of 390^{o}C.

Figure 3.3 shows a thermal cross-linking process of PMR-II-50 oligomers and its chemical structure of cross-linked polymer.

Mechanical properties of neat PMR-II-50 are obtained from NASA Glenn Research Center and shown in Table 3.1 and Figure 3.4. Strength and modulus decrease with increasing temperature up to 371^{o}C after cure.

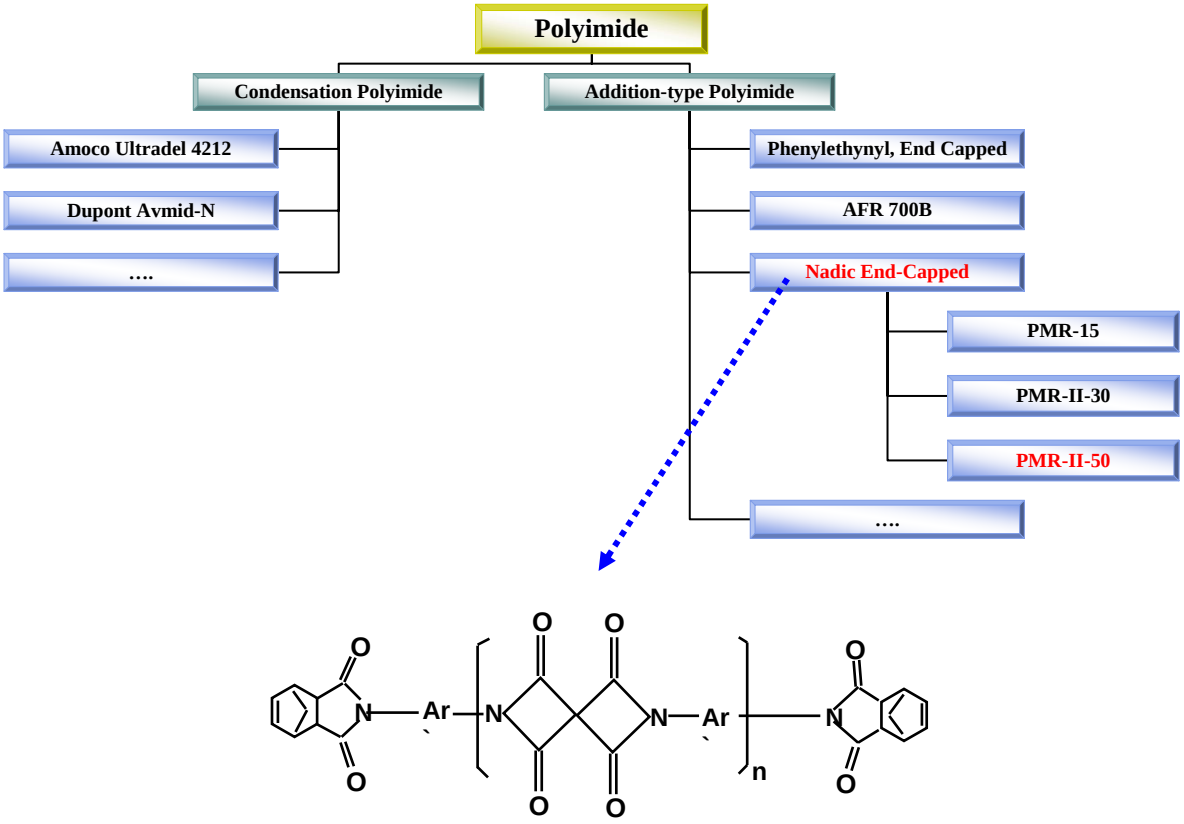

Figure 3.2. *Various types of polyimide*

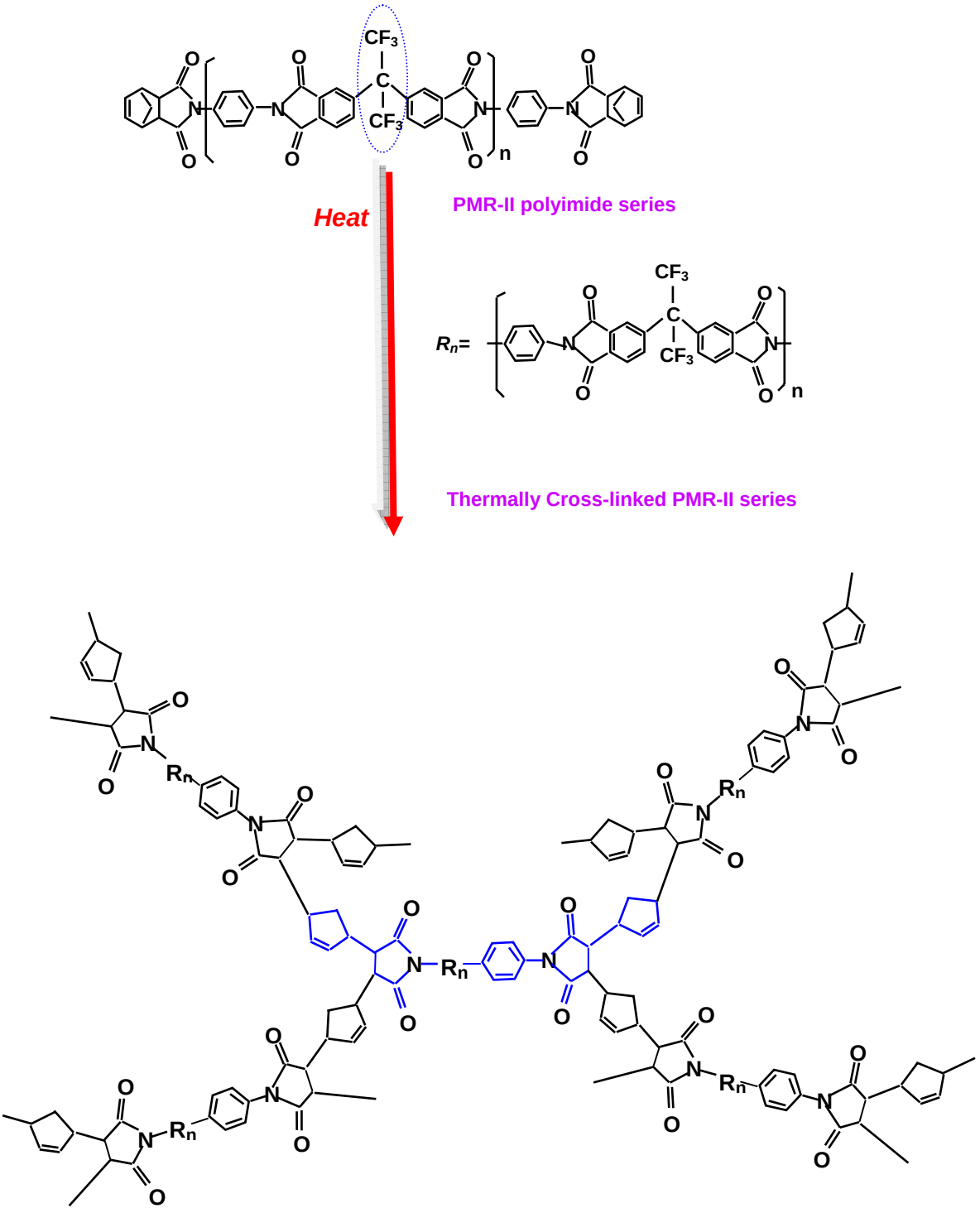

Figure 3.3. *Chemical structure of PMR-II-50 oligomer and its cross-linked polymer*

Table 3.1. *Mechanical properties of PMR-II-50 neat resin [77]*

Temperature, T (^{o}C)	Tensile Strength, X_T (MPa)	Tensile Modulus, E_T (GPa)	Poisson's ratio, ν_{12}	Shear Strength, S (MPa)	Shear Modulus, G (GPa)
RT	64.02	3.64	0.3	35.76	1.43
316	32.64	2.05	N/A	27.34	N/A
371	28.12	1.94	N/A	N/A	N/A

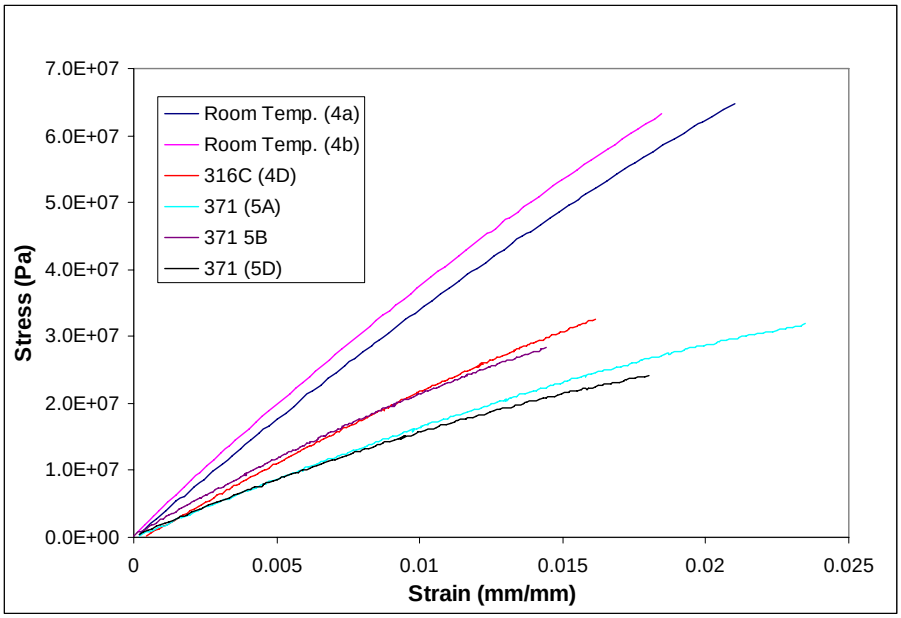

Figure 3.4. *Tensile stress-strain curve of neat PMR-II-50 provided by NASA GRC*

Mechanical and thermal properties of epoxy, bismaleimide(BMI), and polyimde are often compared to one another as a typical thermoset used for aerospace applications. Polymide (PMR-II-50) shows excellent both in modulus and strength compared to the BMI and epoxy as can be seen in Figure 3.5.

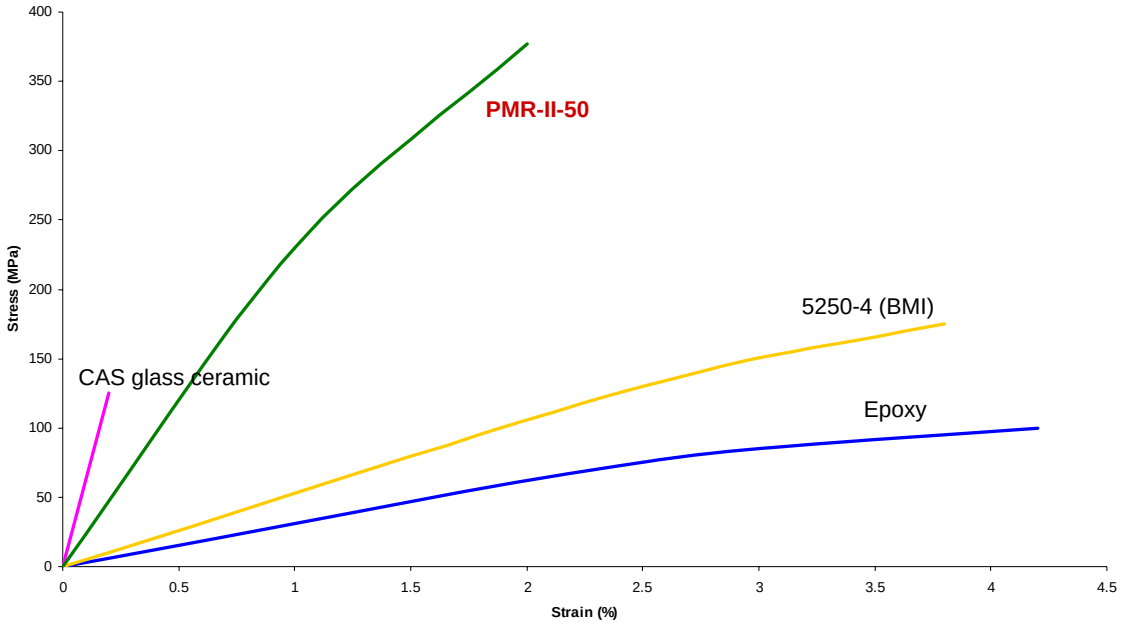

Figure 3.5. *Stress strain curves of epoxy, BMI (5250-4), and polyimide (PMR-II-50) [51, 76, 77]*

Available temperature range of the polyimide is also good up to 300^{o}C for long term use and 520^{o}C for short term use as shown in Figure 3.6. BMI also has high temperature durability but it is not still comparable with polyimide.

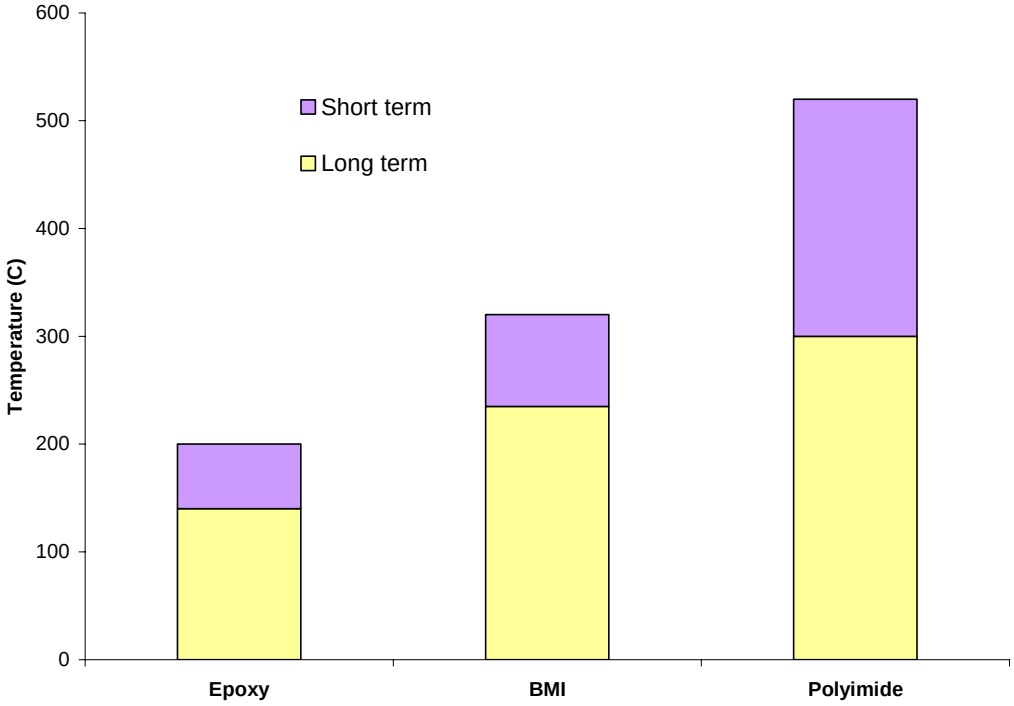

Figure 3.6. *Usable temperature ranges of Epoxy, BMI (5250-4), and Polyimide (PMR-II-50) [51,76,77]*

3.2 Fiber (M40J)

The M40J fibers have been selected for their high modulus and strength. Zhou *et al.* measured the tensile strength of fiber bundles under different strain rates. They found the M40J fibers are strain-rate insensitive materials, and the average modulus, strength, and strain at failure of the fiber were reported to be 359.2GPa, 3344MPa, and 1.28%, respectively with 4130 filaments when assuming 5.5μm of fiber diameter [78].

Mechanical and thermal properties of the M40J fabric having about 6000 filaments of 5.5μm fiber diameter were obtained from the available literature [79,80]; The fabric has 4400MPa tensile strength, 377GPa tensile modulus, 0.7 Poison's ratio, 1.93g/cm^3 density, 1.2% strain at failure, and -0.83E-6/^{o}C longitudinal CTE.

Figure 3.7 shows stress-strain curves of various fibers which are used for composite reinforcement. M40J and IM7 have high modulus and strength compared to the other fibers.

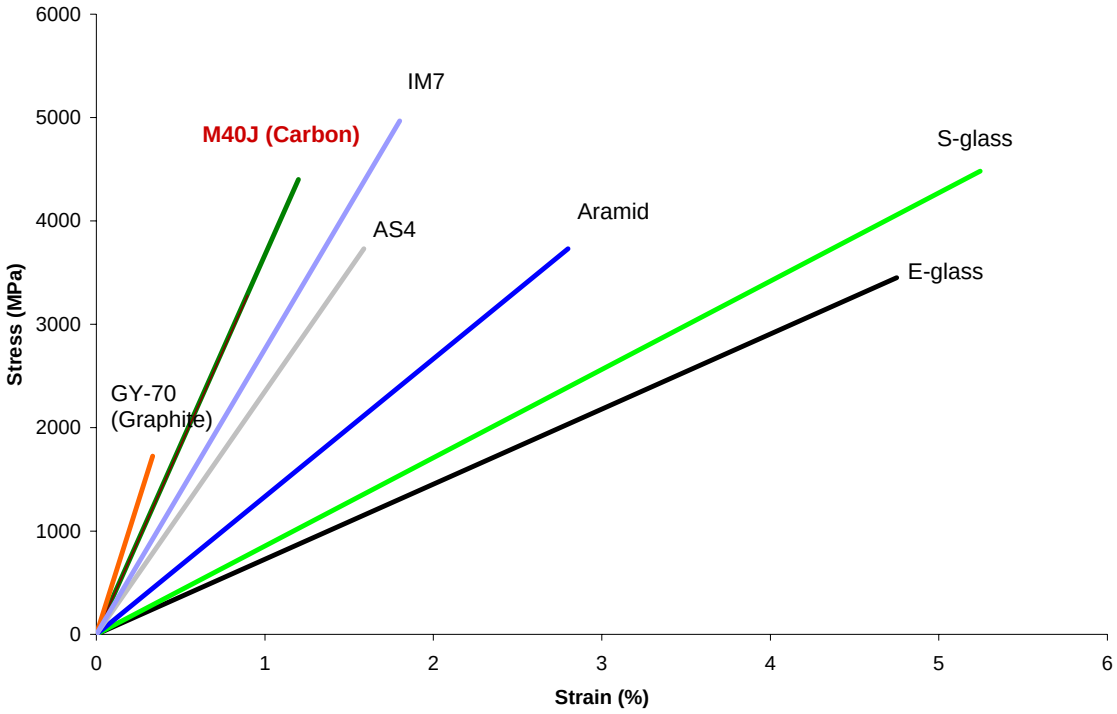

Figure 3.7. *Stress-strain curves of various fibers used for reinforcements [78-80]*

3.3 Composite (M40J/ PMR-II-50)

A unidirectional or uni-tape architecture with higher strengths and moduli has approximately 15 to 25% higher tensile strength that woven fabric [7]. However, the uni-tape architectures suffer from lower toughness, hygrothermal performance and production cost [7]. In this part, the uni-tape two ply configuration M40J/PMR-II-50

composites was manufactured using, so called, “tow plate-winding” with a modified lathe for fabrication of all unidirectional panels.

The composite has a 389^{o}C glass transition temperature (T_g), 545^{o}C decomposition temperature (T_d), 58.13% total fiber volume ratio, 35.98% matrix weight ratio, 1.80% void fraction, 1.65g/cm^3 density, 23.4msi of tensile modulus, 20.3msi of compression modulus, 0.83msi of shear modulus, and $1.2e^{\frac{-371}{T_k}}\ [W/mK]$ of thermal conductivity over a temperature range of 40-160^{o}C [76]. Fiber areal weight (FAW) of the composite is 215g/m^2. Physical and thermal properties of M40J/PMR-II-50 are shown in Table 3.2. Temperature dependence of modulus and strength are shown in Table 3.3.

The panel was vacuum-bagged in a press and cured according to the process done by NASA Glenn Research Center (Manufacturing details are shown in the reference) [76]. After that, the panel was postcured in air for 16 hours at 370^{o}C then cooled to room temperature in 2 hours as can be seen in Figure 3.8.

Table 3.2. *Physical-thermal properties of M40J/PMR-II-50 uni-tape cross-ply composites [76]*

Density (g/cm3)	***Void Content (%)***	***Fiber Volume Fraction, (%)***	***Glass Transition Temperature, T_g (^oC)***	
			G' Onset	$\tan\delta$
1.621 ± 0.010	0.5 ± 0.2	57 ± 3	378	410

Table 3.3. *Mechanical properties of M40J/PMR-II-50 uni-tape cross-ply composites having 0.02 inch (0.508mm) thickness [77]*

	Tension			***Compression***		
	Dry at RT	***Dry at 315^{o}C***	***Wet at 315^{o}C***	***Dry at RT***	***Dry at 315^{o}C***	***Wet at 315^{o}C***
Modulus (MSI)	13.1 ± 0.1	14.3 ± 1.1	14.9 ± 1.2	11.7 ± 0.4	13.5 ± 0.7	14.0 ± 0.2
Strength (KSI)	92.7 ± 4.3	93.7 ± 1.2	101.3 ± 5.4	56.3 ± 7.7	44.6 ± 9.2	43.1 ± 9.1
Strain to Failure ($\mu\varepsilon$)	6969 ± 421	6209 ± 558	6593 ± 73	4928 ± 61	3353 ± 739	3263 ± 91

* For the compression test, 0.1 inch thick panel was used

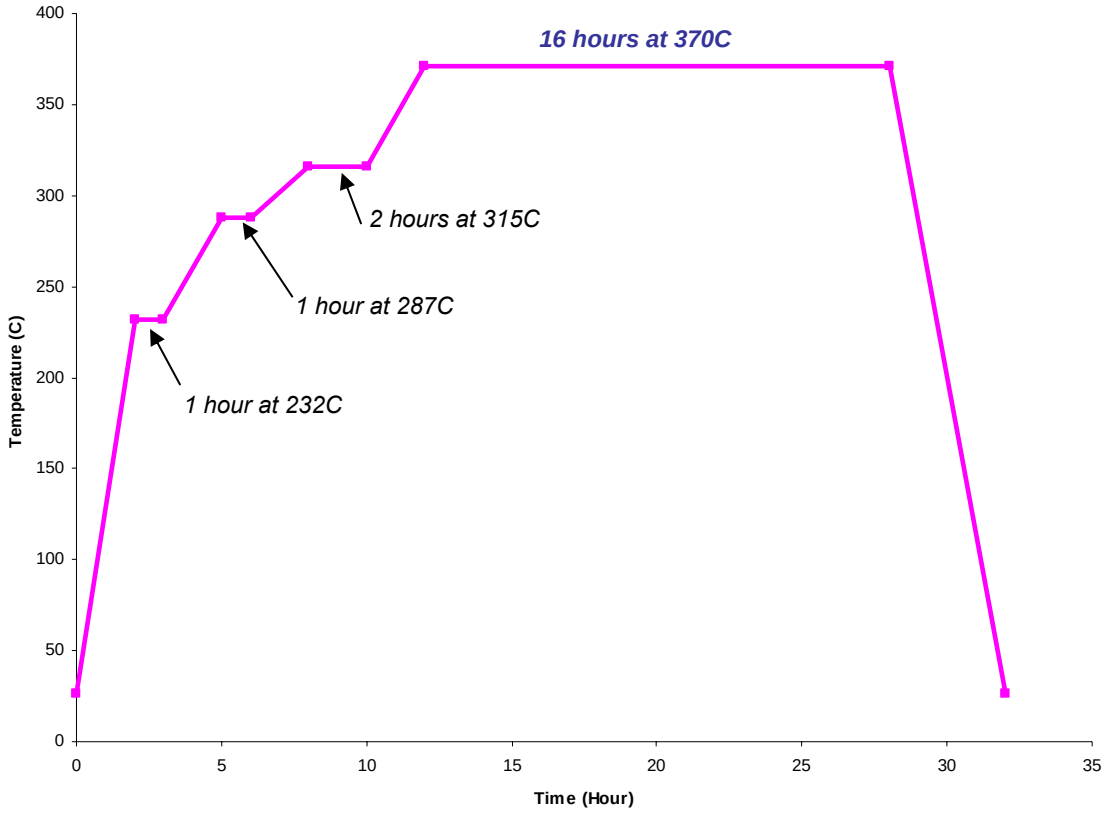

Figure 3.8. *Postcuring cycle for the M40J/PMR-II-50 [76]*

Table 3.4 shows the thermal and mechanical properties of M40J, PMR-II-50, and M40J/PMR-II-50 composite measured at room temperature. These data will be used for the analytical study in Chapter VI to evaluate our experimental results.

Figures 3.9 and 3.10 are stress-strain curves of M40J/PMR-II-50 and IM7/5250-4, respectively. Those composites have been actively studied for cryogenic thermo-cycling application for aerospace application. Data comparison of results after current experiments using M40J/PMR-II-50 with IM7/5250-4 in literature will be beneficial to validate the reasonability of the results.

Figure 3.11 is the thermal expansion of M40J/PMR-II-50 as a function of temperature both in the longitudinal and transverse direction [76]. As shown in the Figure 3.11, the thermal expansion of the transverse direction is much higher than that of longitudinal one because the properties of transverse direction are more rely on the matrix (PMR-II-50) which has a higher thermal expansion.

Table 3.4. *Thermo-mechanical properties of M40J, PMR-II-50, and M40J/PMR-II-50 at 20°C [77-79,80]*

	Symbol (Units)	**M40J** (Radius=5.5μm)	**PMR-II-50**	**M40J/PMR-II-50** ($V_{f,tow}$ = 58.13%)
Longitudinal tensile modulus	E_{11T} (GPa)	316	3.64	181.7
Transverse tensile modulus	E_{22T} (GPa)	13.4	3.64	8.9
Transverse tensile modulus	E_{33T} (GPa)	13.4	3.64	7.19
Longitudinal compression modulus	E_{11C}(GPa)	N/A	N/A	80.6
Tensile Strength	X_{11T}(MPa)	4.41	N/A	639
Compression Strength	X_{11C}(MPa)	N/A	N/A	388
Strain at Failure	(%)	1.2	1.9	0.69
Shear modulus	G_{12} (GPa)	20.8	1.43	4.73
Shear modulus	G_{13} (GPa)	20.8	1.43	4.73
Shear modulus	G_{23} (GPa)	3.9	1.43	2.58
Poisson's ratio	ν_{12}	0.22	0.3	0.26
Poisson's ratio	ν_{13}	0.22	0.3	0.26
Poisson's ratio	ν_{23}	N/A	0.3	N/A
Thermal expansion coefficient	α_{11} (/°C)	-2.05E-6	39.19E-6	-1.6E-6
Thermal expansion coefficient	α_{22} (/°C)	-6.9E-6	39.19E-6	20.1E-6
Thermal expansion coefficient	α_{33} (/°C)	-6.9E-6	39.19E-6	26.7E-6

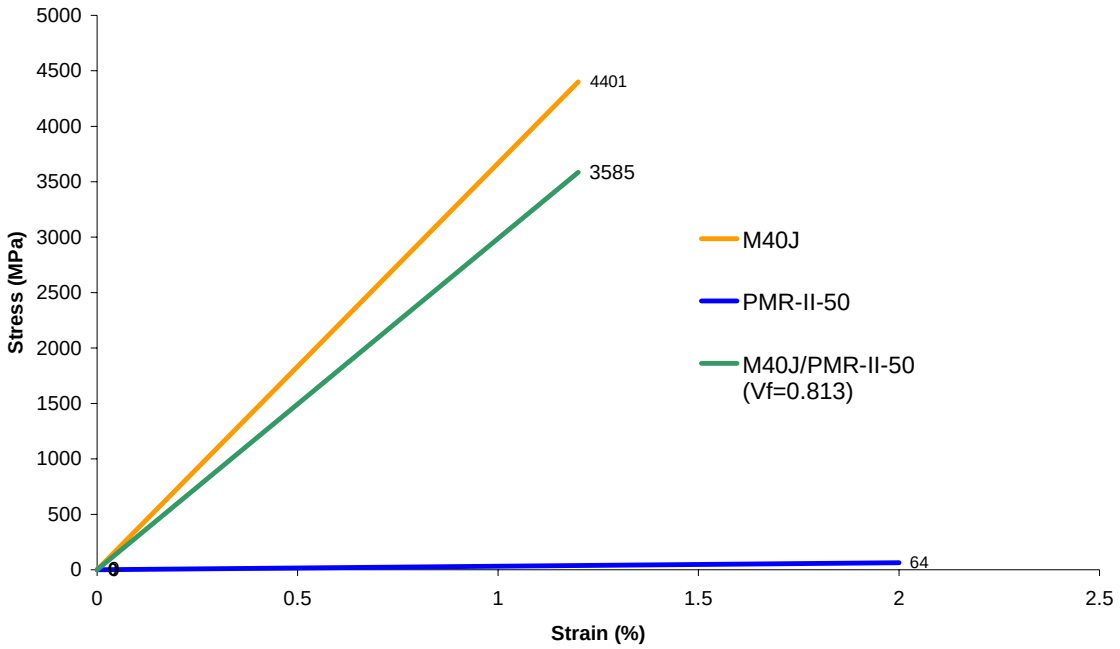

Figure 3.9. *Stress-strain curves of M40J, PMR-II-50, and M40J/PMR-II-50 composite (V_f=0.813) [51,76,77]*

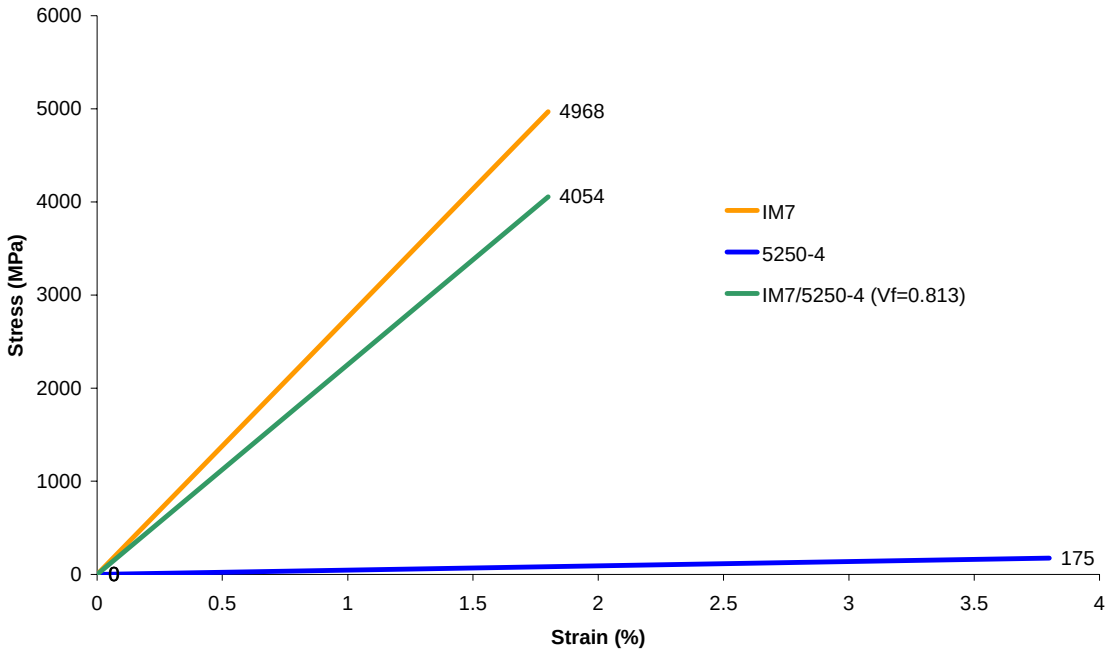

Figure 3.10. *Stress-strain curves of IM7, 5250-4, and IM7/5250-4 composite (V_f=0.813) [51,78-80]*

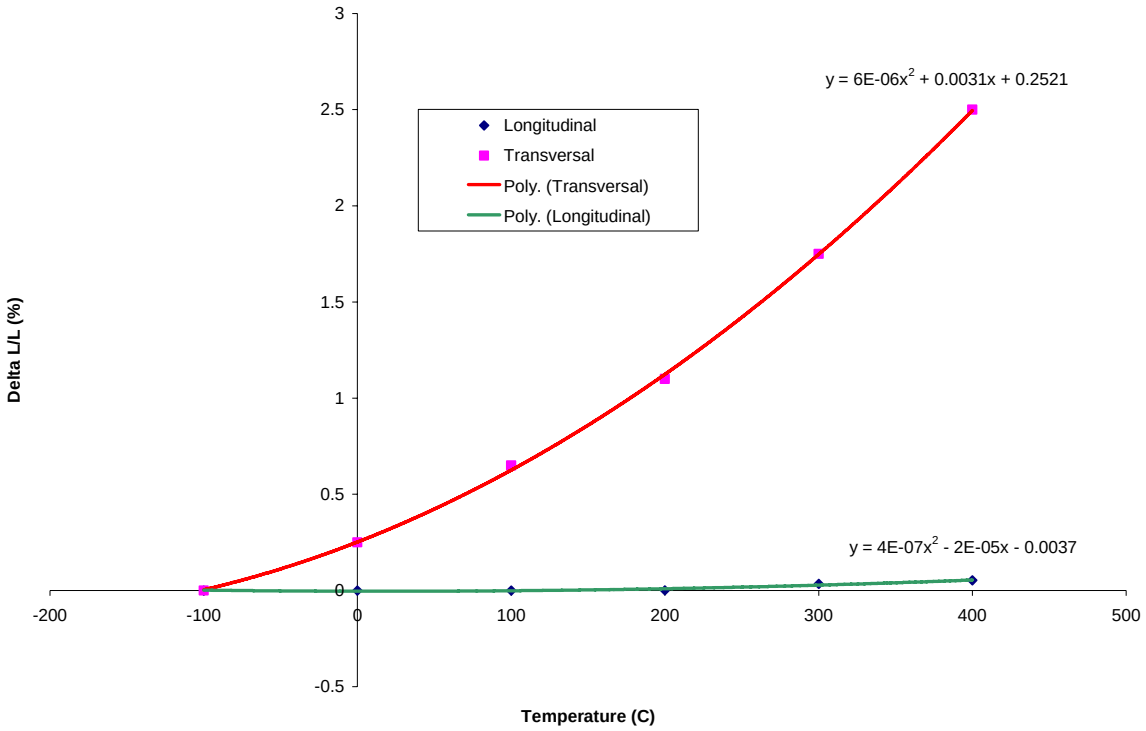

Figure 3.11. *Thermal expansions (a) in-plane and (b) out-of plane for the M40J/PMR-II-50 as a function of temperature [76]*

Samples were cut with a diamond saw to 110mm in length, 10mm in width, and 0.5mm in thickness for experiments. Experimental details of the prepared samples will be explained in next chapter.

CHAPTER IV

DEVELOPMENT OF NOVEL CONDUCTION HEATING BASED STRESS-THERMAL CYCLING APPARATUS AND ITS APPLICATION*

According to the ASTM E512, methodologies for combined simulated environment testing of thermal control materials are divided into two categories in terms of specimen thermal control; 1) One is that the specimen can be insulated from its surroundings and convection type heating is applied. 2) The other is that specimens are thermally intimately contacted with a heat source and conduction based heating is applied to the specimens. Most of the thermal cycling has been performed by the first method. In this study, the second method is applied. Based not only on the good contact condition between the specimens and the heating source but also the cooling by circulating nitrogen, a new experimental methodology of stress-thermal cycling was developed.

As can be seen from Figures 4.1 to 4.3, specimens are attached along the radial direction of the block surface, which is under bending loading condition. In case of no strain condition, a specimen is placed on the flat surface as shown in Block #3 of Figure 4.3. Inside the half cylinder shapes of aluminum blocks having different radii, heaters are embedded and conduction type of heat is transferred to the specimens. Each block is

---

*Part of this chapter is reprinted with permission from "Characterization of Microcrack Development in BMI-Carbon Fiber Composite under Stress and Thermal Cycling" by Ju, J. and Morgan, R. (2004), *Journal of Composite Materials, 38* (22): 2007-2024 by SAGE Publications.

connected to temperature controllers and maximum temperature is controlled by the temperature controllers and different heating rates can be applied by the transformer by changing the voltage. When cooling the specimens, liquid nitrogen flows inside the chamber. In order not to let specimen contact the liquid nitrogen directly, for preventing local thermal shock on the surface of the specimen, an aluminum cover is set above the specimens. While liquid nitrogen touches the cover and falls down to the bottom of the chamber, two fans propel for helping the liquid nitrogen evaporate and make a uniform cooling effect on the specimens. Therefore, with this apparatus, the specimens under bending load can be exposed to large temperature changes during thermal cycling.

We will systematically investigate how stress-thermal cycling affects microcrack development in polyimide carbon fabric (M40J/PMR-II-50). The temperature cycle range from cryogenic temperatures (-196^{o}C) up to 250^{o}C with different number of cycles, and the maximum pre-strain levels from 0 to 0.65% (corresponding to transverse maximum stress levels of the 90^{o} composite ply from 0 to 57.85 MPa) were applied in this study. Independent and interaction effects from the various factors on microcrack development will be obtained from the stress-thermal cycling experiment.

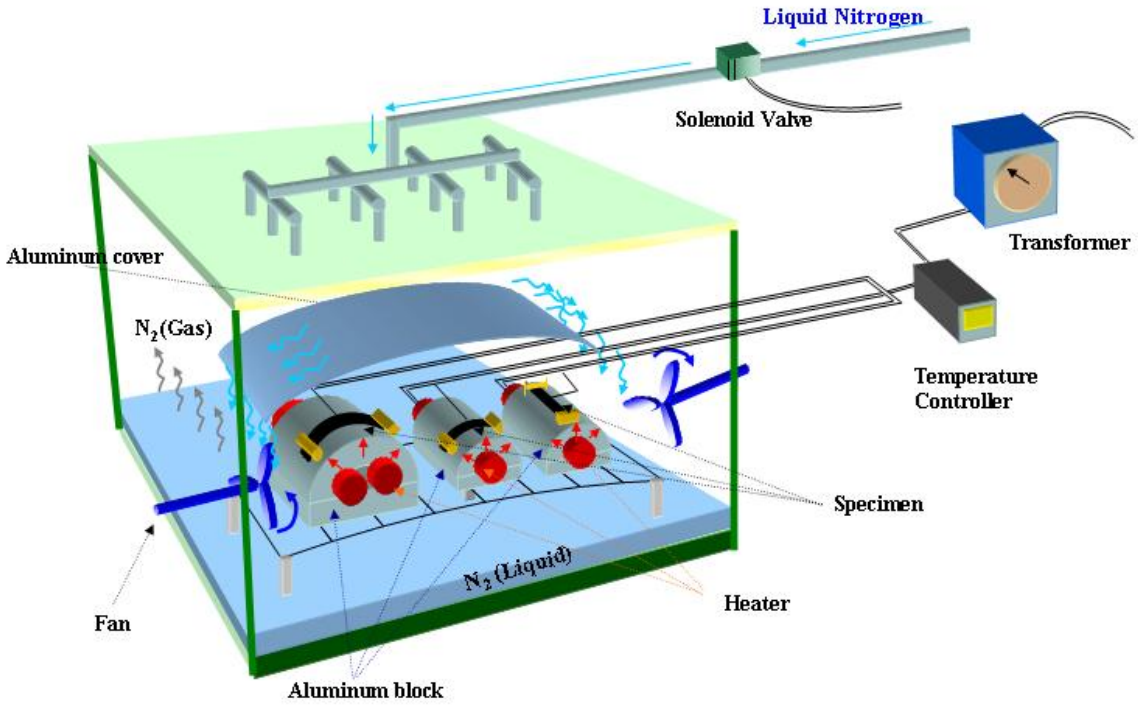

Figure 4.1. *Schematic of the conduction heating based stress-thermal cycling facility*

Figure 4.2. *Picture of the developed stress-thermal cycling apparatus*

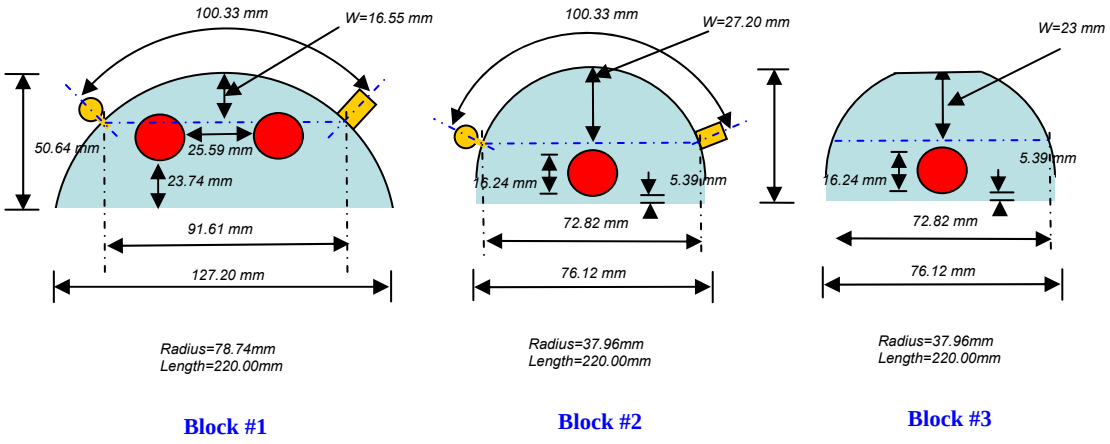

Figure 4.3. *Dimensions of aluminum blocks*

4.1 Mechanical Loading Conditions: Analysis of Laminated Beam Using the Classical Laminate Plate Theory (CLPT)

Bending was used as the applied loading in this study. However, when simulating the loading condition of cryogenic fuel tank, the bending does not necessarily represent loading conditions of the tank. Instead, generally, bi-axial loading is considered to express the loading condition of the fuel tank under fuel pressure. The reason why the bending is used as an applied loading in this study is that only bending loading was the most acceptable loading condition when considering the developed apparatus which combines

the conduction heating type of thermal cycling with loading. Even though the bending does not represent the loading condition of the cryogenic tank, in-plane strain (or stress) can be derived from the bending and the derived in-plane strain (or stress) conditions can be applied to assess the strain (or stress) conditions of initial cracks with combined thermal cycling. A simply supported beam with large deflection condition was used with pin-clamping one side of the specimen and roller-clamping the other side of the specimen. Euler-Bernoulli's exact differential equation for the elastic curve was applied to get the in-plane stress conditions [81].

At this time, in-plane stress at the laminate level without considering fabric architecture is used first. When the specimens are bent, the deflection curve of the specimen can be derived from the geometry of the aluminum block by applying a large deflection condition. When the specimen is deflected, the projected length of the sample (L_1) becomes 10 to 15% less than the initial sample length (L_0) as seen in Figure 4.4.

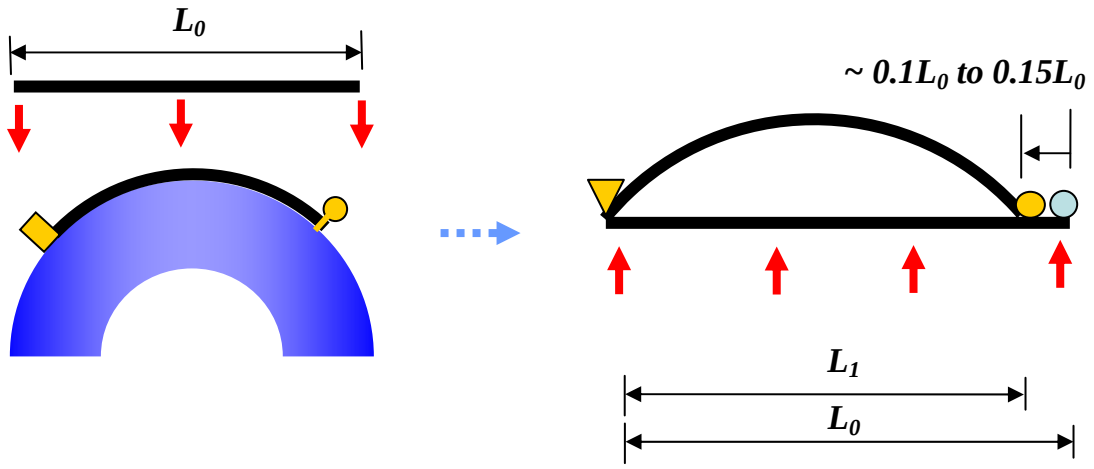

Figure 4.4. *Large deflection bending conditions*

The loading sequence is illustrated in Figure 4.5. One side of a specimen is pin clamped on the aluminum block and a force is carefully applied to the other side to bend. The other side edge is roller clamped for the longitudinal constraint free condition.

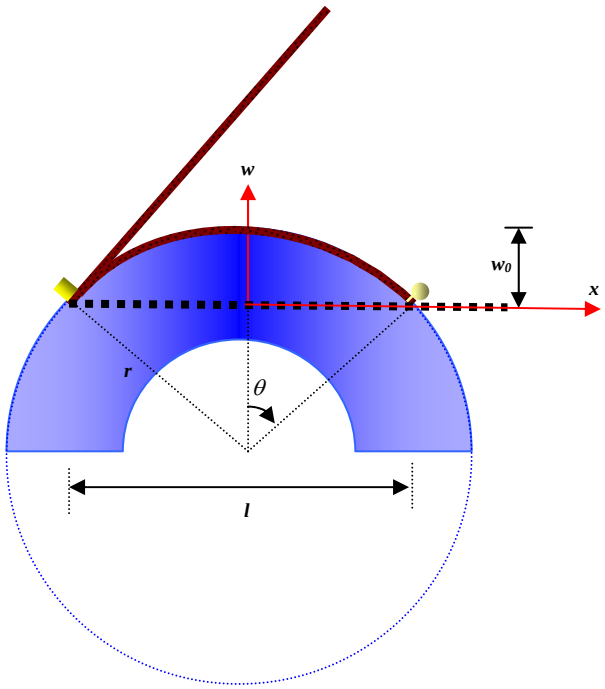

Figure 4.5. *Large deflection bending associated with block geometry*

From Figure 4.5, the deflection geometry associated with x and $w(x)$ coordinates are derived.

$$x = r\sin\theta$$
$$w = r\cos\theta - (r - w_0) \tag{4-1}$$

$$\frac{dw}{dx} = \frac{d\theta}{dx}\frac{dw}{d\theta} \tag{4-2}$$

and

$$\begin{aligned} \frac{dx}{d\theta} &= r\cos\theta \\ \frac{dw}{d\theta} &= -r\sin\theta \end{aligned} \tag{4-3}$$

Substituting (4-2) into (4-3) results in

$$\frac{dw}{dx} = \frac{1}{r\cos\theta} \times -r\sin\theta = -\tan\theta \tag{4-4}$$

and

$$\begin{aligned} \frac{d^2w}{dx^2} &= \frac{d}{dx}\left(\frac{dw}{dx}\right) \\ &= \frac{d}{dx}(-\tan\theta) \\ &= \frac{d\theta}{dx}\cdot\frac{d}{d\theta}(-\tan\theta) \\ &= \frac{1}{r\cos\theta}\cdot\frac{-1}{\cos^2\theta} \\ &= -\frac{1}{r\cos^3\theta} \end{aligned} \tag{4-5}$$

From the geometry of the curved block shapes, the deflection curve, *w(x)* can be derived. By inserting the *w(x)* into the equation (4-6), a relation between moment and deflection curve associated with Euler-Bernoulli's exact differential equation for elastic

curve, the bending moment, M_{xx} is derived from the obtained deflection curves. For driving the laminated beam theory, we assume that $M_{yy} = M_{xy} = 0$.

$$\left(\frac{\frac{d^2w}{dx^2}}{\left[1+\left(\frac{dw}{dx}\right)^2\right]^{3/2}}\right) = -\frac{M_{xx}}{EI} \tag{4-6}$$

where

w : deflection cure

M_{xx}: Bending Moments

E: Modulus

I: Moment of inertia (=bh^3/12, b: width, h: thickness of the specimen)

Substituting equation (4-4) and (4-5) into (4-6) results in constant bending moment resultants along the length direction; 0.0759 [$N \cdot m$] for small curvature block geometry and 0.1433 [$N \cdot m$] for large curvature one (Figure 4.6). The moment induced bending strains were respectively, -0.35 to 0.35% for the small curvature block and -0.65 to 0.65% for large curvature block (Figure 4.7).

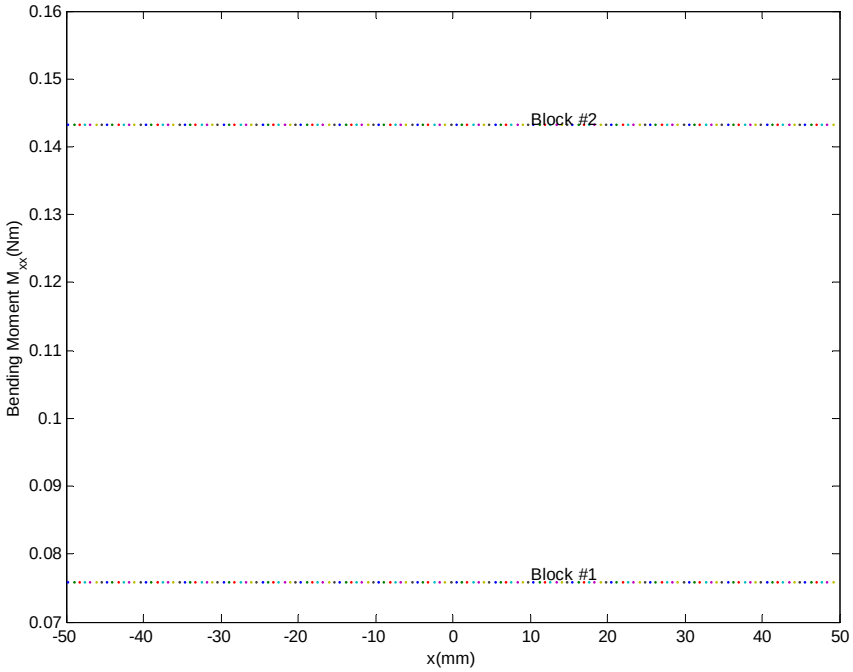

Figure 4.6.*Bending moment of the sample under the cylindrical surface*

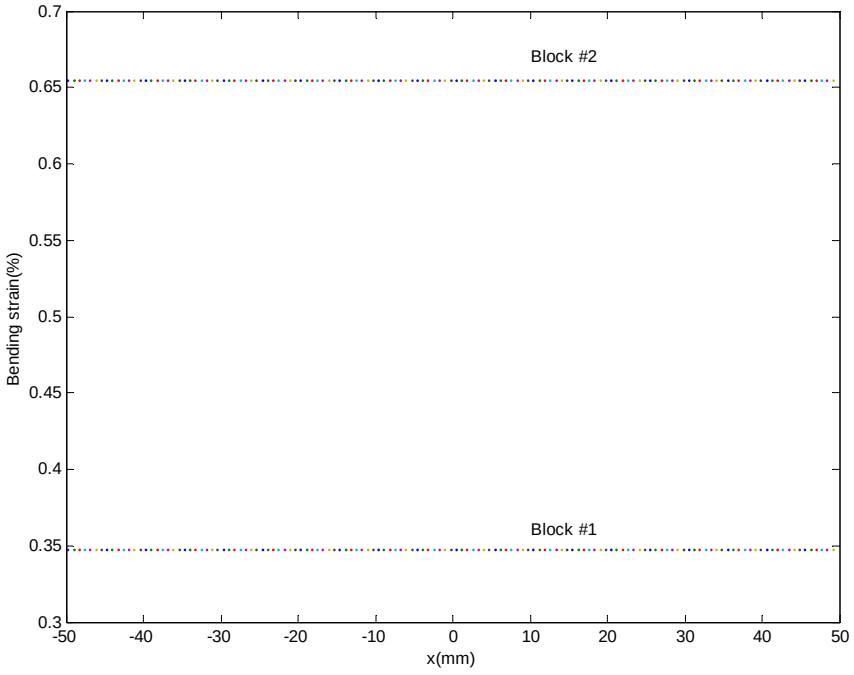

Figure 4.7. *Bending strain through length direction*

It should be noted that (Figure 4.8)

$$\begin{aligned}\frac{d\theta}{dS} &= \frac{d\theta}{dx}\cdot\cos\theta \\ &= \frac{1}{r\cos\theta}\cdot\cos\theta \\ &= \frac{1}{r} \\ &= curvature \\ &= -\frac{M_{xx}}{EI}\end{aligned} \tag{4-7}$$

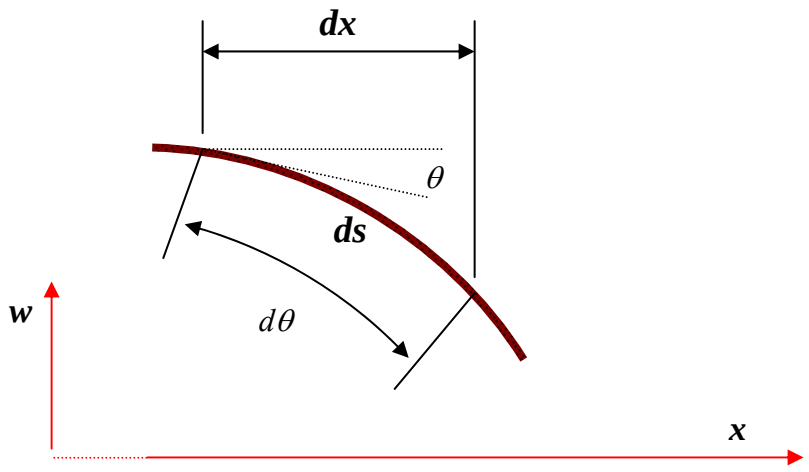

Figure 4.8. *Angle and displacement relation under deflection*

From the moment obtained from the equation (4-6), in-plane stresses of laminate level are calculated by equation (4-8),

$$\sigma_{xx}(x,z) = \frac{Mz}{b}(Q_{11}D_{11}^{*} + Q_{12}D_{12}^{*}) \tag{4-8}$$

where

$$D_{ij}^{*} = D_{ij} - B_{ik}A_{kl}^{-1}B_{lj}$$
$$(A_{ij}, B_{ij}, D_{ij}) = \int_{-h/2}^{h/2}(1, z, z^{2})Q_{ij}dz$$

$$Q_{11} = \frac{E_1}{1 - v_{12}v_{21}}$$
$$Q_{22} = \frac{E_2}{1 - v_{12}v_{21}}$$
$$Q_{12} = \frac{v_{21}E_1}{1 - v_{12}v_{21}} = \frac{v_{12}E_2}{1 - v_{12}v_{21}}$$
$$Q_{66} = G_{12}$$

Q_{ij}: Plane stress-reduced stiffness

A_{ij}: Extensional stiffness

B_{ij}: Bending-Extensional coupling stiffness

D_{ij}: Bending stiffness

E_i: Modulus

v_{ij}: Poison's ratio

Expanding the (4-8) to the stress components of layer levels results in

$$\begin{Bmatrix}\sigma_{xx}\\ \sigma_{yy}\\ \sigma_{xy}\end{Bmatrix}^{(k)} = z\begin{bmatrix}\overline{Q}_{11} & \overline{Q}_{12} & 0\\ \overline{Q}_{12} & \overline{Q}_{22} & 0\\ 0 & 0 & \overline{Q}_{66}\end{bmatrix}^{(k)}\begin{Bmatrix}-\dfrac{\partial^2 w_0}{\partial x^2}\\ -\dfrac{\partial^2 w_0}{\partial x^2}\\ -2\dfrac{\partial^2 w_0}{\partial x \partial y}\end{Bmatrix} \qquad (4\text{-}9)$$

$$= \frac{z}{b}\begin{bmatrix}\overline{Q}_{11} & \overline{Q}_{12} & 0\\ \overline{Q}_{12} & \overline{Q}_{22} & 0\\ 0 & 0 & \overline{Q}_{66}\end{bmatrix}^{(k)}\begin{bmatrix}D_{11}^{*} & D_{12}^{*} & D_{16}^{*}\\ D_{12}^{*} & D_{22}^{*} & D_{26}^{*}\\ D_{16}^{*} & D_{26}^{*} & D_{66}^{*}\end{bmatrix}\begin{Bmatrix}M_{xx}\\ 0\\ 0\end{Bmatrix}$$

4.2 Strain Condition under Large Deflection and Thermal Loading

According to the classical laminate and plate theory (CLPT), *von karman strains* based on the Berinoulli beam theory, transverse strains ($\varepsilon_{xz}, \varepsilon_{yz}, \varepsilon_{zz}$) are identically zero [82]. The remaining terms are

$$\begin{Bmatrix}\varepsilon_{xx}\\ \varepsilon_{yy}\\ \gamma_{xy}\end{Bmatrix} = \begin{Bmatrix}\varepsilon_{xx}^{(0)}\\ \varepsilon_{yy}^{(0)}\\ \gamma_{xy}^{(0)}\end{Bmatrix} + z\begin{Bmatrix}\varepsilon_{xx}^{(1)}\\ \varepsilon_{yy}^{(1)}\\ \gamma_{xy}^{(1)}\end{Bmatrix} \qquad (4\text{-}10)$$

where

$$\left\{\varepsilon^0\right\} = \begin{Bmatrix}\varepsilon_{xx}^{(0)}\\ \varepsilon_{yy}^{(0)}\\ \gamma_{xy}^{(0)}\end{Bmatrix} = \begin{Bmatrix}\dfrac{\partial u_0}{\partial x} + \dfrac{1}{2}\left(\dfrac{\partial w_0}{\partial x}\right)^2\\ \dfrac{\partial v_0}{\partial y} + \dfrac{1}{2}\left(\dfrac{\partial w_0}{\partial y}\right)^2\\ \dfrac{\partial u_0}{\partial y} + \dfrac{\partial v_0}{\partial x} + \dfrac{\partial w_0}{\partial x}\dfrac{\partial w_0}{\partial y}\end{Bmatrix}$$

$$\{\varepsilon^1\} = \begin{Bmatrix} \varepsilon_{xx}^{(1)} \\ \varepsilon_{yy}^{(1)} \\ \gamma_{xy}^{(1)} \end{Bmatrix} = \begin{Bmatrix} -\dfrac{\partial^2 w_0}{\partial x^2} \\ -\dfrac{\partial^2 w_0}{\partial y^2} \\ -2\dfrac{\partial^2 w_0}{\partial x \partial y} \end{Bmatrix}$$

where $(\varepsilon_{xx}^{(0)}, \varepsilon_{yy}^{(0)}, \gamma_{xx}^{(0)})$ are the *membrane strains*, and $(\varepsilon_{xx}^{(1)}, \varepsilon_{yy}^{(1)}, \gamma_{xx}^{(1)})$ are the *bending (flexural) strains*, also known as the *curvature*. It should be noted that the bending strain terms are dependent on the laminate thickness. However, the membrane strain terms are independent on the thickness.

As shown in (4-6), bending moment, M_{xx} is a nonlinear function of $\frac{dw}{dx}$. However, a numerical calculation of M_{xx} shows the bending moments are constant along the x, which means the present loading condition can be considered as a pure bending. Considering a boundary condition, because an axial force was not applied to the specimen, $\frac{\partial u_0}{\partial x}, \frac{\partial u_0}{\partial y}, \frac{\partial v_0}{\partial x}$, and $\frac{\partial v_0}{\partial y}$ are negligible [83]. But it should be noted that there still exists membrane strains featured by $(\frac{\partial w_0}{\partial x})^2$. Nevertheless the term is small, it cannot be negligible compared to ε. That is why Timoshenko and Woinowsky-Krieger mentioned that a strain of the middle plane of the plate cannot be neglected in cases in which the deflections are no longer small as compared with the thickness of the plate, the problem must be extended to include the strain of the middle plane of the plate [82,83].

Total strain by bending is expressed as

$$\{\varepsilon\} = \begin{Bmatrix} \varepsilon_{xx}^{(0)} \\ \varepsilon_{yy}^{(0)} \\ \gamma_{xy}^{(0)} \end{Bmatrix} + z \begin{Bmatrix} \varepsilon_{xx}^{(1)} \\ \varepsilon_{yy}^{(1)} \\ \gamma_{xy}^{(1)} \end{Bmatrix} = \begin{Bmatrix} \frac{1}{2}\left(\frac{\partial w_0}{\partial x}\right)^2 \\ 0 \\ 0 \end{Bmatrix} + z \begin{Bmatrix} -\frac{\partial^2 w_0}{\partial x^2} \\ 0 \\ 0 \end{Bmatrix}$$

$$= \begin{Bmatrix} \frac{1}{2}(-\cot\theta)^2 \\ 0 \\ 0 \end{Bmatrix} + z \begin{Bmatrix} \frac{1}{r\sin^3\theta} \\ 0 \\ 0 \end{Bmatrix} \qquad (4\text{-}11)$$

Total strain combined mechanical with thermal part is expressed as

$$\begin{Bmatrix} \varepsilon_{xx} \\ \varepsilon_{yy} \\ \gamma_{xy} \end{Bmatrix} = \begin{Bmatrix} \varepsilon_{xx}^{(0)} - \alpha_{xx}T^0 \\ \varepsilon_{yy}^{(0)} - \alpha_{yy}T^0 \\ \gamma_{xy}^{(0)} - 2\alpha_{xy}T^0 \end{Bmatrix} + z \begin{Bmatrix} \varepsilon_{xx}^{(1)} - \alpha_{xx}T^1 \\ \varepsilon_{yy}^{(1)} - \alpha_{yy}T^1 \\ \gamma_{xy}^{(1)} - 2\alpha_{xy}T^1 \end{Bmatrix} \qquad (4\text{-}12)$$

where

$$\Delta T = T_0 + zT_1$$

T_0 is the temperature on mid-plane.

T_1 is the temperature gradient though specimen thickness.

4.3 Thermal Loading Conditions: Analysis of Laminated Beam Using the CLPT

Assuming the temperature varies linearly through the thickness direction of the plate, the temperature difference can be written

$$\Delta T = T_0 + zT_1 \qquad (4\text{-}13)$$

where T_0 is the difference between the average temperature of the plate and the reference temperature and T_1 is the change in temperature per unit thickness of the plate. Due to the symmetry of the lamina scheme, thicknesses, and lamina properties about the laminate, the coupling between bending and extension is eliminated and the governing equation is simplified [82]. The symmetry reduced thermal force resultants are

$$\begin{Bmatrix} N_{xx}^T \\ N_{yy}^T \\ N_{xy}^T \end{Bmatrix}^{(k)} = \int_k^{k+1} \begin{bmatrix} \overline{Q}_{11} & \overline{Q}_{12} & 0 \\ \overline{Q}_{12} & \overline{Q}_{22} & 0 \\ 0 & 0 & \overline{Q}_{66} \end{bmatrix}^{(k)} \begin{Bmatrix} \alpha_{xx} \\ \alpha_{yy} \\ 2\alpha_{xy} \end{Bmatrix}^{(k)} \Delta T \, dz \tag{4-14}$$

and

$$\begin{Bmatrix} M_{xx}^T \\ M_{yy}^T \\ M_{xy}^T \end{Bmatrix}^{(k)} = \int_k^{k+1} \begin{bmatrix} \overline{Q}_{11} & \overline{Q}_{12} & 0 \\ \overline{Q}_{12} & \overline{Q}_{22} & 0 \\ 0 & 0 & \overline{Q}_{66} \end{bmatrix}^{(k)} \begin{Bmatrix} \alpha_{xx} \\ \alpha_{yy} \\ 2\alpha_{xy} \end{Bmatrix}^{(k)} \Delta T \, z \, dz \tag{4-15}$$

Once the thermal force and moment resultants are obtained, they can be converted to a stress form for stress analysis. The force and moment resultants are just the thickness averaged lamina forces and moments per unit width of the plate. Therefore, the thermal axial stress in the kth lamina, $\left\{\sigma^{N^T}\right\}^{(k)}$ is

$$\left\{\sigma^{N^T}\right\}^{(k)} = \begin{Bmatrix} \sigma_{xx}^{N^T} \\ \sigma_{yy}^{N^T} \\ \sigma_{xy}^{N^T} \end{Bmatrix}^{(k)} = \frac{1}{t} \begin{Bmatrix} N_{xx}^T \\ N_{yy}^T \\ N_{xy}^T \end{Bmatrix} \tag{4-16}$$

where t is the lamina thickness.

The thermal bending stress in the k^{th} lamina, $\left\{\sigma^{M^T}\right\}^{(k)}$, can be calculated by dividing the force per unit width by the lamina thickness,

$$\left\{\sigma^{M^T}\right\}^{(k)} = \begin{Bmatrix} \sigma_{xx}^{M^T} \\ \sigma_{yy}^{M^T} \\ \sigma_{xy}^{M^T} \end{Bmatrix}^{(k)} = \frac{1}{t \cdot D^{(k)}} \begin{Bmatrix} M_{xx}^{T} \\ M_{yy}^{T} \\ M_{xy}^{T} \end{Bmatrix} \tag{4-17}$$

where $D^{(k)}$ is the moment arm, $D^{(k)} = z^{(k)} + \frac{t}{2}$.

4.4 Thermal Loading Combined with Bending Conditions

Under the liner assumption, stress components of the combined bending with thermal loading are expressed to be the summation of the each mechanical and thermal loading components as expressed in (4-18).

$$\begin{aligned} \left\{\sigma^{Total}\right\}^{(k)} &= \begin{Bmatrix} \sigma_{xx} \\ \sigma_{yy} \\ \sigma_{xy} \end{Bmatrix}^{(k)} + \begin{Bmatrix} \sigma_{xx}^{N^T} \\ \sigma_{yy}^{N^T} \\ \sigma_{xy}^{N^T} \end{Bmatrix}^{(k)} + \begin{Bmatrix} \sigma_{xx}^{M^T} \\ \sigma_{yy}^{M^T} \\ \sigma_{xy}^{M^T} \end{Bmatrix}^{(k)} \\ &= z \begin{bmatrix} \overline{Q}_{11} & \overline{Q}_{12} & 0 \\ \overline{Q}_{12} & \overline{Q}_{22} & 0 \\ 0 & 0 & \overline{Q}_{66} \end{bmatrix}^{(k)} \begin{Bmatrix} -\frac{\partial^2 w_0}{\partial x^2} \\ -\frac{\partial^2 w_0}{\partial x^2} \\ -2\frac{\partial^2 w_0}{\partial x \partial y} \end{Bmatrix} + \frac{1}{t} \begin{Bmatrix} N_{xx}^{T} \\ N_{yy}^{T} \\ N_{xy}^{T} \end{Bmatrix} + \frac{1}{t \cdot D^{(k)}} \begin{Bmatrix} M_{xx}^{T} \\ M_{yy}^{T} \\ M_{xy}^{T} \end{Bmatrix} \\ &= \frac{z}{b} \begin{bmatrix} \overline{Q}_{11} & \overline{Q}_{12} & 0 \\ \overline{Q}_{12} & \overline{Q}_{22} & 0 \\ 0 & 0 & \overline{Q}_{66} \end{bmatrix}^{(k)} \begin{bmatrix} D_{11}^{*} & D_{12}^{*} & D_{16}^{*} \\ D_{12}^{*} & D_{22}^{*} & D_{26}^{*} \\ D_{16}^{*} & D_{26}^{*} & D_{66}^{*} \end{bmatrix} \begin{Bmatrix} M_{xx} \\ 0 \\ 0 \end{Bmatrix} + \frac{1}{t} \begin{Bmatrix} N_{xx}^{T} \\ N_{yy}^{T} \\ N_{xy}^{T} \end{Bmatrix} + \frac{1}{t \cdot D^{(k)}} \begin{Bmatrix} M_{xx}^{T} \\ M_{yy}^{T} \\ M_{xy}^{T} \end{Bmatrix} \end{aligned} \tag{4-18}$$

where $\left\{\sigma^{Total}\right\}^{(k)}=$ total stress in the k^{th} lamina.

However, this linear assumption is over-simplified the problem enough to apply the super-position method. The linearity, while adding the bending stresses and thermal stresses, should be checked again. From elastic and thermo-elastic constitutive equation,

$$\sigma_j^M = C_{ij}\varepsilon_i^M \tag{4-19}$$

$$\sigma_j^T = C_{ij}[\varepsilon_i^T - \alpha_i(T - T_0)] \tag{4-20}$$

where

σ_j^M is the stresses induced by mechanical loading.

σ_j^T is the stresses induced by thermal loading.

ε_i^M is the strains induced by mechanical loading.

ε_i^T is the strains induced by thermal loading.

C_{ij} is the plane-stress reduced stiffness tensor.

Let's consider the case that a mechanical loading is first applied followed by thermal loading. The constitutive equation, when thermal loading is applied after mechanical loading, is expressed as follows.

$$\varepsilon_i^{Total} = S_{ij}\sigma_j^{Total} + \alpha_i(T - T_0) \tag{4-21}$$

where

$$\sigma_j^{Total} = \sigma_j^T + \sigma_j^M$$

and

$$\sigma_j^{Total} = C_{ij}[\varepsilon_i^{Total} - \alpha_i(T - T_0)] \tag{4-22}$$

where

$$\varepsilon_j^{Total} = \varepsilon_j^T + \varepsilon_j^M$$

On the other hand, if the thermal loading is first applied followed by mechanical loading, then the constitutive equation is

$$\varepsilon_i^{Total} = S_{ij}\sigma_j^{Total} \tag{4-23}$$

where

$$\sigma_j^{Total} = \sigma_j^T + \sigma_j^M$$

and

$$\sigma_j^{Total} = C_{ij}\varepsilon_i^{Total} \tag{4-24}$$

where

$$\varepsilon_j^{Total} = \varepsilon_j^T + \varepsilon_j^M$$

Comparing 4-(20) with 4-(22), the strain when the mechanical loading was first applied followed by the thermal loading is higher than that of the opposite order by $\alpha_i(T - T_0)$. The stress is also higher when the mechanical loading was applied first than when the thermal loading was applied first by $C_{ij}\alpha_i(T - T_0)$. The linearity condition can

be acceptable when the $\alpha_i(T-T_0)$ and $C_{ij}\alpha_i(T-T_0)$ are very small comparing to thermal (or mechanical) strain and thermal (or mechanical) stress, respectively.

4.5 Thermo-Viscoelastic Constitutive Equations

Normally, polymers exhibit viscoelastic properties caused by their relaxation properties. In order to characterize the damage of polymer composites under the combined non-isothermal condition with mechanical loading, An analytical study of thermo-viscoelastic constitutive equation is necessary.

The thermoelastic constitutive equation,

$$\varepsilon_{ij}^{(k)} = S_{ijpq}^{(k)}\sigma_{pq}^{(k)} + \alpha_{ij}^{(k)}(T-T_0) \tag{4-25}$$

should be changed to be the following equation when we consider the thermo-viscoelastic condition.

$$\varepsilon_{ij}^{(k)} = S_{ijpq}^{(k)}\sigma_{pq}^{(k)} + \int_0^t \alpha_{ij}^{(k)}(\xi-\xi')\frac{\partial \Delta T}{\partial \tau}d\tau \tag{4-26}$$

where ξ and ξ' are the reduced time, defined by:

$$\xi = \xi(t) \equiv \int_0^t \frac{1}{a_T}d\tau$$

$$\xi' = \xi(\tau) \equiv \int_0^\tau \frac{1}{a_T}d\tau$$

The temperature shift factor, $a_T = a_T[T(\tau)]$

Schapery [84] called the problem the thermo-rheologically complex, which deals with any viscoelastic material whose temperature dependence cannot be characterized by the thermo-rhelogically simple representation. A few researches have been done with the thermo-viscoelastic approach in polymer/polymer composite materials. In this study, the lack of data in time dependent thermal and mechanical properties make it difficult to go further for the analytical approach with thermo-viscoelastic equation.

The uni-axial nonlinear viscoelastic constitutive equation of Schapery can be written for an isotropic material as

$$\varepsilon_{ij}^{(k)} = g_0^t S_{ijpq}^{(k)} \sigma_{pq}^{(k),t} + g_1^t \int_0^t \Delta S_{ijpq}^{(k)}(\xi - \xi') \frac{\partial}{\partial \tau}(g_2^\tau \sigma_{pq}^{(k),\tau}) d\tau \tag{4-27}$$

where

$S_{ijpq}^{(k)}$ is the instantaneous elastic compliance.

$\Delta S_{ijpq}^{(k)}(\xi)$ is a transient creep compliance function modeled by a Prony series:

$$\Delta S_{ijpq}^{(k)}(\xi) = \sum_{r=1}^{k} (S_{ijpq}^{(k)})_r [1 - e^{-\lambda} r^{\xi}] \tag{4-27}$$

ξ and ξ' are the reduced time scale parameter, defined by

$$\xi = \xi(t) \equiv \int_0^t \frac{1}{a_T} d\tau$$

$$\xi' = \xi(\tau) \equiv \int_0^\tau \frac{1}{a_T} d\tau$$

τ is the relaxation time.

The temperature shift factor, $a_T = a_T[T(\tau)]$

The viscoelastic thermal expansion term can be added to the uni-axial constitutive equation and can be expressed as

$$\varepsilon_{ij}^{(k)} = g_0^t S_{ijpq}^{(k)} \sigma_{pq}^{(k),t} + g_1^t \int_0^t \Delta S_{ijpq}^{(k)}(\xi - \xi') \frac{\partial}{\partial \tau}(g_2^\tau \sigma_{pq}^{(k),\tau}) d\tau + \int_0^t \alpha_{ij}^{(k)}(\xi - \xi') \frac{\partial \Delta T}{\partial \tau} d\tau \quad (4\text{-}28)$$

4.6 Thermocouple Attachment

Ten thermocouples of the foil thickness types (CO2-K, OMEGA) were used to check the temperature anisotropy of aluminum block and measure the surface temperatures of the specimen. Each temperature at five different points along the radial direction at both bottom and top of the specimen was measured. The thermal gradient through the thickness is not considered. The average values of top and bottom surface temperature are considered to be the reference temperature data. Due to the difficulties to embed thermocouples into the mid-surface, which is located at 0.25mm from bottom surface of the specimen, the mid-surface temperatures are assumed to be the average of the top and bottom surface temperature. Maximum difference between top and mid surface is around 20^{o}C at the desired maximum temperature. Surface temperature profiles of the specimen from -196 to 250 ^{o}C are shown in the Figures 4.9 and 4.10.

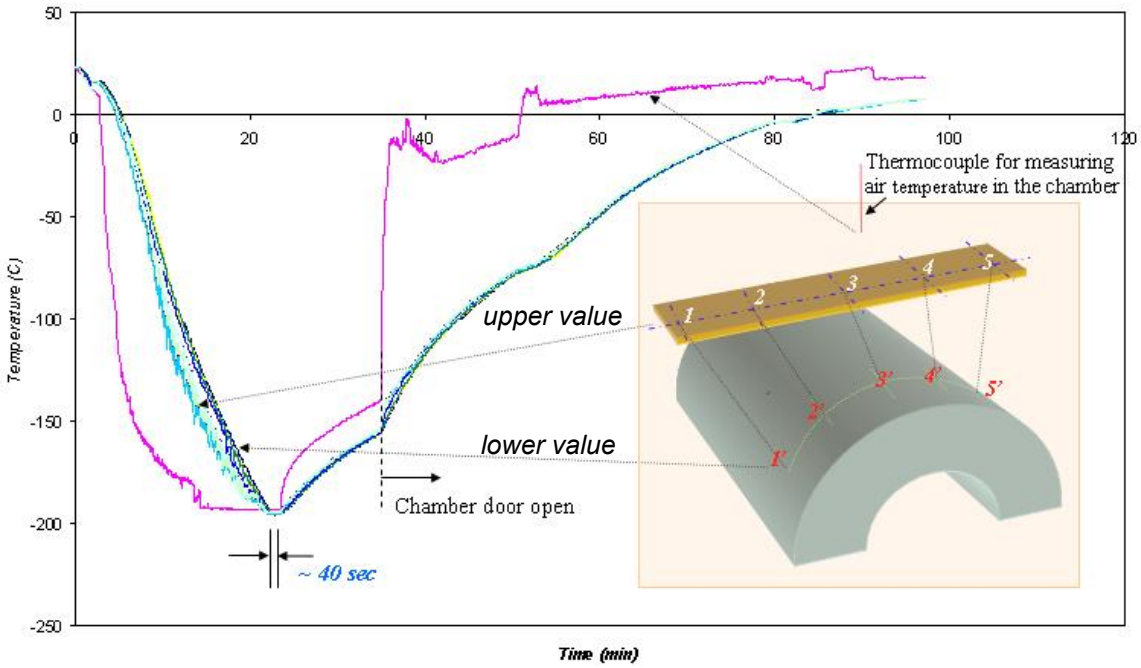

Figure 4.9. *Temperature profile from 23 to -196°C*

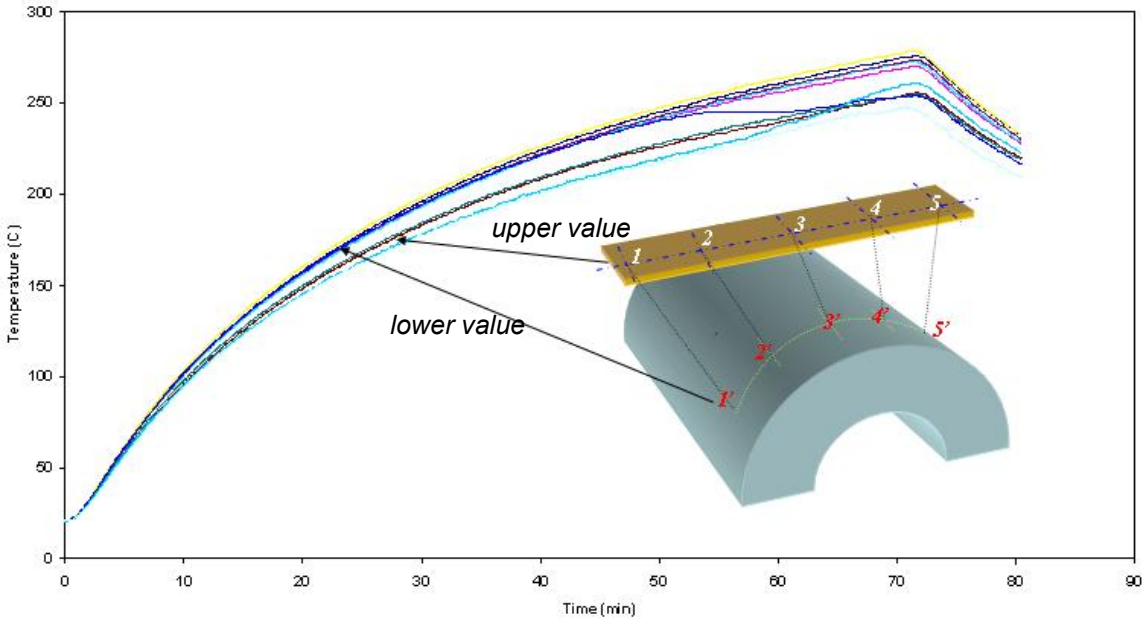

Figure 4.10. *Bottom and top surface temperature profile from 23 to 250°C*

4.7 Stress-Thermal Cycling

The mechanical loading combined thermal cycling tests were performed with the apparatus introduced in this chapter. Cryogenic thermal cycling starts from room temperature and down to cryogenic temperatures and then goes back to room temperature (Figure 4.11). In order to prevent thermal shock by direct contact with liquid nitrogen on the samples, resulting in thermal shock by rapid cooling to cryogenic temperatures, convection based cooling is applied to make the samples' temperature cool relatively slowly down. Temperature was measured by LabView (National Instrument Co.) with a scanning rate 1.0 scan/sec. The scanned samples were averaged for every 60 data and the average data were recorded every one minute. The time taken to reach the temperature of the sample -196^{o}C from room temperature was 30 ± 2.58 minutes and the cooling rate was 7.56 ± 1.50 ^{o}C/min. After cooling down to the -196^{o}C, the temperature was held for 5.8 ± 1.78 minutes, then the temperature was increased back to the room temperature with two different temperature increasing rates: The lower temperature increasing rate was 1.033 ± 0.639 ^{o}C/min and the higher one was 4 ± 1.58 ^{o}C/min as shown in Figures 4.11 and 4.12, respectively.

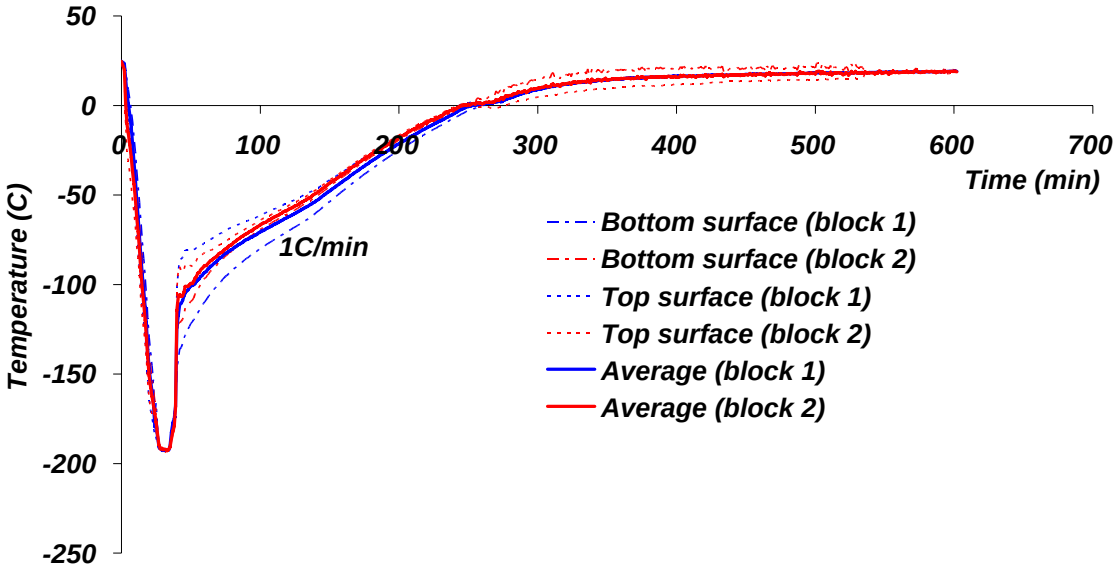

Figure 4.11. *Temperature profile from room temperature to cryogenic and back to the room temperature with lower temperature increasing rate (1.033 ± 0.639 °C/min)*

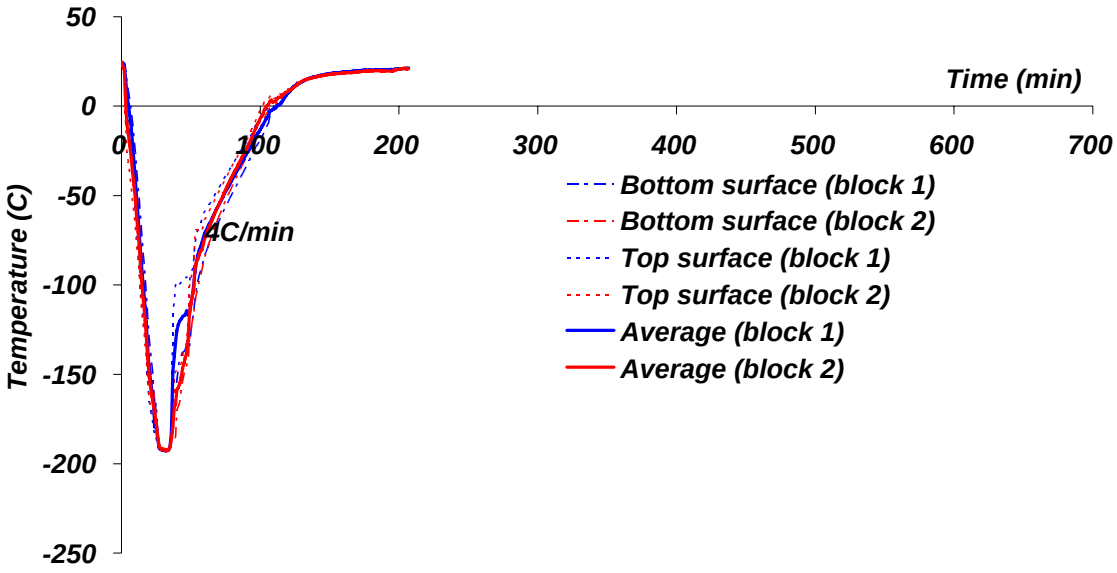

Figure 4.12. *Temperature profile from room temperature to cryogenic and back to the room temperature with higher temperature increasing rate (4 ± 1.58 °C/min)*

Heating the samples by conduction from room temperature to 250°C is performed with two different temperature increasing rates as well shown in Figures 4.13 and 4.14. Because the resistances of the heater between the two blocks are different, in order to be consistent in the power dissipation between the two heating blocks, different voltages from the two different transformers are applied at every step while heating up.

$$P = \frac{V^2}{R} \tag{4-29}$$

where

P = the rate of energy loss or the power dissipation

V = voltage [V]

R = resistance [Ω]

Periods to stay in a specific voltage to maintain a constant heating rate are different according to the block's electrical resistances. Table 4.1 shows empirical periods to stay in order to maintain 1°C/min heating rate when increasing the temperature up to 250°C.

Table 4.1. *Time schedule and corresponding voltage input for slow heating from room temperature to 250°C*

Time to stay in specific voltage (min)	*Block 1 Voltage [V] for resistance of 26.6 Ω*	*Block 2 Voltage [V] for resistance of 18.7 Ω*
20	*42.6 (40%)*	*32.18 (30%)*
20	*49.2 (45%)*	*37.4 (42.5%)*
30	*55.2 (50%)*	*50.3 (46%)*
30	*60.1 (55%)*	*56.3 (51%)*
20	*66.1 (60%)*	*61.5 (56%)*
20	*71.9 (65%)*	*67.3 (61%)*
20	*77.7 (70%)*	*69.9 (63%)*
20	*83.2 (75%)*	*77.5 (70%)*
20	*89.4 (80%)*	*84.3 (76%)*
20	*94.6 (85%)*	*89.7 (81%)*
20	*100.4 (90%)*	*94.6 (85%)*
20	*(95%)*	*96.2 (86%)*
20	*111.6 (100%)*	*98.1 (88%)*

With a careful manipulation of voltage control, heating from room temperature to 250°C was applied. 1.033 ± 0.218 and 4 ± 0.103 °C/min of heating rates were applied as shown in Figure 4.12 and 4.13, respectively. After 10 minutes of holding at the high temperature, a fan is switched on and the samples start cooling down to the room temperature.

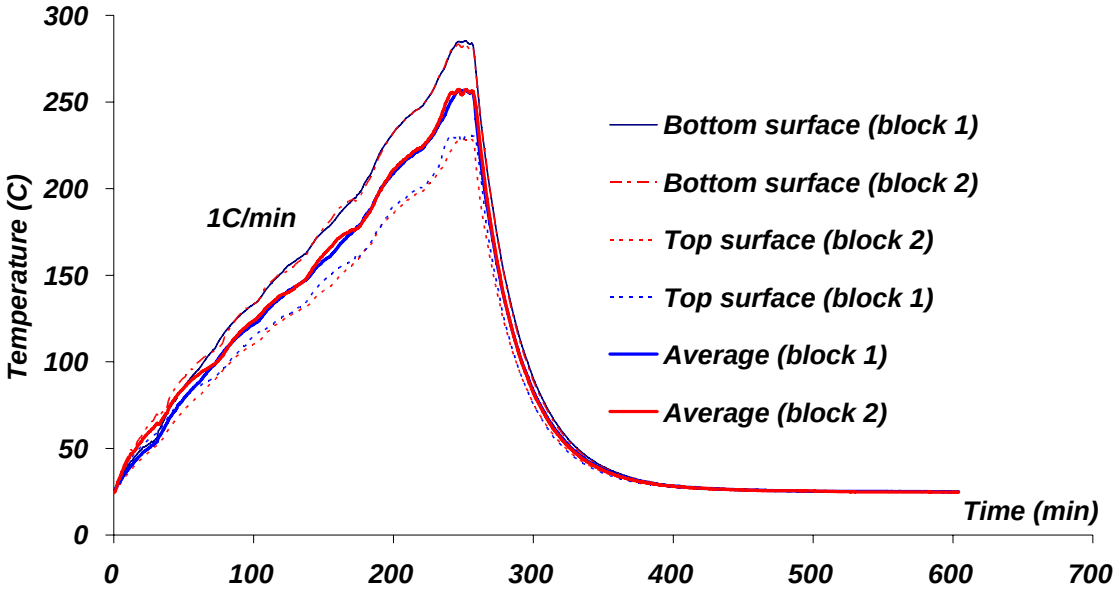

Figure 4.13. *Temperature profile from room temperature to 250°C and back to the room temperature with lower heating rate (1.033± 0.218 °C/min)*

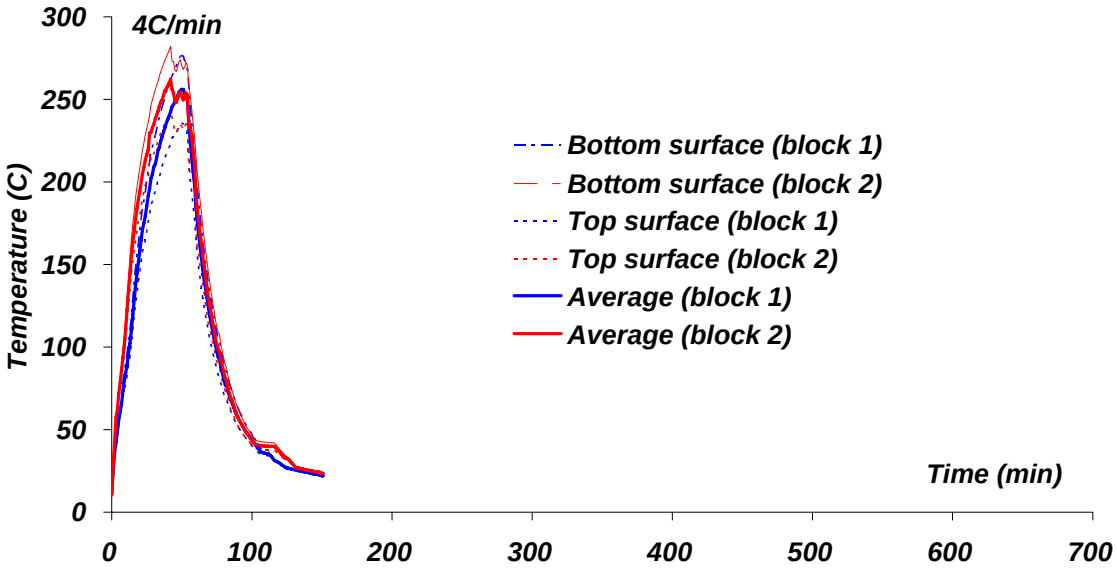

Figure 4.14. *Temperature profile from room temperature to 250°C and back to the room temperature with higher heating speed (4 ± 0.103 °C/min)*

The planned test matrix consists of the following parameters;

- *Three* different strain conditions with respect to the neutral axis: 0%, -0.35 to 0.35%, and -0.65 to 0.65%
- *Five* different thermal cycling experiments:

  (1) -196°C to 23°C

(2) 23°C to (i) 150°C, (ii) 200°C, (iii) 250°C

(3) -196°C to 250°C

- *Four* types of heating rates: 1°C/min, 2°C/min, 3°C/min and 4°C/min
- *Four* different thermal cycles: 1, 2, 4, 8

The maximum experimental time from the -196°C to 250°C thermo-cycling temperature profile, with the minimum temperature increasing rate (1°C/min), and the maximum number of cycles (8 cycles), was 93 hours. All specimens are held under a mechanical strain condition even though the thermal cycling is completed in order to make mechanical loading conditions be the same in all cases.

4.8 Characterization of Damage

4.8.1 Sample Preparation for Microscopy

In order to preserve the loading conditions while observing the crack damage, a wax mock-up having a concave shape of the deformed specimen was built by a molding technique. After putting specimen into the wax mock-up, epoxy (mixed five parts by weight of No. 20-8130 Epoxicure resin, Buehler Co. to one part by weight of No. 20-8132 Epoxicure hardener, Buehler Co.) was poured and cured for eight hours at room temperature. After detaching the solidified epoxy from the wax mock-up, the epoxy with the embedded specimen is cut roughly as a rectangular shape. Then, the roughly cut rectangular shaped epoxies were attached to a glass, cut again into slices with a diamond

saw (thickness 1mm) and polished to take microphotographs. The schematic of the procedures is shown in Figure 4.15.

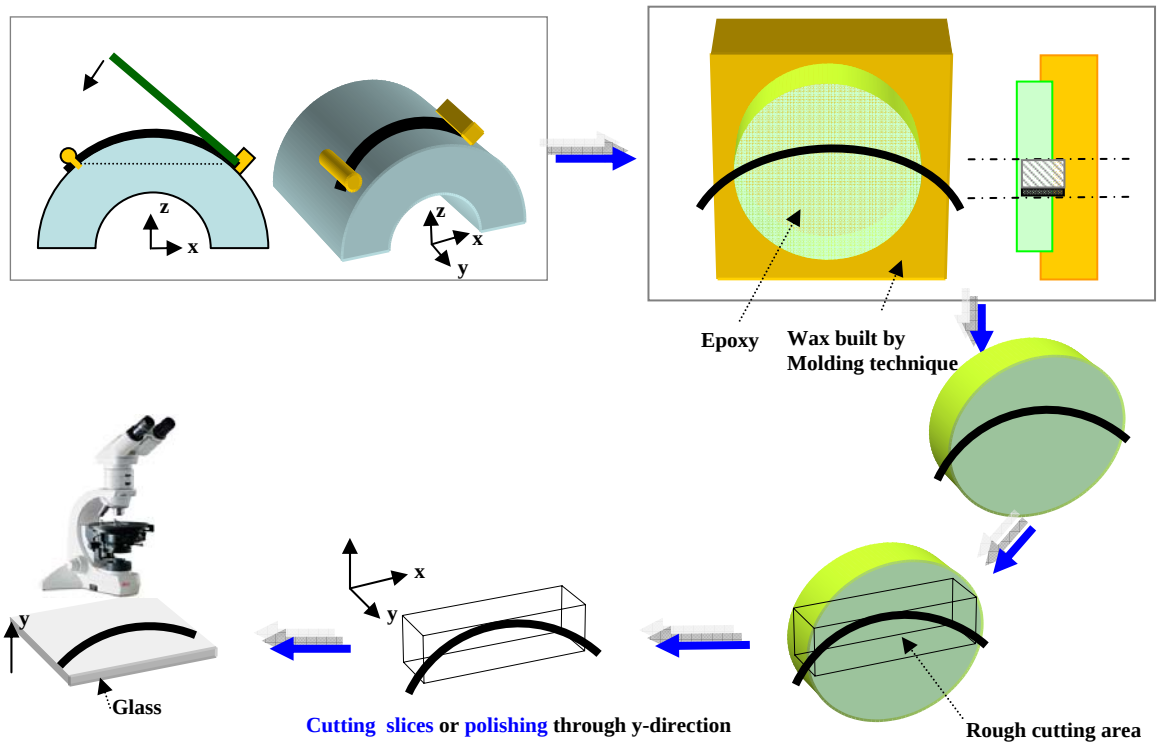

Figure 4.15. *Sample preparation process for microscopy*

After mounting sample with epoxy, 60mm of middle part of the sample is cut and investigated with the Nikon optical microscope for the characterization of damage shown in Figure 4.16. The reason to cut the both end-parts of the sample is that the clamping and supporting parts might cause local stresses while samples were bent or constrained with thermal loading, thus those parts should be excluded from our observation in order to make investigating parts consistent to the global in-plane stress condition.

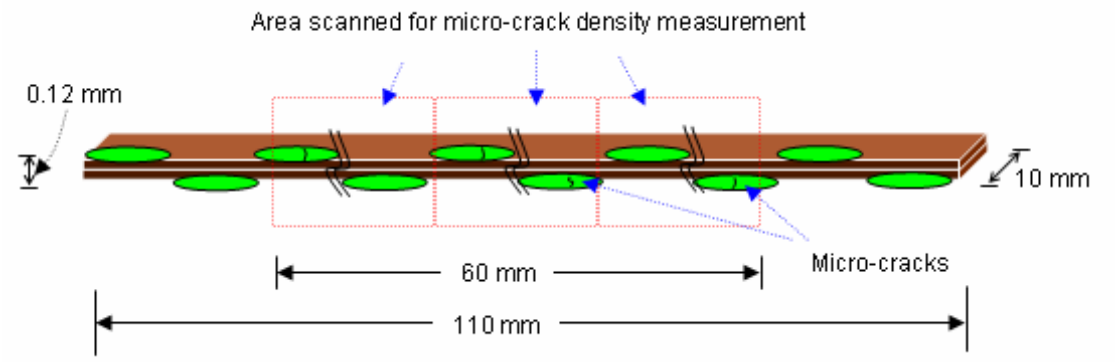

Figure 4.16. *Sample section area to be observed*

Mounted specimens are grounded to half width and cracks are counted in order to get a crack density data which are free from stress concentration and singularities near the free edges of the composite laminates.

Figures 4.17 and 4.18 demonstrate samples' in-plane strain and stress values under mechanical and/or thermal loading condition. During the cryogenic thermo-cycling, both upper and lower stresses are experiencing tension associated with the cryogenic temperature induced thermal stress (Figure 4.17). However, at the high temperature thermo-cycling condition, the lower 90^{o} layers of both blocks are under compression condition at the high temperature peak (Figure 4.18). Those resultant compressive stresses at the lower layer make it difficult to evaluate stress condition inducing lamina cracks. Therefore, only upper 90^{o} layers are selected for crack density observation.

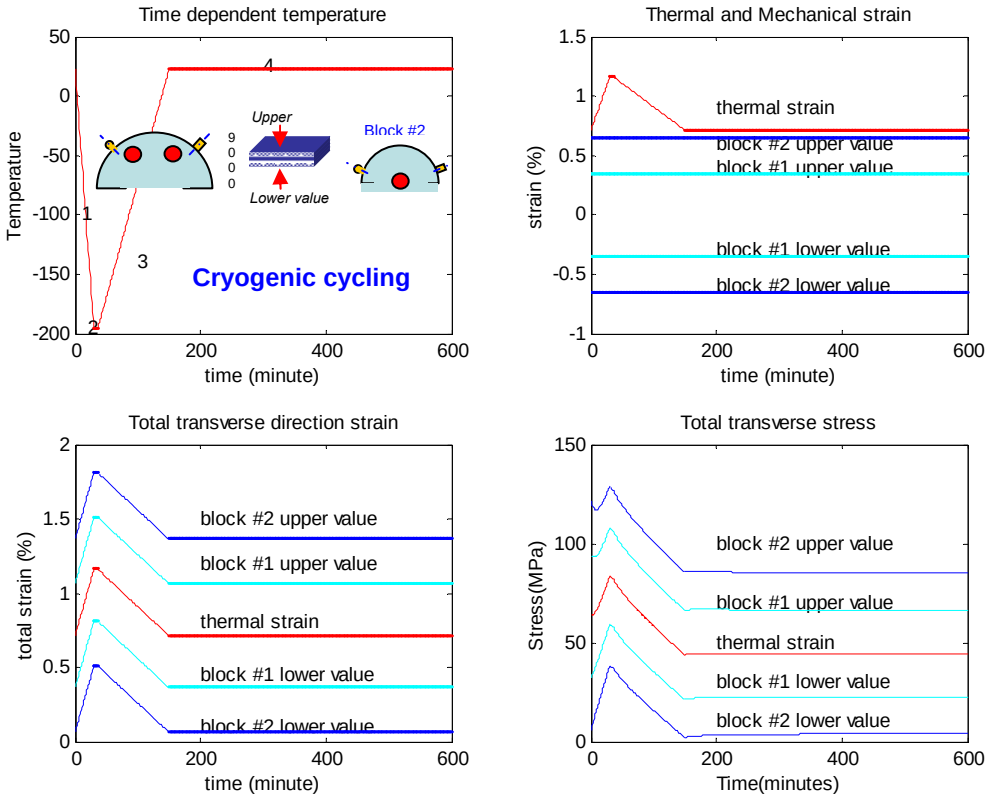

Figure 4.17. *Applied in-plane strain and stress associated with cryogenic temperature thermo-cycling temperature profile*

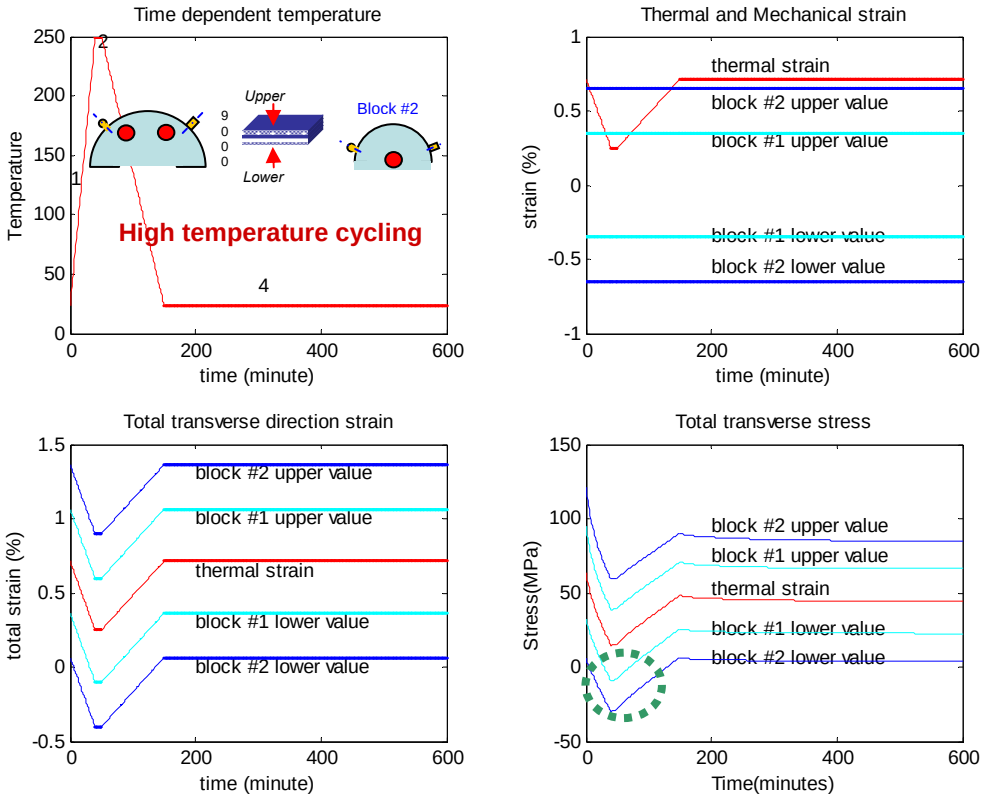

Figure 4.18. *Applied in-plane strain and stress associated with high temperature thermo-cycling temperature profile*

For monitoring of the microcrack development in the composites, a charge-coupled device (CCD) camera with microscope lens (2000x) was used to capture pictures and connected to a computer showing images of the microcracks. Figures 4.19 and 4.20 are example photo images of microcracks obtained by the CCD microscopy. Under the three different thermal cycling conditions and with or without strain, microcracks with different free strain conditions were observed, and the crack density is measured.

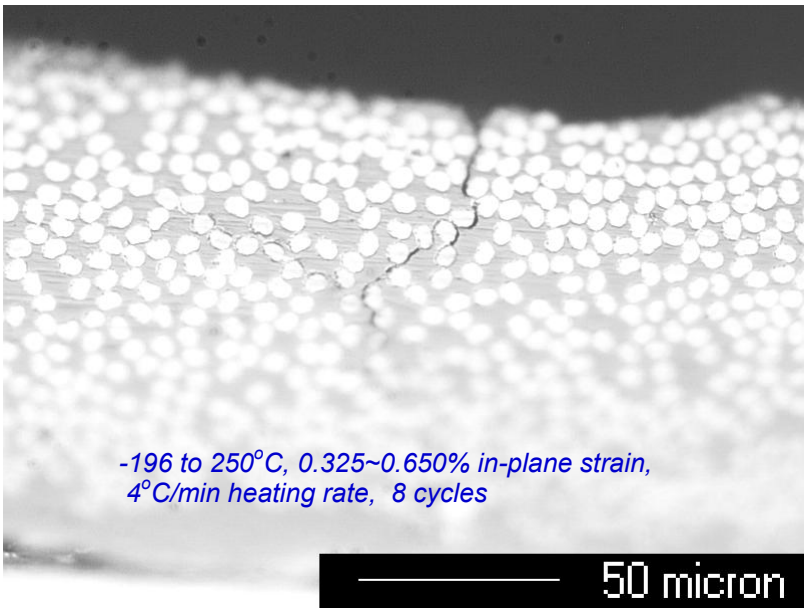

Figure 4.19. *Photo of transverse cracks developed after stress-thermal cycling (4000x)*

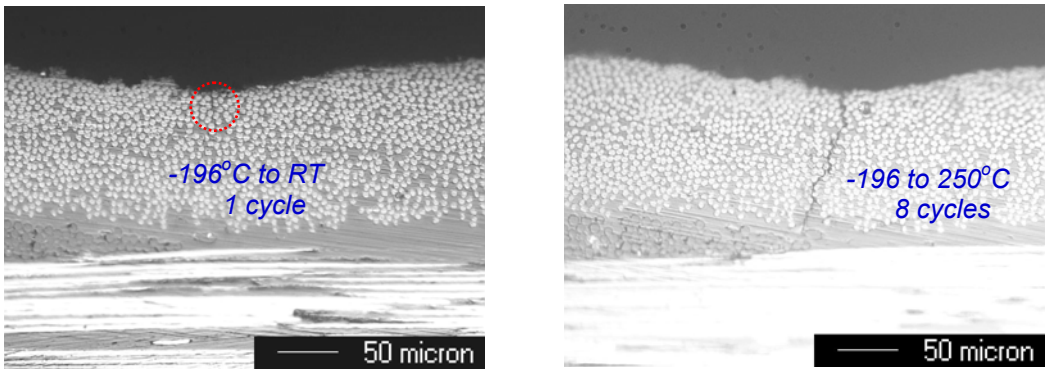

(a) 1°C/min temperature increasing rate, 0.325~ 0.650% of in-plane strain

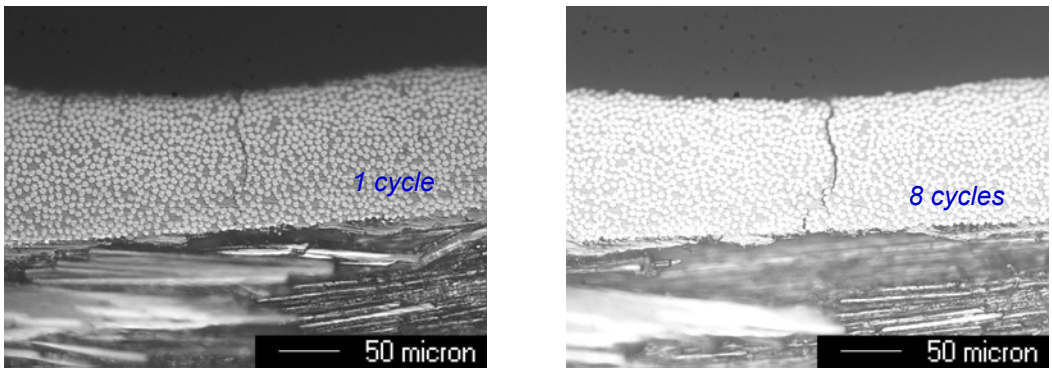

(b) -196 to 250°C, 1°C/min temperature increasing rate, 0.175~0.350% in-plane strain

Figure 4.20. *Photos of transverse crack growth with increasing number of thermal cycles*

4.8.2 Crack Quantification Using Image Analysis

The digital image processing technique is applied to quantify microcracks pixel by pixel. As examples, Figures 4.21 and 4.22 show the procedure to calculate the crack length from the image taken by two different lens multiplications using ImageJ (version 1.31j), a free software program provided by the National Institutes of Health (NIH). Manual superimposing of line along the crack length and auto-calculation of the length with pixel unit is the basic function of the software. Depending on the lens multiplication and the image size, the unit pixel with respect to physical length is derived and applied to ascertain the total length of cracks in a physical length scale.

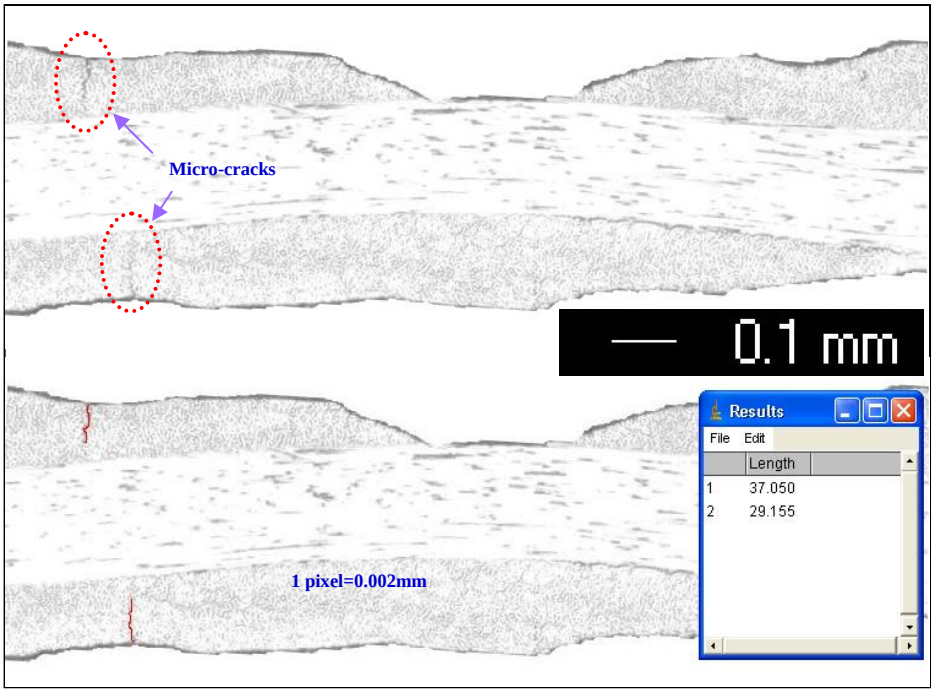

Figure 4.21. *Procedure to calculate crack length (500x, 800 by 600 image, 50 pixels = 0.1mm)*

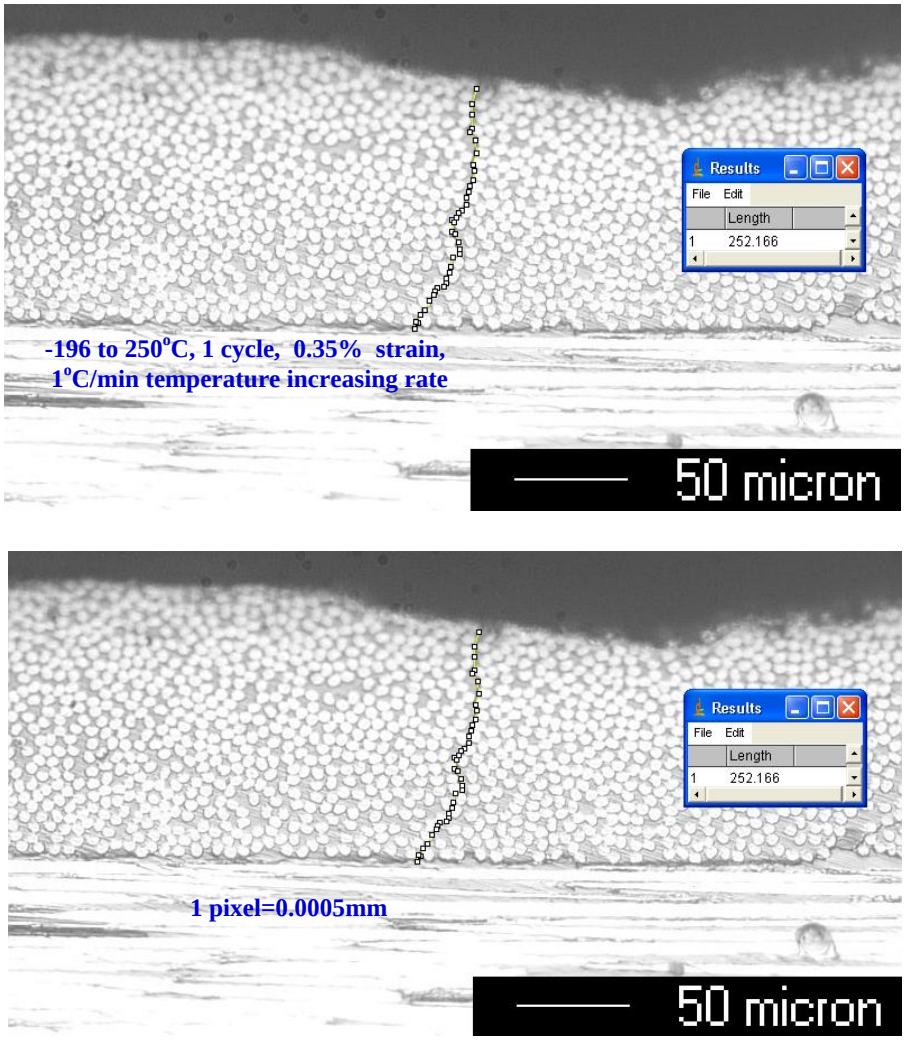

Figure 4.22. *Procedure to calculate crack length (2000x, 800 by 600 image, 100 pixels = 50 micron)*

Because the tow areas are different along the length direction, individual areas were calculated using ImageJ and the total areas were calculated. As can be seen Figure 4.23, after superimposing a green color on fill tow areas and manipulating the green split image with a binary threshold, fill tow segmentation is performed (Figures 4.23 (a) and (b)). The areas of fill tows are also calculated by summing all pixels inside the outlined fill tow area features (Figure 4.23 (c)).

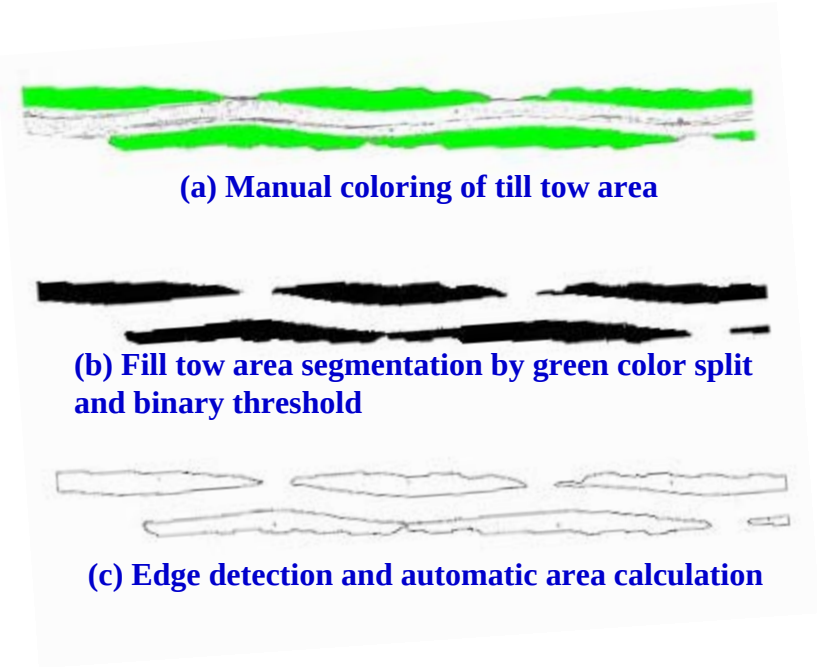

Figure 4.23. *Procedure to calculate tow area using image analysis*

From the information, crack densities are calculated by the equations 4-(30).

$$\text{Transverse crack density, } \delta^{crack} = \frac{\sum_{i=1}^{N^{crack}} l_i^{crack}}{\sum_{i=1}^{N} A_i} \qquad 4\text{-}(30)$$

where

l_i^{crack} is the i th crack length.

N^{crack} is the number of cracks.

A_i is the i th fill tow area.

N is the number of fill tow areas.

4.9 Water Absorption Test as a Non-Destructive Evaluation

Currently, widely used non-destruction evaluation (NDE) methods for composite damage are x-radiography and acoustic emission (AE). However their high cost sometimes makes them difficult to use. As an independent study to the stress-thermal cycling, the water absorption NDE methodology, which will be an easier and more cost effective damage evaluation test for M40J/PMR-II-50 uni-taped cross ply fabric composites will be pursued. The short term water uptake test for 24 hours in 80^{o}C after the thermal cycling test has been performed. The crack densities of specimens after the stress-thermal cycling can be evaluated by using the reference data of diffusion rates and saturation levels corresponding to various crack densities of M40J/ PMR-II-50 composite. Figure 4.24 shows the water absorption test procedure after each stress-thermal cycle.

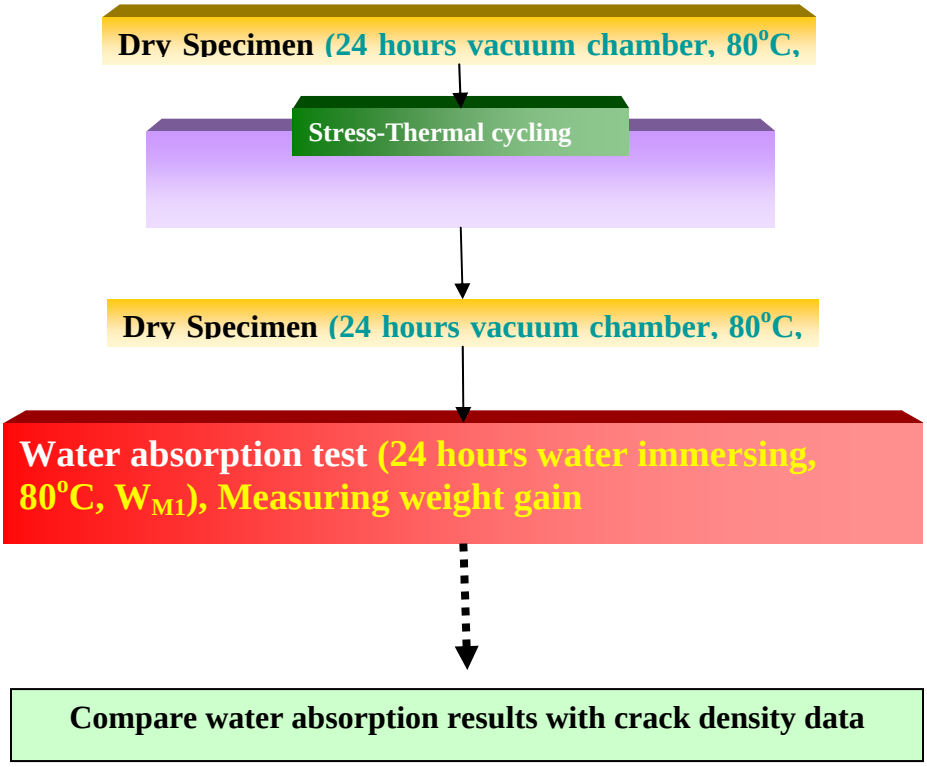

Figure 4.24. *Schematic of water absorption test procedure*

CHAPTER V

STATISTICAL EXPERIMENTAL DESIGN AND ANALYSIS

The experimental design technique is normally split into two parts; the planning or design of the experiment, and the statistical analysis of the results. In this chapter, the experimental planning, particularly designed to make sure that the statistical analysis gives the maximum information with the minimum experimental resources, will be shown. A test based on the planned experimental design will be introduced, followed by a description of how the effects of each factor and their interactions will be simply presented with a graphical tool. Following that, a statistical approach will be applied to make a decision of which of these factors are important in microcrack formation, and which may be attributable to experimental variation, or noise. Finally, an overview of the interpretation of the results of the analyses will be given.

5.1 Experimental Design: 2^k Factorial Designs

The 2^k factorial design is useful in the early stages of the experimental work as a factor for screening when there seem to be many factors to be investigated. One of the goals of this research is to find significant environmental factors that give rise to micro-cracking of M40J/PMR-II-50 composite under combined mechanical loading with thermal cycling. Empirically obtained probable factors causing microcracks of polymer

composites are mechanical loadings, thermo-cycling temperature profiles, temperature increasing rates, and number of thermal cycles.

The originally planned test matrix consists of the following parameters;

- *Three* different transverse mechanical strain conditions: 0%, 0.175 ~ 0.350%, and 0.325~0.650%
- *Five* different thermal cycling profiles:

  (1) -196^{o}C to 23^{o}C

  (2) 23^{o}C to (i) 150^{o}C, (ii) 200^{o}C, (iii) 250^{o}C

  (3) -196^{o}C to 250^{o}C
- *Four* temperature increasing rates: 1^{o}C/min, 2^{o}C/min, 3^{o}C/min, and 4^{o}C/min
- *Four* different number of cycles: 1, 2, 4, 8

Based on the concept of *one-factor-at-a-time* experiments, the total number of runs are $3\times5\times4\times4\times r = 240r$, where *r* stands for replicates of experiments. If *r* is 4, then the total number of runs is 960. It is very time and cost consuming to do the thermal cycling with the tremendous number of experimental runs. Therefore, a time and cost effective experimental design approach is required for getting the main effects and interaction effects among factors on microcracks.

One method to reduce extremely large number of runs is to use only two levels of each of the factors of interest. Using this approach to study *k* different factors, each having only *two* levels, the minimum number of experimental runs needed is 2^{k} , which is called **2^{k} factorial designs**. Based on the concept of 2^{k} factorial design, the test matrix for stress-thermal cycling is simplified as shown in Table 5.1. The test matrix consists of

four different row factors (strain levels, number of cycles, temperature increasing rate, and thermo-cycling temperature profiles) and two different column factors (low level and high level). Therefore, when the 2^k factorial design is applied to this experiment, basically, 16 ($=2^4$) runs are needed to identify the main effects and interaction effects on microcrack formation in the composites. Assuming replicates, *r*, is 4, the total number of runs is $64\,(=16\times 4)$.

Table 5.1. *2^4 experiment design set-up for studying the effects of four factors on the microcrack density*

Factor	Low Level (-1)	High Level (1)
A, Mechanical Strain (%)	0	0.64
B, Thermo-cycling temperature profiles	23 to -196^{o}C	23 to -196 to 250^{o}C
C, Number of Cycles	1	8
D, Temperature increasing rate (^{o}C/min)	1	4

Table 5.2. *Crack densities obtained after the mechanical loading combined thermal cycling experiment based on the 2^4 factorial design*

Run	A	B	C	D	Crack Density (1/mm)
1 (8)	-1	-1	-1	-1	0.098 ± 0.010
2 (6)	1	-1	-1	-1	0.182 ± 0.013
3 (10)	-1	1	-1	-1	0.192 ± 0.017
4 (16)	1	1	-1	-1	0.311 ± 0.035
5 (4)	-1	-1	1	-1	0.230 ± 0.022
6 (15)	1	-1	1	-1	0.427 ± 0.034
7 (7)	-1	1	1	-1	0.438 ± 0.038
8 (3)	1	1	1	-1	0.669 ± 0.035
9 (14)	-1	-1	-1	1	0.106 ± 0.014
10 (1)	1	-1	-1	1	0.187 ± 0.019
11 (12)	-1	1	-1	1	0.183 ± 0.033
12 (11)	1	1	-1	1	0.299 ± 0.041
13 (5)	-1	-1	1	1	0.265 ± 0.021
14 (13)	1	-1	1	1	0.420 ± 0.031
15 (2)	-1	1	1	1	0.484 ± 0.045
16 (9)	1	1	1	1	0.686 ± 0.046

( ) is the real test run number for randomization.
'-1' means the lower level.
'1' means the higher level.

Based on the Table 5.1, 16 crack densities were obtained with four repetitions for each run as shown in Table 5.2. While performing the experimental tests, the test runs were conducted in random order to help reduce the possible effects of unknown factors on the test results [53]. Figure 5.1 displays the crack densities in graphical view, showing the effects of the four factors and two levels based on the Table 5.2. Based on the graph, the number of thermo-cycles seems to be a significant factor to have an influence on the crack density. When the increased number of cycles is combined with -196 to 250^{o}C

thermo-cycling temperature profile, the effect seems to be more critical on the damage of the M40J/PMR-II-50.

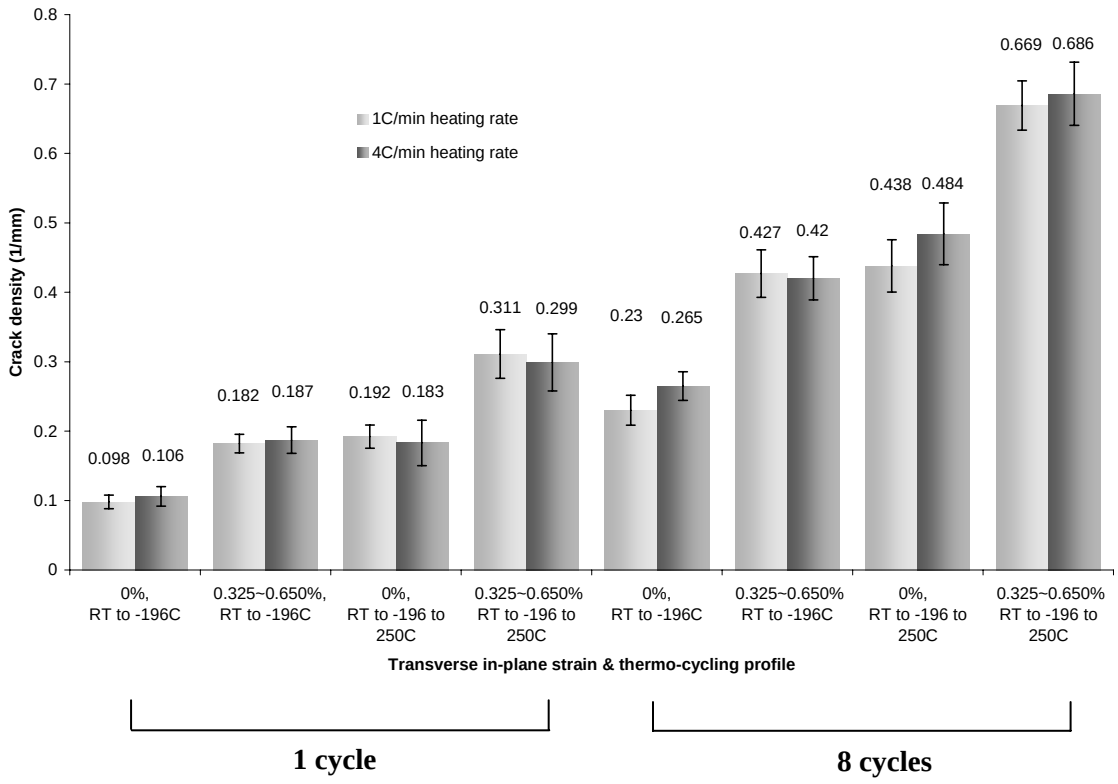

Figure 5.1. *Crack densities of M40J/PMR-II-50 induced by the mechanical loading combined with thermal cycling based on 2^k factorial design*

5.2 Analysis of the 2^k Factorial Design

After performing the experiment designed by the 2^k factorial method, estimation of all main effects and interaction effects should be performed by using a statistical procedure to sort the important effects from the unimportant ones. A normal probability plot of the effects was introduced in this study (Figure 5.2). The effects with magnitude close to zero are fit by a straight line. Only the effects that fall off the line or are not near the line are considered to be significant ones. Experimental errors or noise are thought to be effects falling near the line in the plot [53]. In Figure 5.2, the effects that fall off the line appear to be **C** (number of cycles), **B** (thermo-cycling temperature profile), **A** (mechanical strain), **BC** (interaction between thermo-cycling temperature profiles and number of cycles), and **AC** (interaction between mechanical strain and number of cycles). Particularly, **C** (number of cycles), **B** (thermo-cycling temperature profile), and **A** (mechanical strain) have a large positive effect on the crack density. In other words, changing **C**, **B**, or **A** from their low to high level causes a big increase in the crack density.

To justify that the factors, which were selected tentatively, are important, confidence interval for all the effects in the experiment are introduced by using equation (5-1).

$$\text{Confidence interval for effect } E\text{: } E \pm t_{a/2}(df = m)\sqrt{\frac{1}{m}\sum_{i=1}^{m} E_i^2} \qquad (5\text{-}1)$$

where m = *degree of freedom* and $\frac{1}{m}\sum_{i=1}^{m} E_i^2 \approx$ *variance of any effect.*

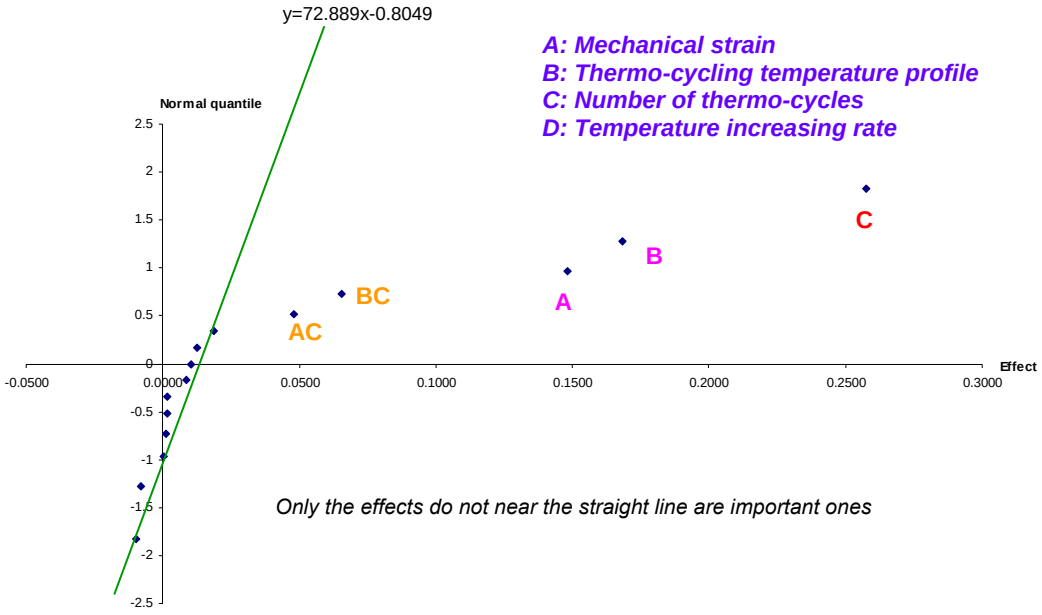

Figure 5.2 *Normal probability plot of the effects on crack densities of M40J/PMR-II-50*

Normal probability plot of Figure 5.2 shows that only a few single-factor main effects and two-factor interactions are likely to be significant in the present experiment. Consequently, it is reasonable to assume that three-factor and four-factor interactions are negligible and can be safely used to derive confidence intervals for all 15 effects. Combining these m=5 effects allows us to approximate the variance of any effect as follows:

Table 5.3. *Insignificant factors' effect and squared effect*

	Effect name	Effect estimate	Squared effect
1	D	0.0188	0.000353
2	AB	0.017	0.000289
3	AD	-0.0038	0.000014
4	BD	0.006	0.000036
5	CD	0.0028	0.000008
6	ABC	0.0222	0.000493
7	ABD	0.0028	0.000008
8	BCD	-0.0006	0.000000
9	ACD	-0.0079	0.000062
10	ABCD	0.011	0.000121

When determining the 95% confidence interval for any effect E as follows:

$$\begin{aligned} E \pm t_{q/2}(df = m) &= \sqrt{\frac{1}{m}\sum_{i=1}^{m} E_i^2} = E \pm t_{0.025} \cdot (5df) \cdot \sqrt{0.0001539} \\ &= E \pm 2.571 \cdot 0.012406 \\ &= E \pm 0.031896 \end{aligned} \tag{5-2}$$

Therefore, a 95% confidence interval for the AC effect is 0.0481 ± 0.03047 and this interval does not contain 0, resulting in conclusion that the AC effect is a significant factor in this experiment. Intervals of C ($0.2576 \pm 0.\ 031896$), B (0.1684 ± 0.031896), A (0.1478 ± 0.031896), BC ($0.0654 \pm 0.\ 031896$), and do not contain 0, which means they are all significant effects. Therefore, the most significant effects in modes of importance on crack-densities induced by the stress-thermal cycling are

- C (Number of cycles)
- B (Thermo-cycling temperature profile)
- A (Mechanical strain)
- BC (Interaction between thermo-cycling temperature profile and number of cycles)
- AC (interaction between mechanical strain and number of cycles)

Each significant factors can by quantified by calculating distances of each points from the line representing non-significant factors. Based on the Figure 5.3, a distance from a point (x_0, y_0) representing C, B, A, BC and AC to a line $ax + by + c = 0$ can be calculated from equation (5-3).

$$d = \frac{|ax_0 + by_0 + c|}{\sqrt{a^2 + b^2}} \tag{5-3}$$

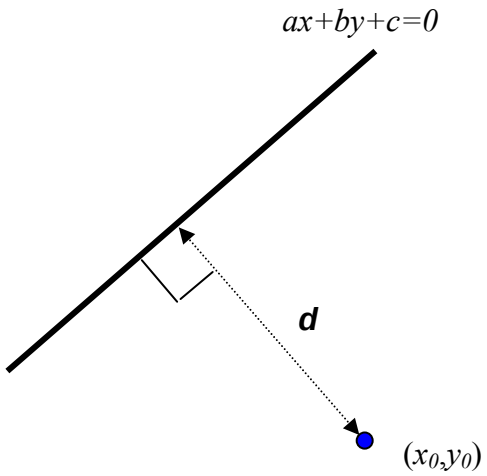

Figure 5.3. *Distance between a point and a line*

From the calculated distances, percentage of the each significant factor on micro-cracking is expressed as shown in Figure 5.4. The effect of C (number of thermo-cycles) was proved to be 41% on micro-cracking of the composite. The effect of B (thermo-cycling temperature profile) was 25% and the effect of A (mechanical strain) was 21%. BC (interaction of thermo-cycling temperature profile and number of thermo-cycles) and AC (interaction of mechanical strain and number of thermo-cycles) also had 7% and 5% of effect on lamina cracking, respectively.

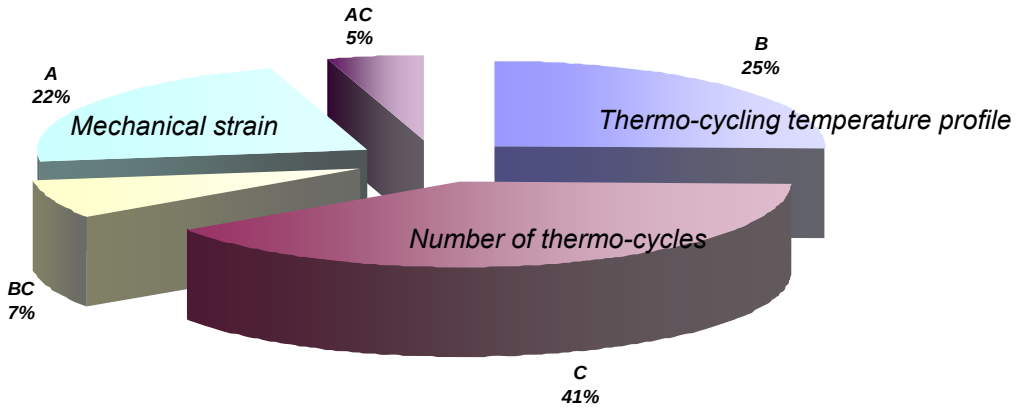

Figure 5.4. *Quantified significant effects*

5.3 Modified Test Plan

From the 2^k experimental analysis in the precious section, number of cycles, thermal cycling temperature profiles, and mechanical transverse strain were proved to be the most important factors. For more specific characterization of microcracking, intermediate levels of the three important factors were added to the test while sticking to one heating rate (4^{o}C/min). Figure 5.5 is the schematic of the modified test plan.

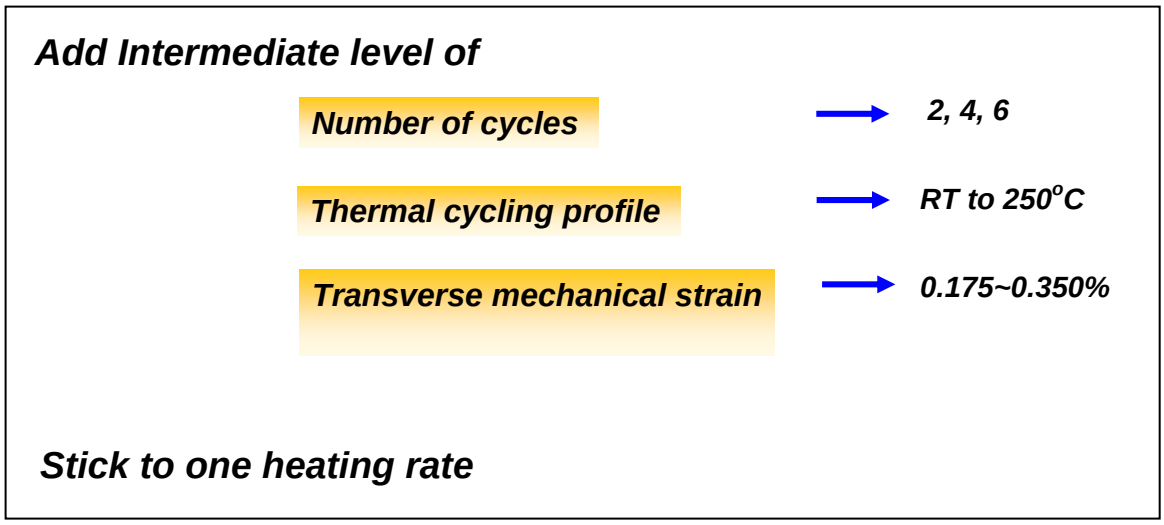

Figure 5.5. *A schematic of the modified test plan after 2^k experimental analysis*

23 to 250°C of thermo-cycling temperature profile and 0.175~0.350% of mechancal strain conditions were added to the original test plan. The synergistic test was done for both one and eight cycles and crack densities were measured (Figures 5.6 amd 5.7).

Figure 5.6 shows the crack density after one thermo-cycle. The crack density under the cryogenic temperature profile (room temperature to -196°C and back to the room temperature) showed the lowest one. High temperature profile (room temperature to 250°C and back to the room temperature) showed slightly higher crack densities (13 to 19% increase) than at the cryogenic temperature induced crack density. Cryogenic and high temperature combined thermo-cycling profile (room temperature to -196°C to 250°C and back to room temperature) showed the highest crack density and 40 to 44% increase compared to the high temperature profile.

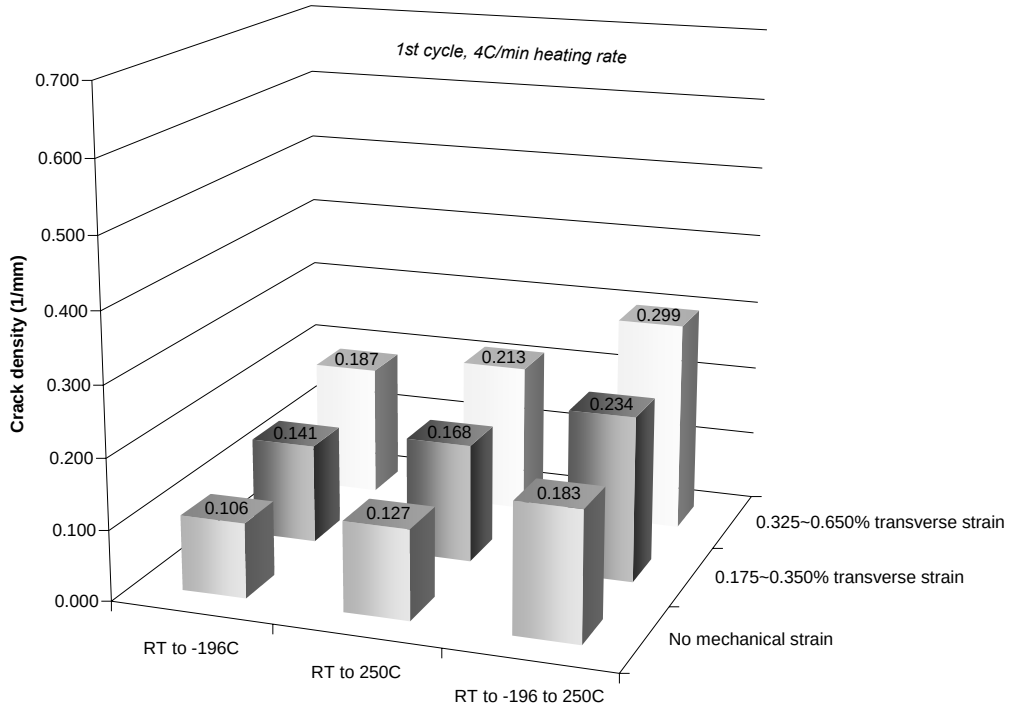

Figure 5.6. *Crack densities with three different thermo-cycling temperature profiles and transverse mechanical strains (1 cycle)*

Figure 5.7 shows the crack densities after eight thermo-cycles' run. The cryogenic temperature thermo-cycling profile induced a higher crack density than the high temperature thermo-cycling profile after eight cycles. The combined temperature thermo-cycling profile accelerated the crack propagation, resulting in 38 to 45% and 48 to 54% higher than the cryogenic and the high temperature thermo-cycling profiles, respectively.

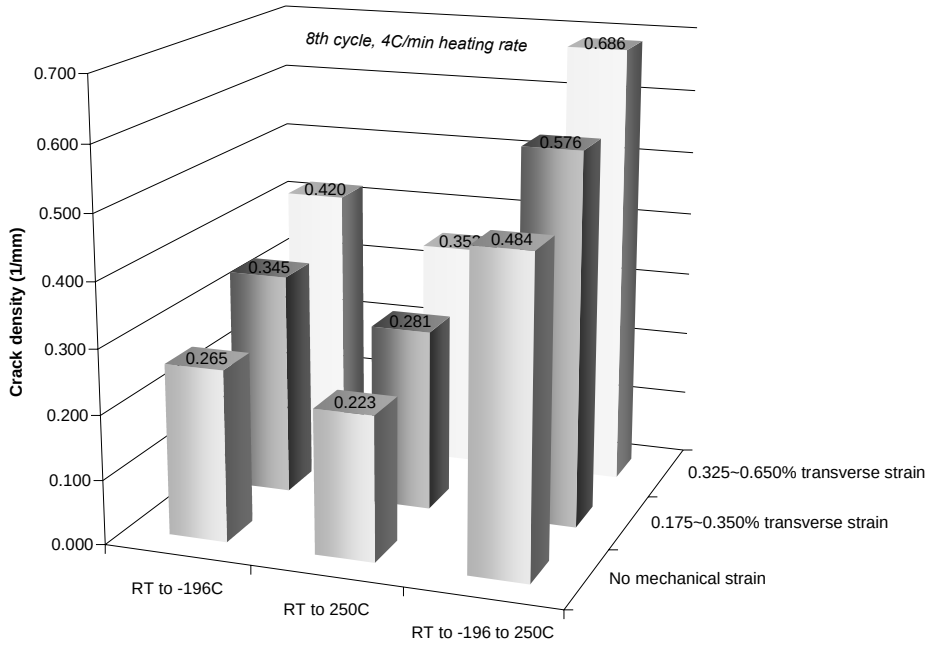

Figure 5.7. *Crack densities with three different thermo-cycling temperature profiles and transverse mechanical strains (8 cycles)*

Intermediate levels of number of cycles (2, 4, and 6) were added to the original test plan and the measured crack densities are shown in Figures 5.8 to 5.10.

All three thermo-cycling temperature profiles showed an increase of crack density with increasing number of thermo-cycles. The high temperature thermo-cycling profile showed a slow increase in crack density with increasing thermo-cycles (Figure 5.9). The combined thermo-cycling profile showed a rapid increase in crack density with increasing number of cycles compared to the other two thermo-cycling temperature profiles (Figure 5.10).

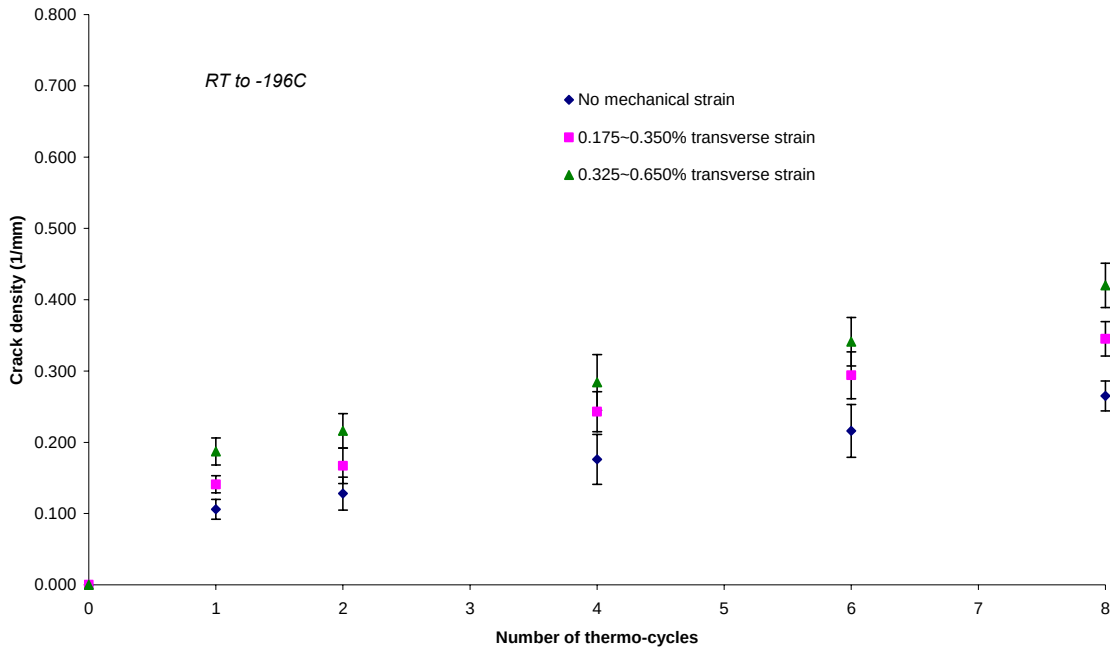

Figure 5.8. *Crack densities with increasing number of cycles (23 to -196^{o}C)*

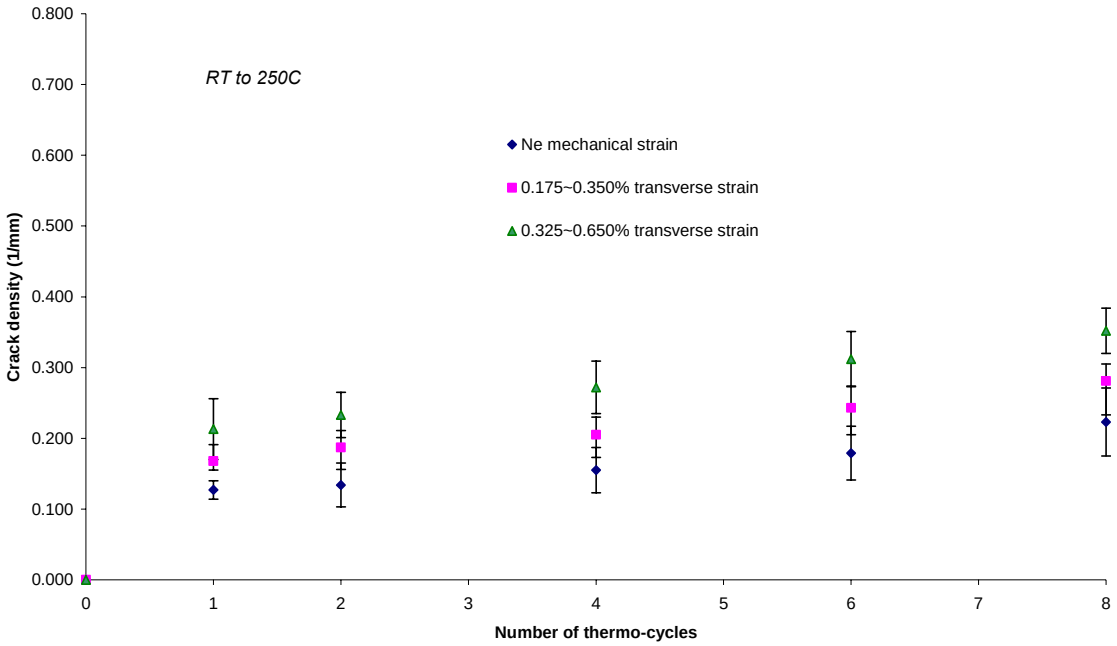

Figure 5.9. *Crack densities with increasing number of cycles (23 to 250°C)*

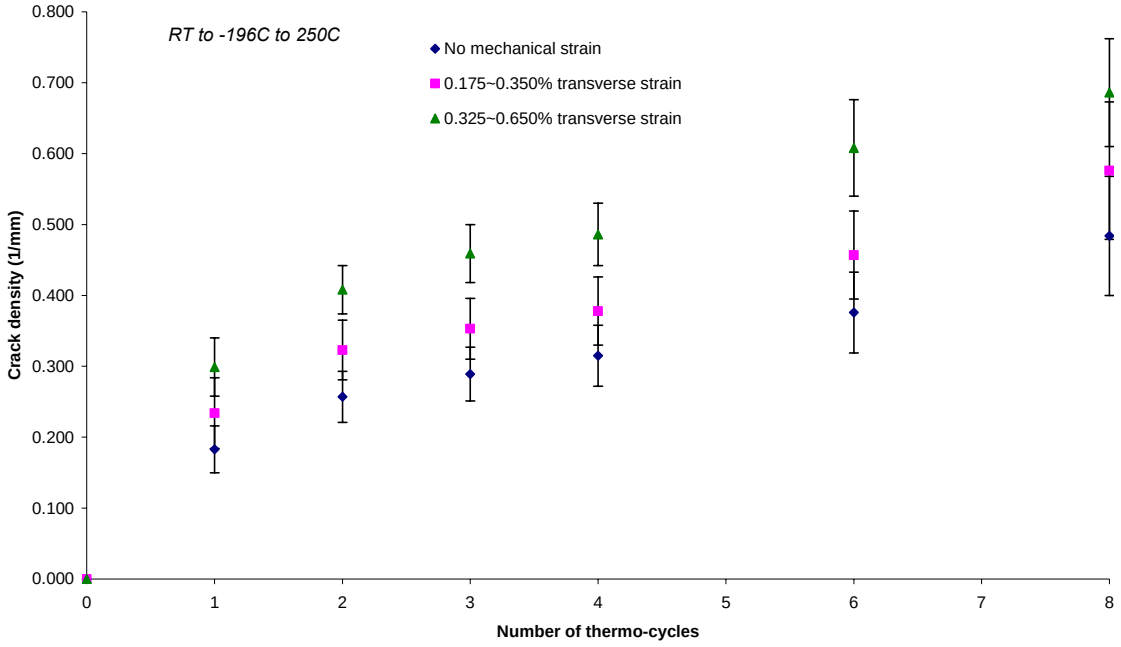

Figure 5.10. *Crack densities with increasing number of cycles (23 to -196°C to 250°C)*

CHAPTER VI

FAILURE MECHANISM AND ANALYTICAL STUDY ON COMPOSITE DAMAGE UNDER MECHANICAL LOADING COMBINED THERMAL CYCLING

Mechanical loading combined thermo-cycling from cryogenic to high temperatures causes the composite materials to have complex damage modes as a result of i) CTE mismatch induced thermal residual stress both in laminas and fiber/matrix while the composites are exposed to cryogenic temperature [85-87], ii) chemical and mechanical degradation of both polymer matrix and fiber/matrix interface at high temperature [88,89], iii) thermal fatigue with thermo-cycling and its combined effect with mechanical loading at low number of thermo-cycles, iv) thermal stress from transient temperature difference between the specimen core and edge, v) damage accumulation effect after initial cracking with increasing number of thermo-cycling, vi) visco-elastic effects, and vii) geometric non-homogeneity in both ply areas and fiber distribution in each ply. All the complex effects were combined in the present study. Number of thermo-cycles, thermo-cycling temperature profiles, mechanical transverse strains were the most important factors to cause damage on the M40J/PMR-II-50 composites using the statistical analysis shown in the previous chapter. In this chapter, discussions about how we could identify the main and interaction factors are introduced using mechanical, thermo-, and chemo- analysis.

6.1 Characterization of Crack Formation and Propagation Mechanism

Crack initiation was interfacial at both high and low temperature as shown in Figure 6.1. Debonding and linking of the debonding sites were observed during initial damage stage and during progression of damage stage, respectively.

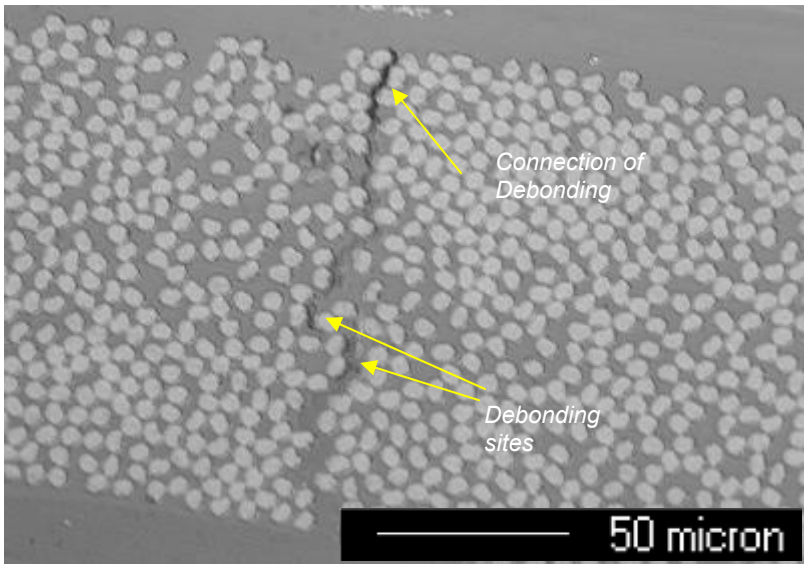

Figure 6.1. *Crack initiation with microcrack precursors*

At cryogenic temperatures, once a crack occurs, the crack propagates through the ply thickness because PMR-II-50 resin is extremely brittle, and it offers little resistance to crack propagation. But cracks in samples exposed to high temperatures rarely propagate through the whole ply thickness due to matrix ductility.

Damage induced by mechanical strain itself does not seem to be severe compared to the combined (high and low temperature) thermal damage.

6.2 Analytical Study of Time Dependent Non-Isothermal Linear Thermo-Viscoelasticity

When composites are exposed to higher or lower temperature than the reference (stress free) temperature, each layer expands or contracts depending on their lay-ups, if there are no constraints as shown in (b) in Figure 6.2. The layer of interest in this study is layer 4 (90^o). Fiber direction is along y-axis direction and the transverse direction to the fibers is along the x-axis direction in ply 4. Fiber direction tends to expand with decreasing temperature because the thermal expansion coefficient in the fiber direction is negative (-1.6E-6).

However, in the transverse direction to the fibers contraction is likely, as temperature decrease, since the thermal expansion coefficient (20.1E-6) is positive. Therefore, the strains in x- and y-direction are expressed by the equations (6-1) and (6-2) assuming no constraint conditions.

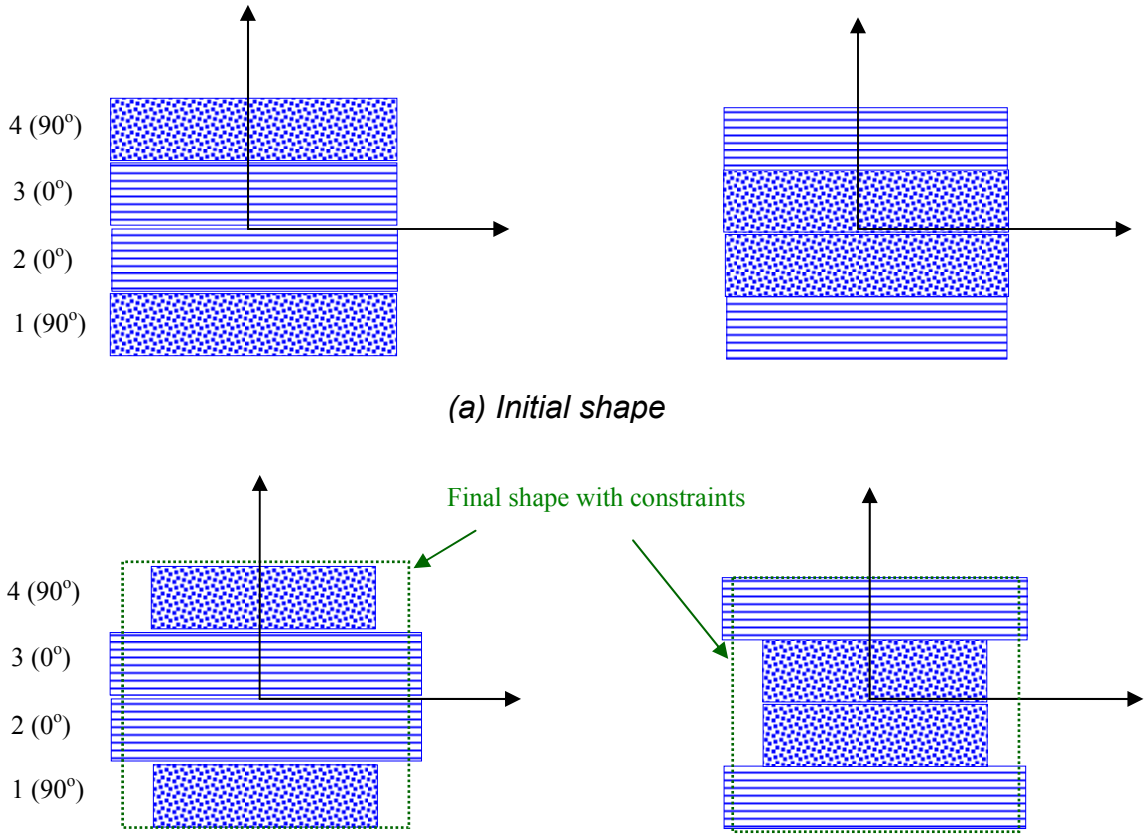

Figure 6.2. *Thermal expansion and contraction of layers with decreasing temperature assuming no constraint in x- and y-direction*

$$\begin{aligned}\varepsilon_x^T &= \varepsilon_2^{(4)} - \nu_{12}\varepsilon_1^{(4)} - \nu_{32}\varepsilon_3^{(4)} \\ &= \Delta T \cdot (\alpha_{22} - \nu_{12}\alpha_{11} - \nu_{32}\alpha_{33})\end{aligned} \tag{6-1}$$

where T notes 'Thermal'.

$$\begin{aligned}\varepsilon_y^T &= \varepsilon_1^{(4)} - \nu_{21}\varepsilon_2^{(4)} - \nu_{31}\varepsilon_3^{(4)} \\ &= \Delta T \cdot (\alpha_{11} - \nu_{21}\alpha_{22} - \nu_{31}\alpha_{33})\end{aligned} \tag{6-2}$$

Total strains are expressed as the sum of mechanical strain and thermal strain in equations (6-3) and (6-4).

$$\begin{aligned}\varepsilon_x^{Total} &= \varepsilon_x^M + \varepsilon_x^T \\ &= \varepsilon_x^M + [\varepsilon_2^{(4)} - \nu_{12}\varepsilon_1^{(4)} - \nu_{32}\varepsilon_3^{(4)}] \\ &= (\frac{\sigma_x^M}{E_{22}} - \nu_{12}\frac{\sigma_y^M}{E_{11}}) + \Delta T \cdot (\alpha_{22} - \nu_{12}\alpha_{11} - \nu_{32}\alpha_{33})\end{aligned} \tag{6-3}$$

where *M* notes 'Mechanical'.

$$\begin{aligned}\varepsilon_y^{Total} &= \varepsilon_y^M + \varepsilon_y^T \\ &= \varepsilon_y^M + [\varepsilon_1^{(4)} - \nu_{21}\varepsilon_2^{(4)} - \nu_{31}\varepsilon_3^{(4)}] \\ &= (-\nu_{21}\frac{\sigma_x^M}{E_{22}} + \frac{\sigma_y^M}{E_{11}}) + \Delta T \cdot (\alpha_{11} - \nu_{21}\alpha_{22} - \nu_{31}\alpha_{33})\end{aligned} \tag{6-4}$$

The thermo-cycling effect is thought to be a relaxation behavior, because the plies are bonded together and cause thermal stresses without significant thermal strain. Mechanical in-plane strain provided by bending is also assumed to be constant once loaded during thermo-cycling provided that there is no significant in-plane extension during the thermo-cycling and the specimens are fully constrained in the longitudinal direction enough not to move in the in-plane direction.

A specimen's strain, ε^{Total} is held constant while stress is recorded in a relaxation test. The constitutive relation for the period of constant strain in the relaxation test is written as shown in (6-5).

$$\sigma(t) = Y(t) \cdot \varepsilon^{Total} \tag{6-5}$$

where *Y(t)* is a relaxation function.

The relaxation function is typically modeled with a Prony series as shown in (6-6) when the material is assumed to be a general Maxwell solid.

$$Y(t) = E_0 \cdot (1 - \sum_{i=1}^{n} p_i \cdot (1 - e^{-\frac{t}{\tau_i}})) \tag{6-6}$$

where

p_i is the *i*'th Prony constant (*i=1,2,….*)

τ_i is the *i*'th Prony retardation time constant (*i=1,2,….*)

E_0 is the instantaneous modulus of the material.

The deformation history should be considered in order to determine the stress state in a viscoelastic material at a give time. A superposition of hereditary integrals describes the time dependent response for linear viscoelastic materials. The relaxation model to obtain the stress function is introduced by an arbitrary function

$$\sigma(t) = Y(t) \cdot \varepsilon_0 + \int_0^t Y(t - \xi) \cdot \frac{d\varepsilon(\xi)}{d\xi} d\xi \tag{6-7}$$

where $\frac{d\varepsilon(\xi)}{d\xi}$ is the strain rate.

Chen implemented the Hereditary integrals with Prony series for a viscoelastic loading process by using divided segments for strain and strain rate functions [90]. Similar segment-dividing can be applied in the current study to simulate stresses corresponding to strain and strain rate functions varying with time and temperature.

$$\varepsilon(t)=\begin{cases}\varepsilon_1\cdot\dfrac{t}{t_1-t_0} & : \quad t_0<t\le t_1 \quad : \quad T(t)=T(t_0)+\dfrac{T(t_1)-T(t_0)}{t_1-t_0}\cdot t\\ \varepsilon_2 & : \quad t_1<t\le t_2 \quad : \quad T(t)=T(t_1)\\ \varepsilon_3\cdot\dfrac{t}{t_3-t_2} & : \quad t_2<t\le t_3 \quad : \quad T(t)=T(t_2)+\dfrac{T(t_3)-T(t_2)}{t_3-t_2}\cdot(t-t_2)\\ \varepsilon_4 & : \quad t_3<t\le t_4 \quad : \quad T(t)=T(t_3)\end{cases} \tag{6-8}$$

$$\frac{d\varepsilon}{dt}=\begin{cases}\dfrac{\varepsilon_1}{t_1-t_0} & : \quad t_0<t\le t_1 \quad : \quad T(t)=T(t_0)+\dfrac{T(t_1)-T(t_0)}{t_1-t_0}\cdot t\\ 0 & : \quad t_1<t\le t_2 \quad : \quad T(t)=T(t_1)\\ \dfrac{\varepsilon_3}{t_3-t_2} & : \quad t_2<t\le t_3 \quad : \quad T(t)=T(t_2)+\dfrac{T(t_3)-T(t_2)}{t_3-t_2}\cdot(t-t_2)\\ 0 & : \quad t_3<t\le t_4 \quad : \quad T(t)=T(t_3)\end{cases} \tag{6-9}$$

where

ε_1 *and* $\varepsilon_3=\varepsilon^M-[T(t)-T_{ref}]\cdot\overline{\alpha}$

$\varepsilon_2=\varepsilon^M-[T(t_1)-T_{ref}]\cdot\overline{\alpha}$

$\varepsilon_4=\varepsilon^M-[T(t_3)-T_{ref}]\cdot\overline{\alpha}$

ε^M is the in-plane strain due to bending.

Temperature, T is a function of time.

$\overline{\alpha}$ is the equivalent thermal expansion coefficient in a specific direction considering poisson's ratio.

Stress functions for each step can be derived from the strain and strain rate functions.

Step 1. ($t_0 < t \le t_1$)

$$\begin{aligned}\sigma(t) &= \varepsilon_0 \cdot Y(t) + \int_0^t Y(t-\xi)\frac{d\varepsilon(\xi)}{d\xi}d\xi \\ &= \varepsilon_0 \cdot Y(t) + \int_0^t E_0 \cdot (1 - \sum_{i=1}^{n} p_i \cdot (1 - e^{-\frac{(t-\xi)}{\tau_i}})) \cdot \frac{\varepsilon_1}{t_1 - t_0} d\xi\end{aligned} \tag{6-10}$$

Step 2. ($t_1 < t \le t_2$)

$$\begin{aligned}\sigma(t) &= \varepsilon_0 \cdot Y(t) + \int_0^{t_1} Y(t-\xi)\frac{d\varepsilon(\xi)}{d\xi}d\xi + \int_{t_1}^t Y(t-\xi)\frac{d\varepsilon(\xi)}{d\xi}d\xi \\ &= \varepsilon_0 \cdot Y(t) + \int_0^{t_1} E_0 \cdot (1 - \sum_{i=1}^{n} p_i \cdot (1 - e^{-\frac{(t-\xi)}{\tau_i}})) \cdot \frac{\varepsilon_1}{t_1 - t_0} d\xi + 0\end{aligned} \tag{6-11}$$

Step 3. ($t_2 < t \le t_3$)

$$\begin{aligned}\sigma(t) &= \varepsilon_0 \cdot Y(t) + \int_0^{t_1} Y(t-\xi)\frac{d\varepsilon(\xi)}{d\xi}d\xi + \int_{t_1}^{t_2} Y(t-\xi)\frac{d\varepsilon(\xi)}{d\xi}d\xi + \int_{t_2}^t Y(t-\xi)\frac{d\varepsilon(\xi)}{d\xi}d\xi \\ &= \varepsilon_0 \cdot Y(t) + \int_0^{t_1} E_0 \cdot (1 - \sum_{i=1}^{n} p_i \cdot (1 - e^{-\frac{(t-\xi)}{\tau_i}})) \cdot \frac{\varepsilon_1}{t_1 - t_0} d\xi + 0 \\ &\quad + \int_{t_2}^t E_0 \cdot (1 - \sum_{i=1}^{n} p_i \cdot (1 - e^{-\frac{(t-\xi)}{\tau_i}})) \cdot \frac{\varepsilon_3}{t_3 - t_2} d\xi\end{aligned} \tag{6-12}$$

Step 4. ($t_3 < t \le t_4$)

$$\begin{aligned}\sigma(t) &= \varepsilon_0 \cdot Y(t) + \int_0^{t_1} Y(t-\xi)\frac{d\varepsilon(\xi)}{d\xi}d\xi + \int_{t_1}^{t_2} Y(t-\xi)\frac{d\varepsilon(\xi)}{d\xi}d\xi + \int_{t_2}^{t_3} Y(t-\xi)\frac{d\varepsilon(\xi)}{d\xi}d\xi \\ &\quad + \int_{t_3}^{t} Y(t-\xi)\frac{d\varepsilon(\xi)}{d\xi}d\xi \\ &= \varepsilon_0 \cdot Y(t) + \int_0^{t_1} E_0 \cdot (1 - \sum_{i=1}^{n} p_i \cdot (1 - e^{-\frac{(t-\xi)}{\tau_i}})) \cdot \frac{\varepsilon_1}{t_1 - t_0}d\xi + 0 \\ &\quad + \int_{t_2}^{t_3} E_0 \cdot (1 - \sum_{i=1}^{n} p_i \cdot (1 - e^{-\frac{(t-\xi)}{\tau_i}})) \cdot \frac{\varepsilon_3}{t_3 - t_2}d\xi + 0\end{aligned} \tag{6-13}$$

More thermo-cycles were applied to the viscoelastic model and the stress levels corresponding to time and thermo-cycles were investigated.

The overall stress computation algorithm is as follows (Figure 6.3).

for (number of thermo-cycles, N=1 to 8)
for (t=0 to 700 minutes)

$T(t)$

$\varepsilon(t) = \varepsilon^M(t) + \varepsilon^T(t)$

$\frac{d\varepsilon}{dt} = \frac{d\varepsilon^T}{dt}, \quad \frac{d\varepsilon^M}{dt} \approx 0$

$\sigma(t) = \varepsilon_0 \cdot Y(t) + \int_0^t Y(t-\xi)\frac{d\varepsilon(\xi)}{d\xi}d\xi$

Check micro-cracking with a failure criterion $\sigma_{new}^{UT} = \sigma^{UT}(T)$

end

$M_{new} = M(\rho) \quad \alpha_{new} = \alpha(T) \quad \sigma_{new}^{UT} = \sigma^{UT}(\rho) \quad \nu_{new} = \nu(T)$

end

Figure 6.3. *Stress computation algorithm using visco-elastic properties*

Based on the algorithm, in-plane stresses in ply 4 as a function of time, temperature, and thermo-cycles, were calculated using Matlab 7.

6.3 Initial Damage Characterization

Figure 6.4 shows the transverse strain and stress profiles of the top layer (layer 4) as a function of time and temperature under initial cryogenic cycling with heating at a rate of 4^{o}C/min temperature from cryogenic to room temperature. Figure 6.5 shows strain in the fiber direction (longitudinal) and stress profiles in layer 4 under the same cryogenic cycling condition as Figure 6.4.

Transverse strain and stress are tensile as can be seen in Figure 6.4. 130, 115, and 82 MPa of large thermal residual stresses associated with mechanical in-plane stresses of three different bending loads at -196^{o}C were obtained from the Figure 6.4. The strain amplitude of the tension-tension thermal fatigue (cycling) in the transverse direction was 0.45. The stress amplitude was 47 MPa. Longitudinal strain and stress are compressive as shown in Figure 6.5. The strain amplitude of the compression-compression thermal fatigue (cycling) was 0.032.

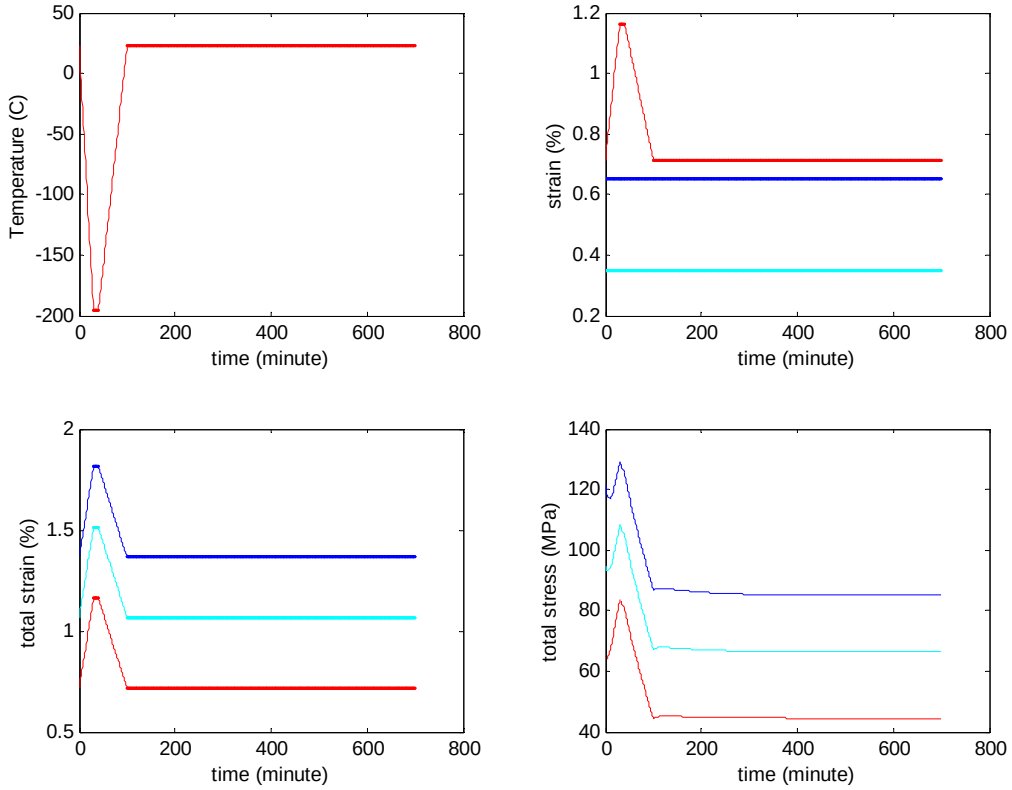

Figure 6.4. *Transverse strain and stress profiles of the top layer as a function of time and temperature under the first cycle of -196 to 23°C with 4°C/min thermo-cycling*

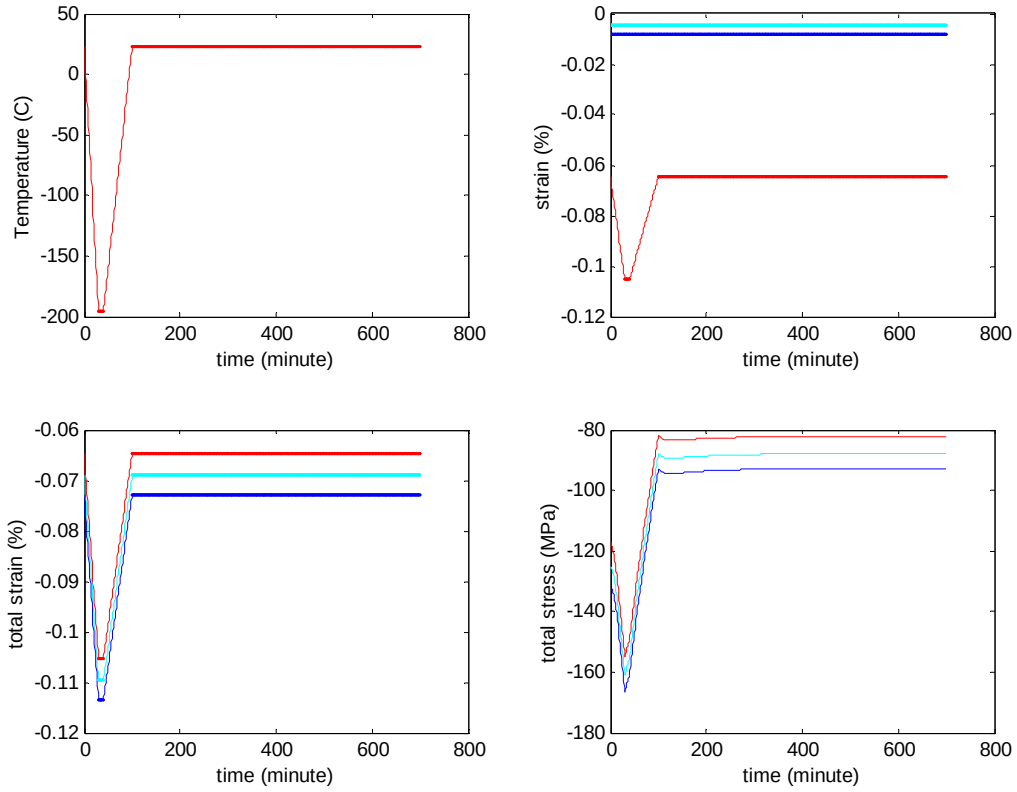

Figure 6.5. *Fiber directional strain and stress profiles of the top layer as a function of time and temperature under the first cycle of -196 to 23°C with 4°C/min thermo-cycling*

Based on the stress level on ply 4, a failure criterion is applied to investigate the initial damage condition. One of the typical layer failure criteria is *the quadratic interaction criterion*. It is similar to the *Tsai-Wu failure criteria* and used on each of the plies in the laminate to determine failure at a lamina level [91]. The quadratic interaction criterion is:

$$R^2(F_{xx}\sigma_x^2 + 2F_{xy}\sigma_x\sigma_y + F_{yy}\sigma_y^2) + R(F_x\sigma_x + F_y\sigma_y) - 1 = 0 \tag{6.14}$$

where

$$F_{xx} = \frac{1}{XX_c} \tag{6.15}$$

$$F_{yy} = \frac{1}{YY_c} \tag{6.16}$$

$$F_x = \frac{1}{X} - \frac{1}{X_c} \tag{6.17}$$

$$F_y = \frac{1}{Y} - \frac{1}{Y_c} \tag{6.18}$$

$$F_{xy} = -\frac{1}{2}\sqrt{F_{xx}F_{yy}} \tag{6.19}$$

X is the tensile strength in the fiber direction.

X_c is the compressive strength in the fiber direction.

Y is the tensile strength transverse to the fibers.

Y_c is the compressive strength transverse to the fibers.

σ_x is the stress in the fiber direction.

σ_y is the stress transverse to the fibers.

Solving for R, which is the only unknown in the equation, gives

$$R = \frac{-H \pm \sqrt{H^2 + 4G}}{2G} \tag{6-20}$$

where

$$G = F_{xx}\sigma_x^2 + 2F_{xy}\sigma_x\sigma_y + F_{yy}\sigma_y^2 \tag{6-21}$$

$$H = F_x\sigma_x + F_y\sigma_y \tag{6-22}$$

The physical meaning of the R is

$$R = \frac{\sigma_{ultimate}}{\sigma_{applied}} \tag{6-23}$$

and the positive R is taken from equation 6-(20). The quadratic interaction criterion states that if R>1, then applied stress components are below failure level. If R<1, the lamina may fail. However, in this study, due to the lack of information on transverse failure strength of composite, we cannot say that failure will occur at R<1. We can only say that lower R implies a higher chance of crack formation. By looking at the stress components on ply 4, which is of interest in this study, R values are derived for each loading condition. Figure 6.6 shows that the R value expected at 23^{o}C, -196^{o}C, 250^{o}C, and 250^{o}C considering transverse modulus and strength reduction, under three different in-plane strains due to bending, based on residual thermal stress analysis. Experimental results show that initial cracking occurs under 0.325 ~0.650% mechanical in-plane strain at 23^{o}C. Therefore, the corresponding R value, 0.5231 is considered to be the critical value to decide whether crack initiation occurs.

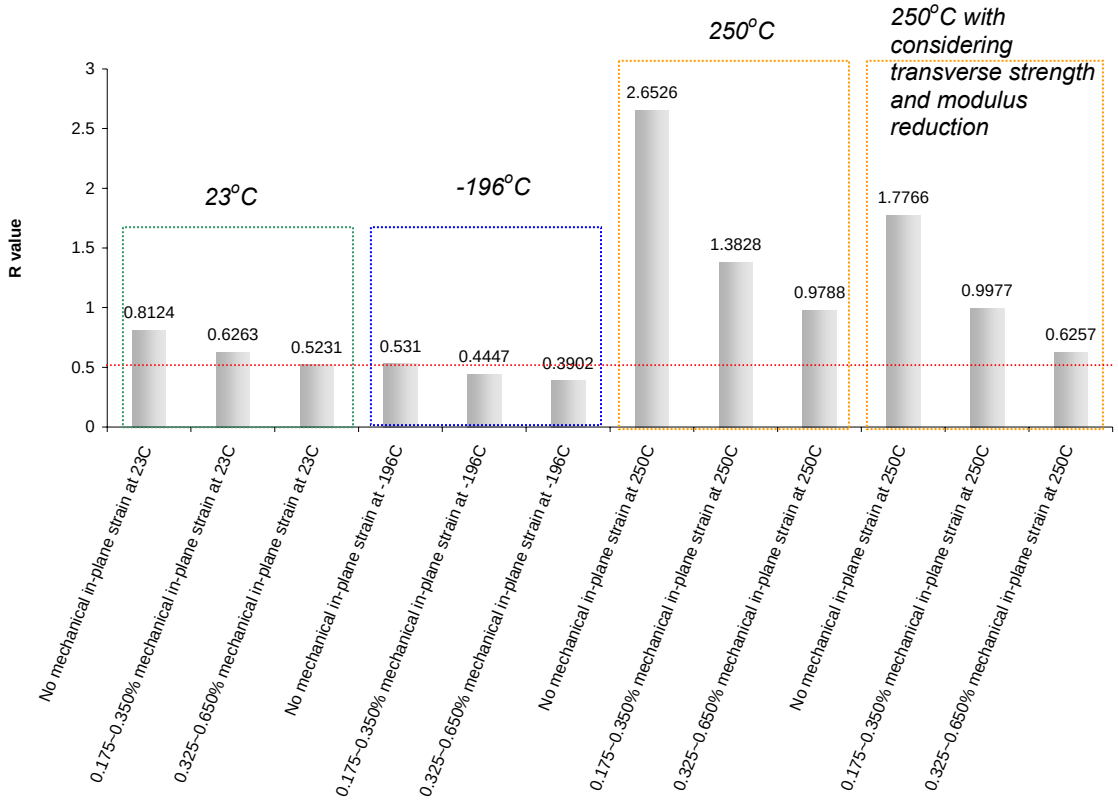

Figure 6.6. *R value of ply 4 based on the quadratic interaction failure criteria corresponding mechanical strains, cryogenic & high temperature induced thermal stress, and mechanical-thermal combined effects*

Microcracking was induced in specimens exposed to -196°C at all stress levels. *R* value (0.5310) under no mechanical strain at -196°C is higher than that (0.5231) under 0.175~0.350% in-plane strain at 23°C, which means the expected crack density under 0.175~0.350% in-plane strain at 23°C is higher than under no strain at -196°C. But experimental results showed opposite. The reason can be explained by the difference in strain energy release rates at different temperatures. Lower strain energy release rate showed easier cracking even under lower strain levels (Figure 6.7).

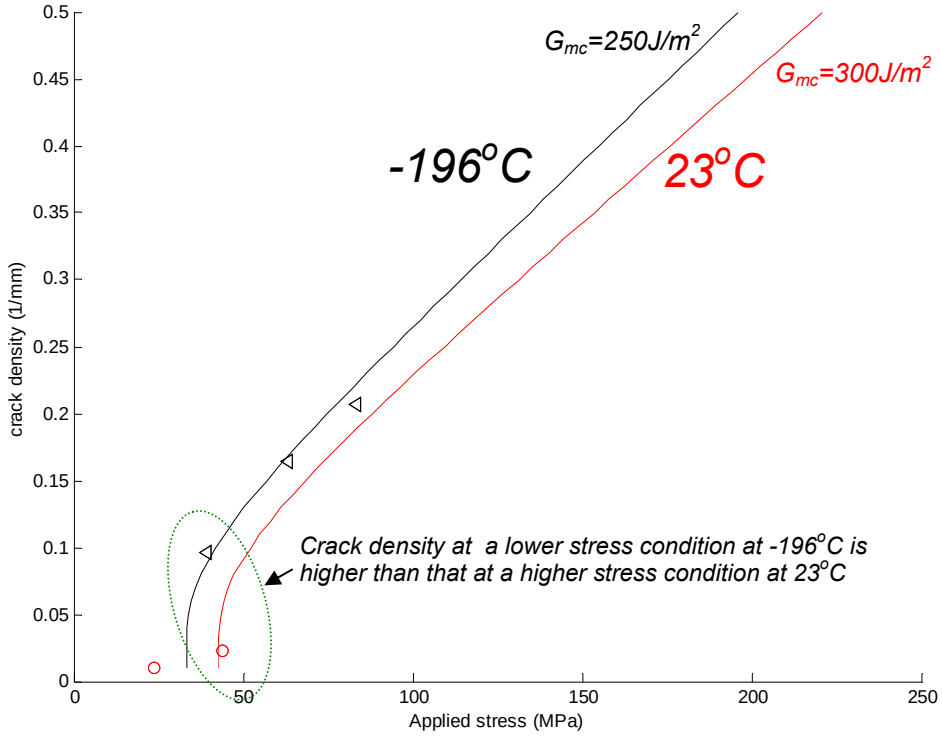

Figure 6.7. *Crack densities at 23 and -196°C as a function of stress*

6.3.1 Cryogenic Temperature Cycling

Cooling to -196°C is known to be an important factor in giving rise to large thermal stresses resulting in micro-cracking. Moreover, composites, post-cured at high temperatures such as 371°C, experience more severe thermal stress conditions in both matrix and fiber/matrix interface when the composites are exposed to cryogenic temperatures. Interfacial debonding seems to be a failure mode at cryogenic temperature

when samples were observed with optical microscopy (Figure 6.8), which gives rise to the conclusion that strength of interface is lower than that of matrix or that the local stress level on the interface is higher than on the matrix. However, an explicit explanation of the interfacial debonding is difficult because the interface (M40J between PMR-II-50) strength is unknown and very hard to measure even using a nano-indenter.

In addition to the cure induced extreme thermal residual stresses associated with cryogenic temperatures, cool-down degradation might occur, mainly caused by the fact that thermal stresses cannot relax sufficiently in highly cross-linked matrix systems [92-96]. The thermal stresses also pre-load the matrix at low temperature and lower the available fracture strain, resulting in a decrease of strength.

The large residual thermal stress at the cryogenic temperature has been known well for the high temperature cured thermoset composite. M40J/PMR-II-50 has 370^{o}C cure temperature, which means the composite is very high temperature cured one. Therefore, initial cryogenic temperature exposure of M40J/PMR-II-50 showed microcrack initiation.

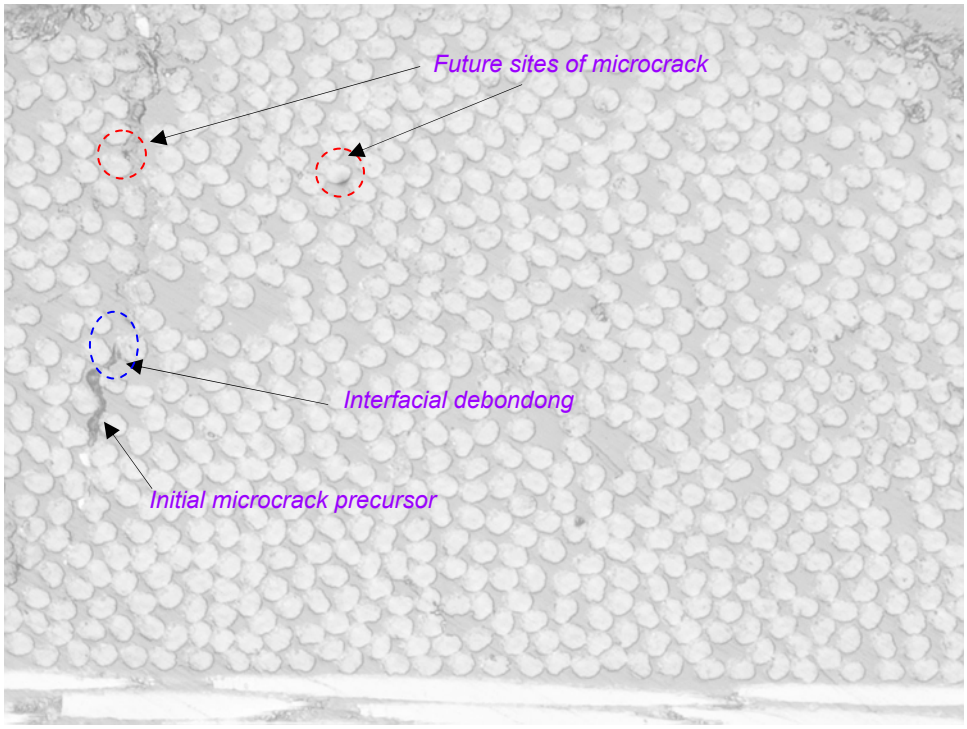

Figure 6.8. *Photo of composite failure in specimen exposed to -196°C (1 cycle)*

6.3.2. High Temperature Cycling

High temperature thermo-cycling itself does not appear to be a factor causing micro-cracking by the thermo-mechanical model based on thermal residual stress components assuming that stress free temperature is 371°C which is the last post-cure temperature. But, microcrack initiation was observed at the fiber/matrix interface as shown in Figure 6.9.

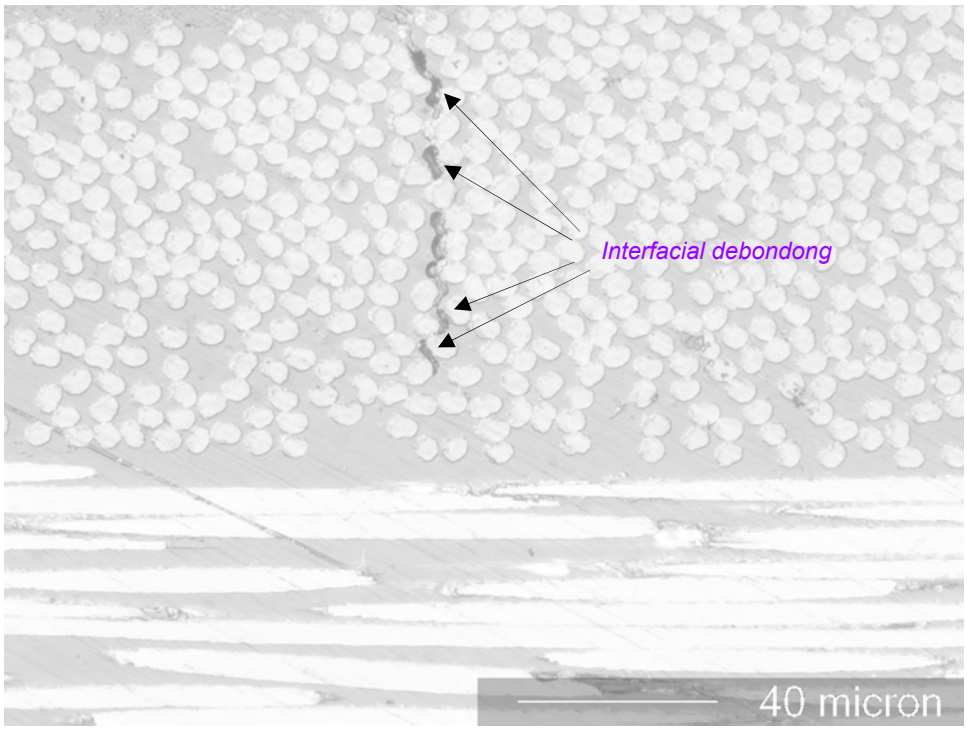

Figure 6.9. *Photo of composite failure exposed to 250°C (1 cycle)*

Temperature dependent strength should be considered for failure criterion at high temperatures. Normally, polymers tested at high temperatures shows a lower threshold of strength value for damage initiation. PMR-II-50 matrix at high temperature shows strength and modulus reductions as shown in Figures 6.9 and 6.10. Therefore, matrix dominated transverse strength value, Y and Y_c in equation 6-(16) and 6-(18) should be changed to 42.28 and 10.57 MPa, respectively, and the quadratic interaction failure criterion calculation was repeated with the changed values. The repeated calculation of the quadratic interaction failure criterion, however, still shows that there is no chance of lamina failure at high temperature based on the thermal residual stress as can be seen Figure 6.6.

0.1% specimen weight loss after one thermo-cycle from 23 to 250^{o}C dose not seem to be enough to explain the high temperature damage associated with the resin's thermal degradation on high temperature exposure.

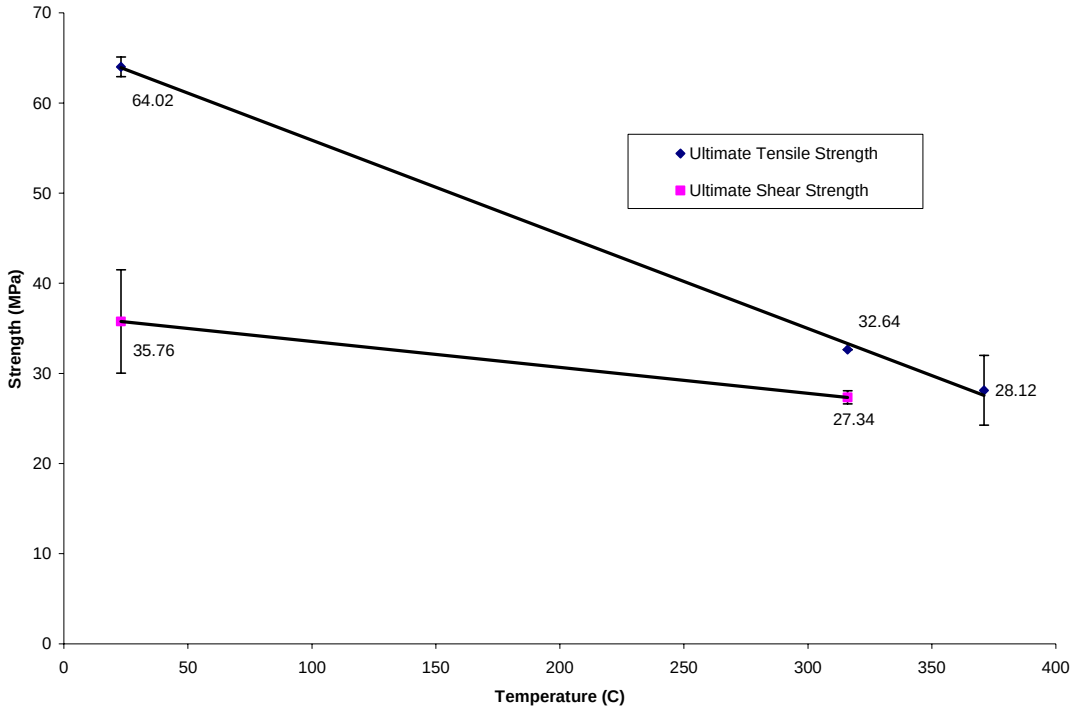

Figure 6.10. *Strength change of PMR-II-50 with temperature varying*

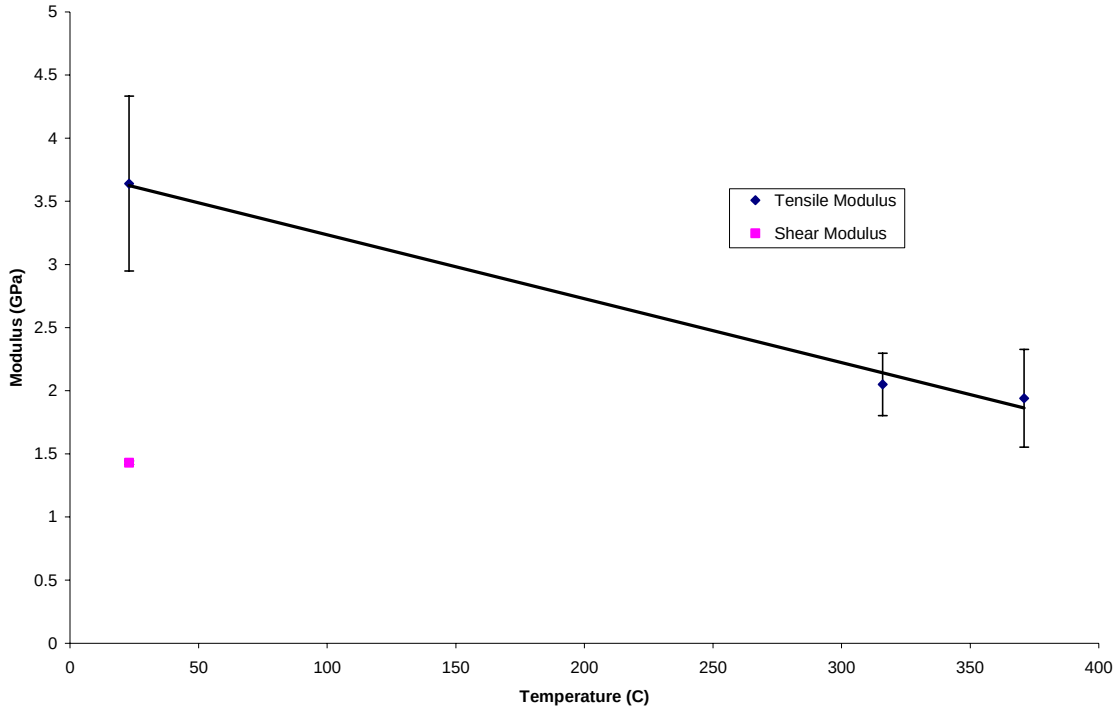

Figure 6.11. *Modulus change of PMR-II-50 with temperature varying*

There are several possible failure modes of composites at high temperature. A possible strength reduction at the interphase (fiber/matrix interface zone) gives rise to the weakness of the bonding, resulting in interface failure at the high temperatures. VanLandingham *et al*. showed an interphase strength reduction at elevated temperature (200^{o}C) using nano indentation test and finite element analysis [97,98]. They also showed a strength gradient over the interphase with increasing temperature.

An epoxy compatible sizing between PMR-II-50 and M40J could be a reason for interfacial failure at high temperatures. High local thermal stresses at the interface due to

the rough fiber surface due to sizing effect may be possible. The sizing material itself could be degraded at the high temperatures, resulting in weakness in interfacial adhesion

6.3.3 Cryogenic and High Temperature Combined Cycling

The cycle profile obtained by adding high temperature (250^{o}C) to the cryogenic exposure increases the crack density maintaining interfacial failure (Figure 6.12). The crack density increase cannot be explained in terms of thermo-elasticity which is focused on thermal residual stress. Bechel *et al.* [26] tried to explain the phenomena . They showed that room temperature mechanical fatigue testing of a carbon/epoxy composite produced interesting results. When a peak cyclic constant tensile loading was applied while varying minimum stress, laminate failure occurred only after a few cycles [26]. The analogy between mechanical fatigue and thermal cycling seems probable but still cannot explain the damage under the room temperature to 250^{o}C cycle profile.

Henaff-Gardin *et al.* theoretically and experimentally showed the significance of high temperature amplitude to strain energy release rate ($\boldsymbol{G_I}$) by showing different $\boldsymbol{G_I}$ levels of carbon/epoxy composites under thermo-cycling of i)-200 to 20^{o}C, ii)-200 to 50^{o}C, iii) -200 to 90^{o}C, and iv) -200 to 130^{o}C [45]. They proved that a lower strain energy release rate would provide a slower damage evolution. For example, no damage evolution in an epoxy composite was observed under the -200 to 20^{o}C thermo-cycling until 30 cycles, which means that $\boldsymbol{G_I}$ value is always lower than $\boldsymbol{G_{IC}}$ value even with increasing number of thermo-cycles. However, the -200 to 130^{o}C thermo-cycling showed crack saturation at an early stage of thermo-cycling, because its initial $\boldsymbol{G_I}$ value is higher than $\boldsymbol{G_{IC}}$ value.

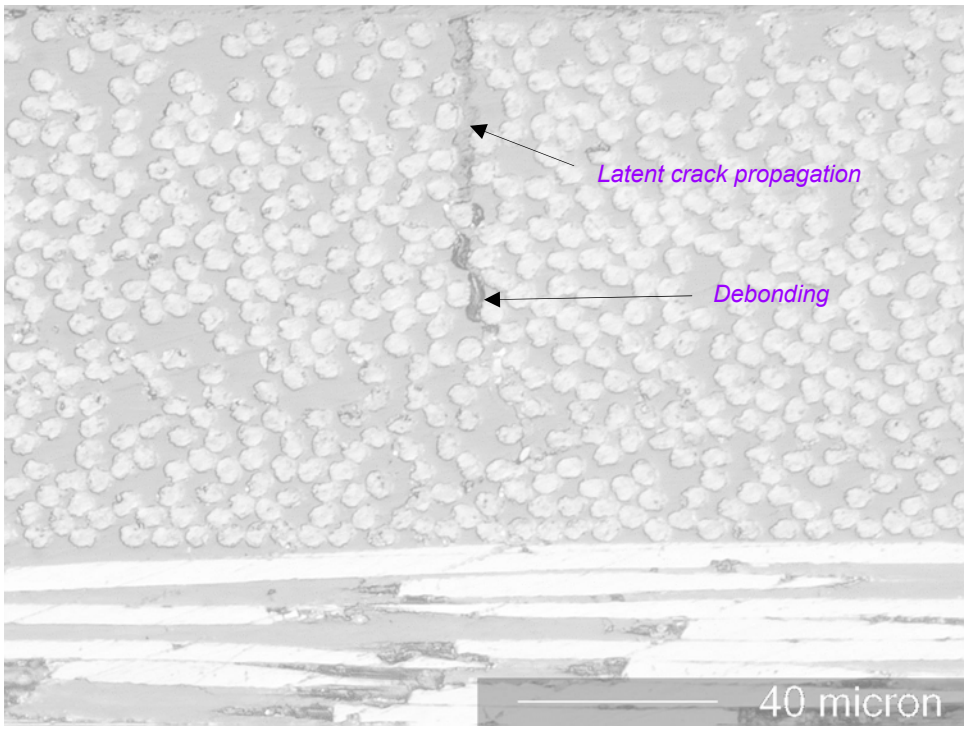

Figure 6.12. *Photo of composite failure exposed to 23 to -196 to 250°C (1 cycle)*

Cryogenic temperature (-196°C) exposure after elevated temperature (250°C) showed about 26% increase in crack density compared to the high temperature exposure subsequent to -196°C as shown in Figure 6.13. Microcracks initiated by interfacial debonding at 250°C connected together at -196°C under brittle matrix conditions (Figure 14).

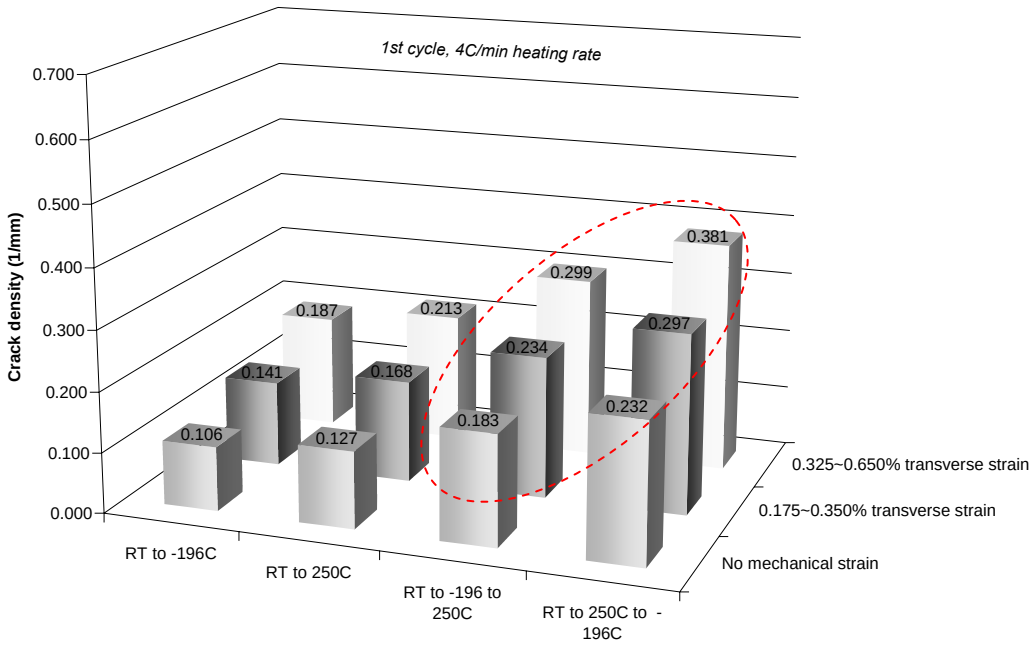

Figure 6.13. *Crack densities with four different thermo-cycling temperature profiles and three different transverse mechanical strains (1 cycle)*

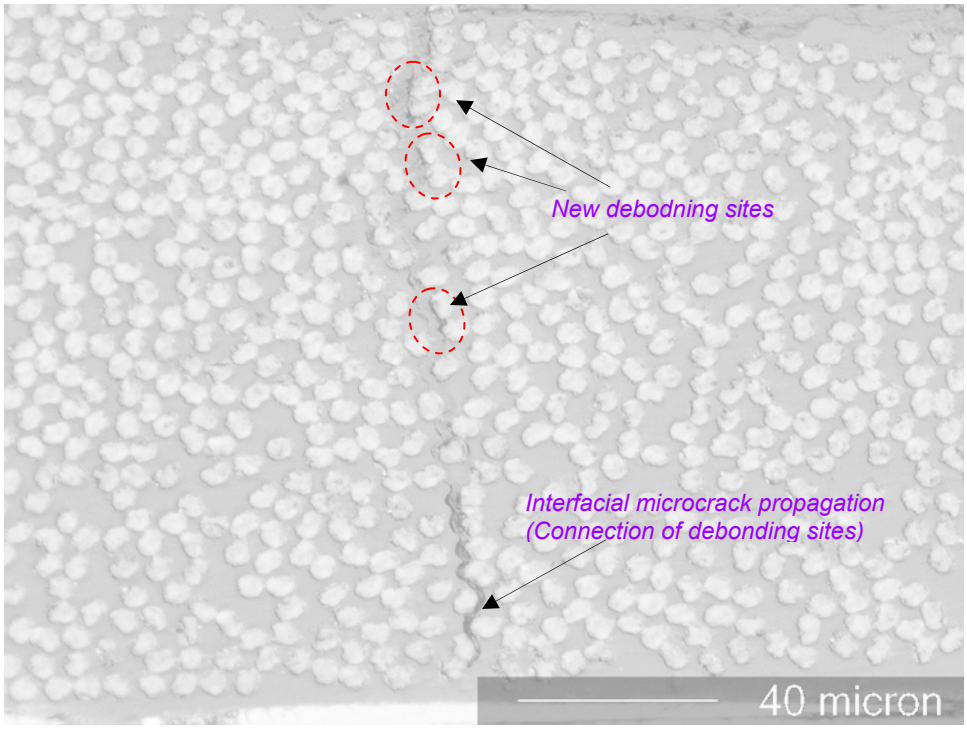

Figure 6.14. *Photo of composite failure exposed to 23 to 250 to -196°C (1 cycle)*

6.4 Damage Characterization with Increasing Number of Thermo-Cycles

Thermal fatigue failure is the result from some form of mechanical constraint and temperature cycling. Thermal expansion or contraction induced by a temperature change acting against a constraint causes thermal stress.

Thermo-cycling induced crack density models are scarcely found in literature. The fact that there is little experimental data is the reason for the lack of thermo-cycling models. Difficulties in expressing the change in mechanical and thermal properties based on different thermal history is the other reason for lack of models. Most models only express temperature dependent stress and strain profiles under one cycling condition. The high thermal stress difference between 130MPa at -196^{o}C and 70MPa at 250^{o}C is thought to be a main mode to induce damage. Damage under the cryogenic to room temperature cycling is related to experience of high transverse stress conditions. The thermal cycling effect at high temperatures is related to interphase strength reduction. Combined cryogenic and high temperature cycling is the most severe condition causing highest crack densities. When crack which initiated at high temperatures are later subjected to cryogenic temperatures, the cracks propagate through the brittle matrix.

Hashin and Nairn proposed a model to account for stiffness reduction in [0/90]s and [90/0]s lay-ups related to crack density [99,100]. The model was set up based on a stress perturbation function and has been proved to be in good agreement with experimental results. The stiffness reduction model is applied to the present material, M40J/PMR-II-50 and the modulus reduction is plotted as a function of crack density as shown in Figure 6.15. The stiffness reduction of M40J/PMR-II-50 (4.5% at saturation level) by using its

mechanical properties is not as severe compared to the E-glass/epoxy (30 to 40% at saturation level) as shown in Figure 6.16.

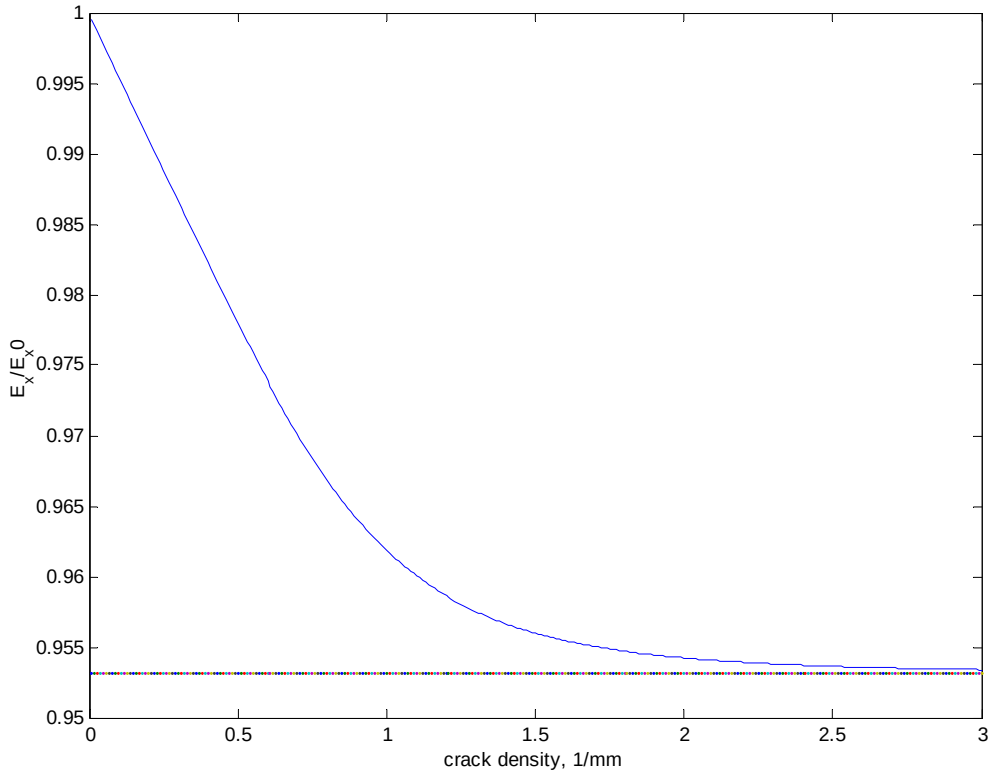

Figure 6.15. *M40J/PMR-II-50 stiffness reduction as a function of crack density using Hashin's stress perturbation theory [99]*

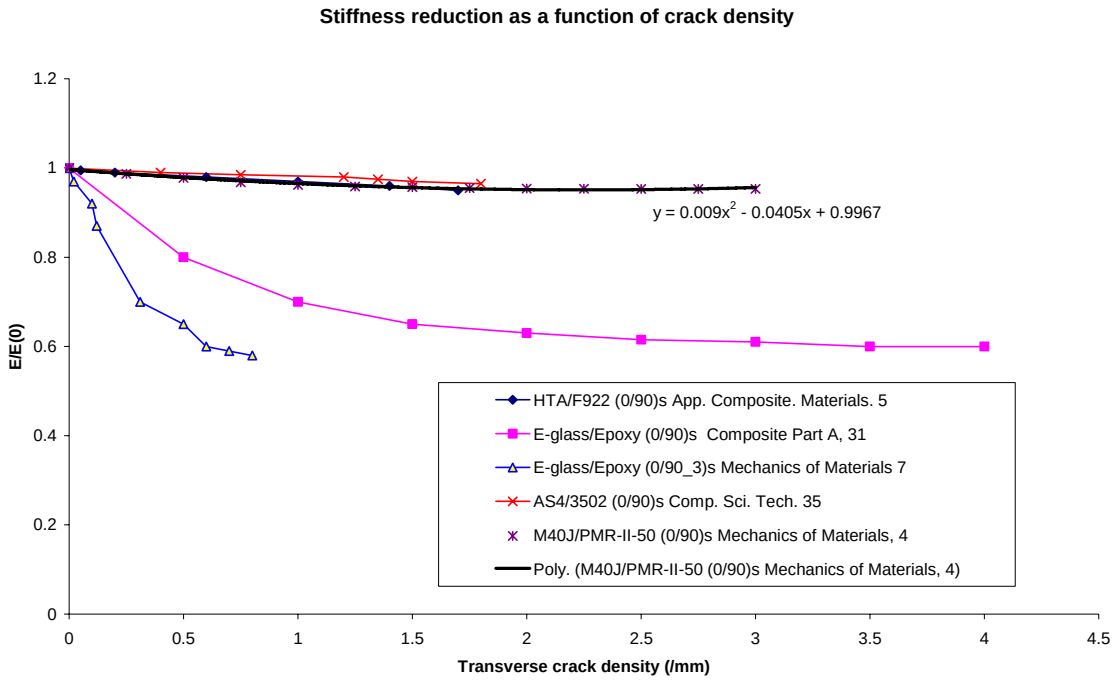

Figure 6.16. *Various modulus reductions of composite materials as a function of crack density*

6.4.1 Low Temperature Cycling with Increasing Number of Cycles

High thermal residual stress was known to be the main damage mechanism under cryogenic temperature exposure. The cycling effect associated with easy crack propagation in brittle matrix conditions enhances the damage at cryogenic temperatures with increasing number of thermo-cycles as can be seen in Figure 5.8. Crack density increase after 8 cycles was observed from 0.159 to 0.233 mm^{-1}.

Cycling effect at -196°C can be evaluated using Nairn's critical strain energy release rate based damage mechanics. Based on the theory, 8 cycles of cryogenic cycling is equivalent to 60 to 70 MPa of applied stress as shown in Figure 6.17.

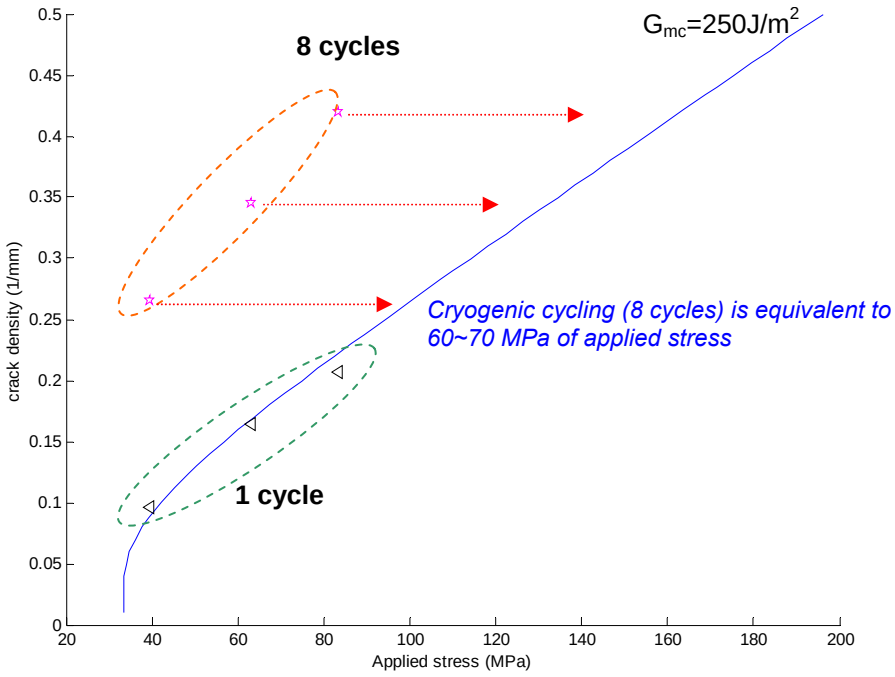

Figure 6.17. *Cryogenic cycling effect on crack density based on Nairn's critical strain energy release rate theory*

Microscophy shows that cracks propagated easily through thickness by linkage of debonding sites associated with the low critical strain energy release rate (Figure 6.18).

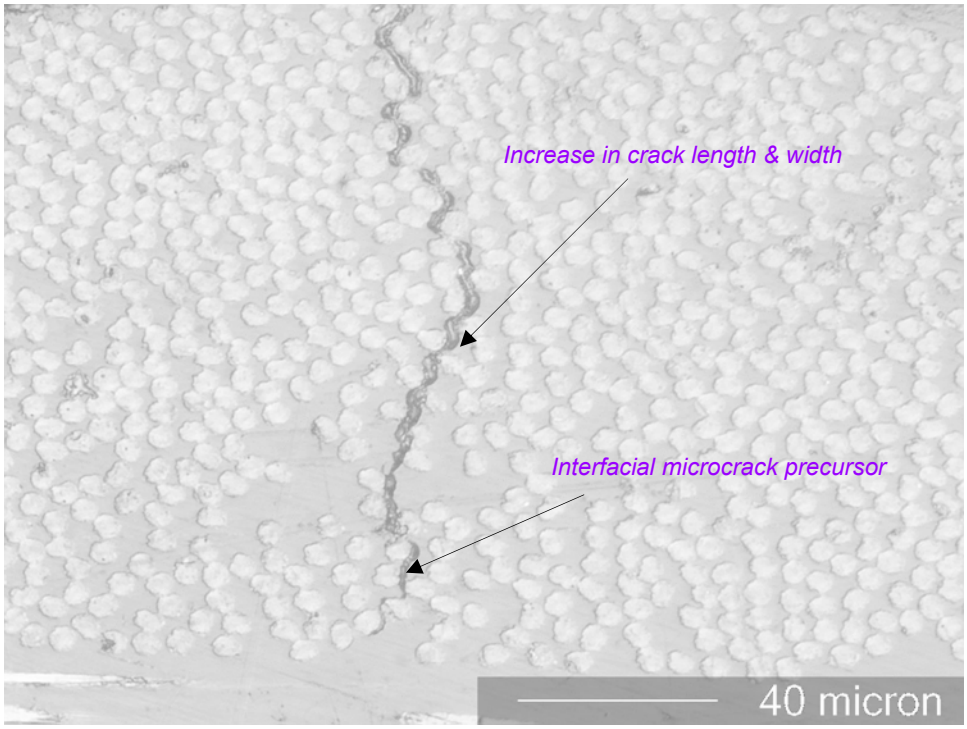

Figure 6.18. *Photo of composite failure exposed to 23 to -196°C (8 cycles)*

6.4.2 High Temperature Cycling with Increasing Number of Cycles

As mentioned earlier, modulus and strength decrease with increasing temperature without any chemical aging. 0.4% weight reduction observed after 8 thermo-cycles with 10 minutes of 250°C exposure (Figure 6.19) does not seem to significantly affect the thermal degradation of resin associated with the chain breaking. Instead, easy mobility of chain molecules at high temperature might cause loss in bonding strength between fiber and matrix resulting in debonding at fiber/matrix interfaces [101-103].

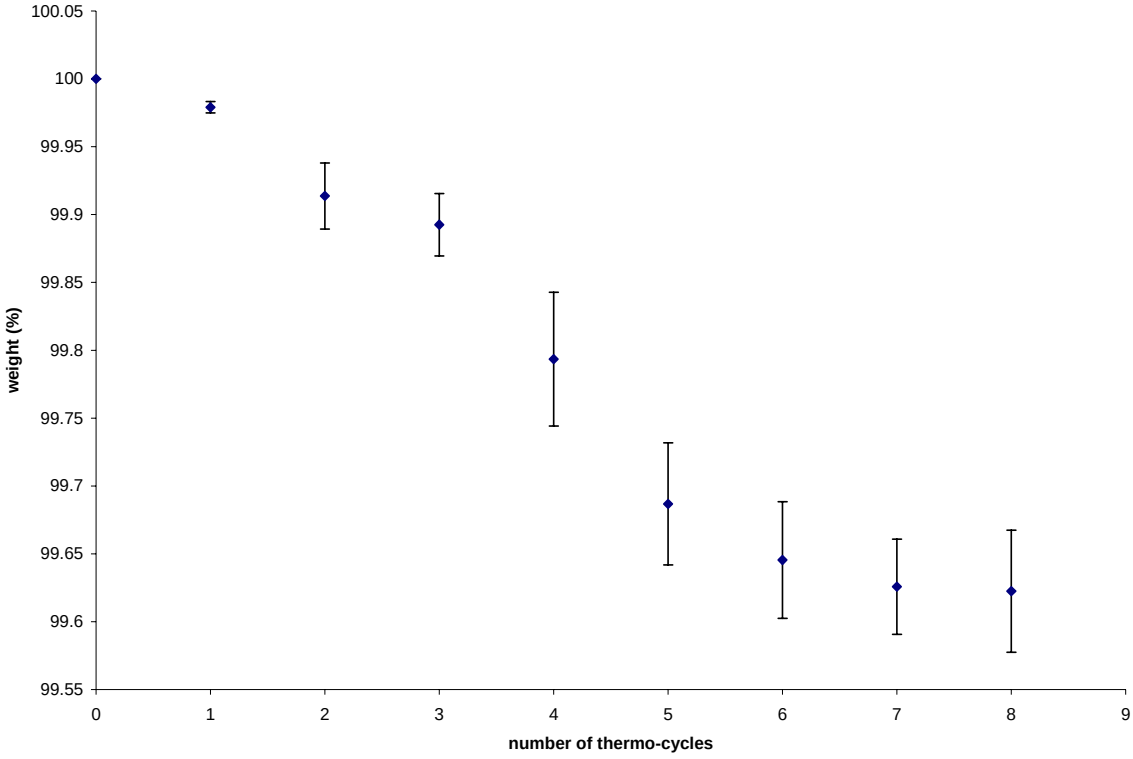

Figure 6.19. *Weight loss under high temperature thermo-cycling (23 to 250°C) with increasing number of thermo-cycles*

Crack density increases with increasing number of high temperature induced thermo-cycles as shown in Figure 5.9. Increase from 0.096 to 0.139 mm^{-1} crack density due to cycling effect was shown. Initial debonding related cracks hardly propagate in the thickness direction. This is because of the matrix ductility at high temperature as can be seen from Figure 6.20.

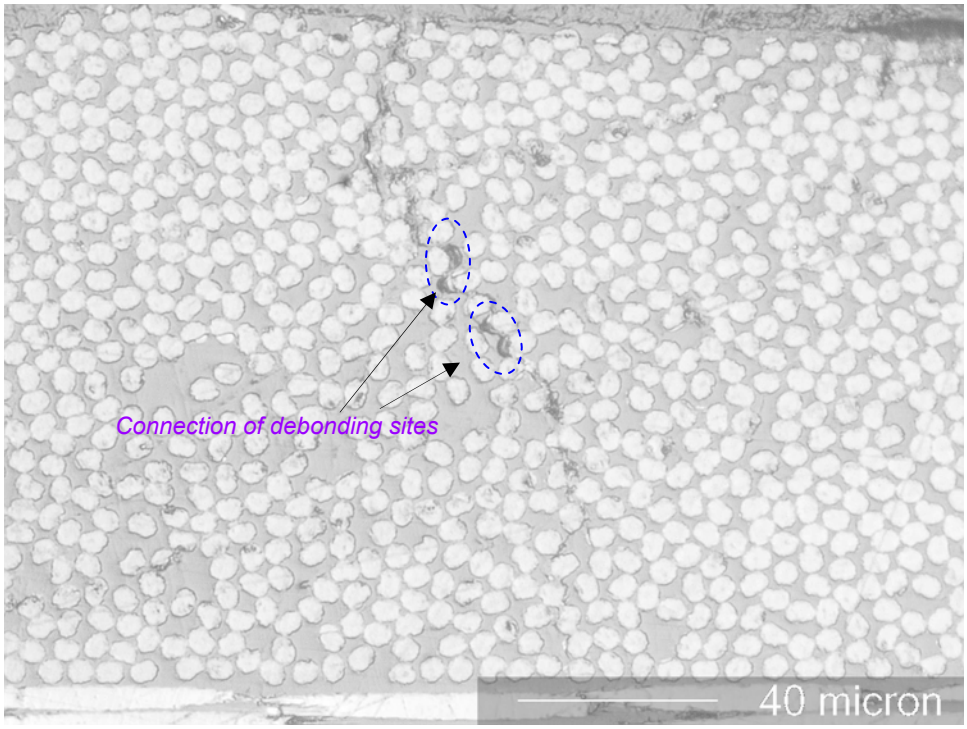

Figure 6.20. *Photo of composite failure exposed to 23 to 250°C (8 cycles)*

6.4.3 Cryogenic and High Temperature Combined Cycling with Increasing Number of Cycles

The combined cycling effect increase damage with increasing number of cycles. Once cracks are initiated, high temperature induced interfacial debonding and cryogenic temperature induced thermal-residual stresses accelerate damage. Crack density increased from 0.301 to 0.387 mm^{-1} after 8 cycles of the combined thermo-cycling as shown in Figure 5.11. Cracks were fully developed in the thickness direction with increasing number of the combined thermo-cycles (Figure 6.21).

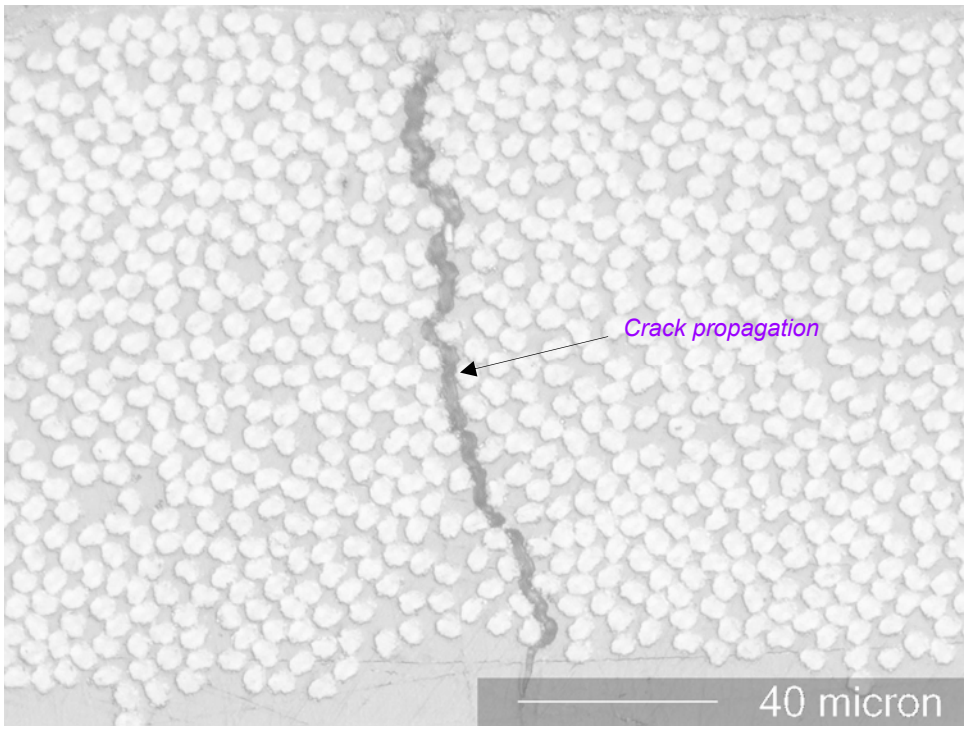

Figure 6.21. *Photo of composite failure exposed to 23 to -196 to 250°C (8 cycles)*

CHAPTER VII

NON- DESTRUCTIVE EVALUATION (NDE) OF COMPOSITES DAMAGE USING WATER ABSORPTION TEST

This chapter introduces an overview on Non-Destructive Evaluation (NDE) for polymer composite cracking and a possibility of the initially planned water absorption NDE for crack quantification during the mechanical loading combined thermo-cycling.

7.1 Overview on NDE for Polymer Composites Damage

Attempts to quantify damage of polymer composite materials have been made for decades in many ways such as manual crack number counting with surface images taken by optical microscopy, x-radiography, acoustic emission (AE) and diffusion of heat or moisture into the materials. Equipped with a good environmental exposure control for damage characterization and the development of approaches to characterize 3-D materials damage by image digitizing technique and computing ability, there still exist obstacles to overcome in order to generate exact 3D damage in terms of resolution and time to measure.

General methods used for damage quantification are i) manual crack counting with images of the damaged composite and ii) x-radiography as a nondestructive evaluation (NDE) (Figure 7.1). The manual crack counting is the method to count the number of

cracks at the edge surface of a specimen and estimate crack density by normally defining number of cracks divided by length of the specimen, which measures the average crack space through the edge surface. This method does not consider the crack opening area at the surface and crack discontinuity through the specimen width direction.

The x-radiography provide inside crack images which are taken from one direction. This method is easier and faster to count the number of cracks than the manual counting method but still does not provide the variation of crack thickness toward the x-ray direction. Moreover, overlap of crack images through the x-ray direction may cause errors with specimens having many stacks. This may make it hard to generate a 3D geometry having numerous damage locations, whose importance is easy to resolve at the ply level stress considering ply thickness, edge stress variations, and stress gradient due to temperature distributions through the thickness of the laminate.

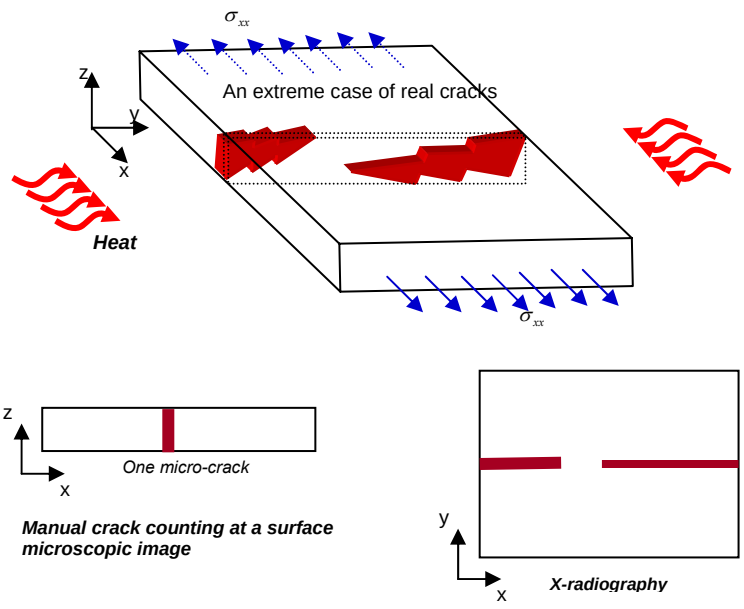

Figure 7.1. *Schematic of inside crack of composites and currently used crack quantification method*

7.2 Overview on Water Absorption NDE for Polymer Composites Damage

Water absorption NDE is based on the fact that water diffusion response varies depending on the damage status of a specimen. Up to now, many polymers and polymer composites' water (or moisture) absorption behavior have been studied. Using the classical diffusion theory [104], Shen and Springer developed a moisture diffusion model in polymer composites and showed that their experimental results are in a good accordance with the Fickian model [72]. After their work, numerous diffusion models of polymer and polymer composites have been developed. But there has been controversy concerning model assumptions. Some materials showed a good Fickian diffusion and others not. Some researchers claimed that the diffusion of polymer and polymer composites is two stage process; diffusion and relaxation controlled [105]. Researchers concluded that materials having a comparable viscoelastic relaxation showed Non-Fickian diffusion.

Anomalies of moisture absorption behavior of polymer composite materials exposed to cyclic moisture environment have been investigated. Wong and Broutman suggested that the increase of the free volume in the polymer network causes the anomalies [106]. Several case of anomalous moisture diffusion in viscoelastic material models have been presented by Wu and Pappas [107], Cai and Weitsman [108].

Fiber architecture was also suggested to be a factor modifying water diffusion kinetics by changing the residual stress state in a composite.

When polymer or polymer composites get irreversible damage such as cracks and delamination which significantly affect moisture uptake, the materials also do not show

the Fickian diffusion. Roy *et al.* [74,75], Weitsman [109] and Lundgren *et al.*[110] presented moisture diffusion models for cracked materials. Weitsman used continuum damage theories and thermodynamics to make the diffusion model, while Lundgren *et al.* used the micromechanical method. Irreversible thermodynamics was applied to the composite's macro-mechanics, which extended to the case of the model of both uni-axially and bi-axially damaged laminates by Roy *et al.* [74,75].

Considering the knowledge that internal damage such as microcracks inside composites may affect the change of diffusion while the composites are immersed in water, a water absorption based NDE is thought be an alternative to investigate the crack densities in composite specimens.

7.3 Application of Water Absorption NDE to the Current Experiment

The possibility of the application of the water absorption NDE to the current mechanical- loading combined thermal cycling experiment was pursued. The original plan for the whole experiment is shown in Figure 7.2. Water absorption based NDE to samples is performed before and after the combined mechanical loading and thermo-cycling test. Hygro-thermal effect was noticed when samples were immersed into 80^{o}C water for 24 hours followed by being dried at 80^{o}C in vacuum oven.

The interesting crack density of samples in this study is only in the upper 90^{o} layer as shown in Chapter IV, which means that immersing of sample and its measurement of water uptake cannot compare the crack density, the water absorption NDE is not thought to be integrated with the current study.

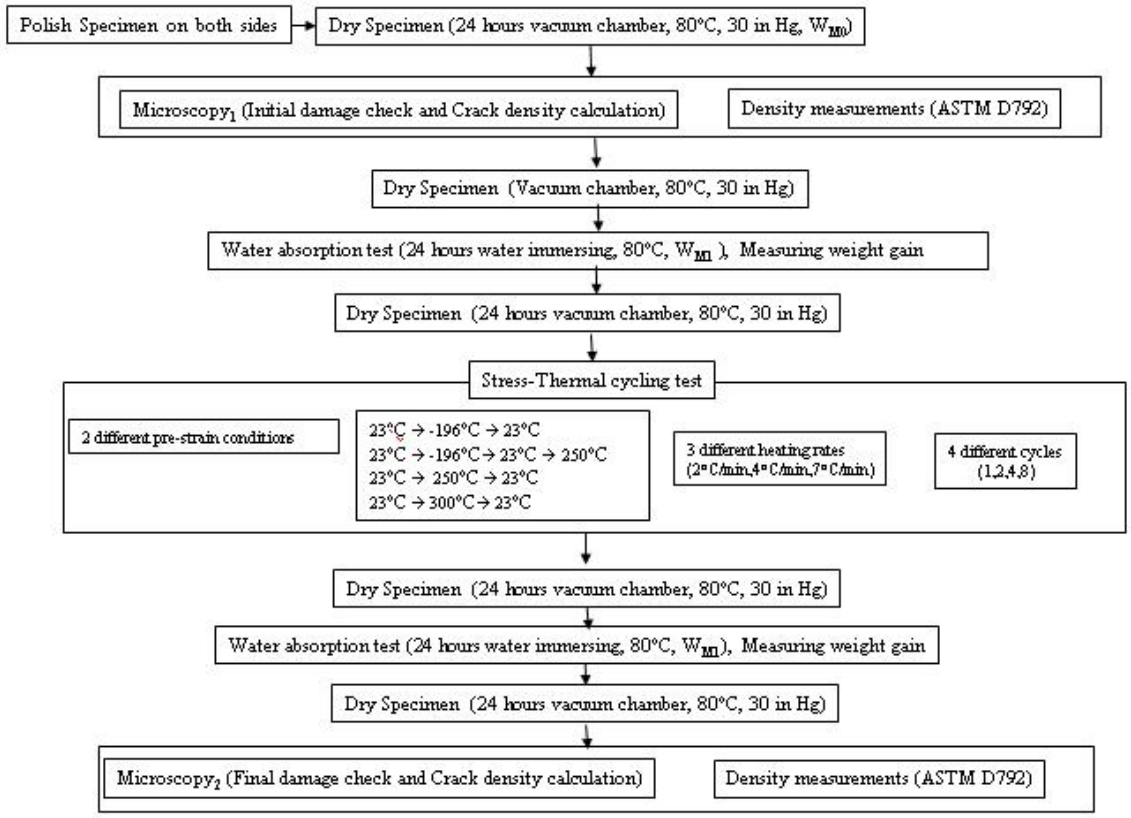

Figure 7.2. *Original plan of water absorption NDE before and after running the stress-thermal cycling experiment*

The goal of water absorption was to detect the amount of interconnected cracks from the surface into the interior of the composite.

7.4 Summary

Based on the investigations, following conclusions were made:

- A simple and cost effective water absorption Non-Destructive Evaluation (NDE) test for observing the levels of surface to interior interconnected micro-cracking of M40J/PMR-II-50, the high temperature polyimide composite, under stress-thermal cycling was studied.
- The hygro-thermal effect on M40J/PMR-II-50 after 24 hours of water immersion followed by drying in vacuum oven at 80^{o}C, again followed by thermo-cycling was serious in that existing cracks opened more.

CHAPTER VIII

SUMMARY AND CONCLUSIONS

8.1 Goals

The objective of this research was to determine the effect of thermal cycling combined with mechanical loading on the development of microcracks in carbon fiber/polyimide composites (M40J/PMR-II-50). Finding the critical controlling parameters for microcrack formation from mechanical stress-thermal cycling was done to meet the objective.

8.2 Experimental Approach

A novel conduction heating apparatus that combines thermal loading with large deflection bending is introduced, and its utilization was investigated in terms of the thermo-mechanical stress analysis

By clamping composite specimens (M40J/PMR-II-50, $[0,90]_s$, a uni-tape cross-ply) on the radial sides of half cylinders having two different radii (78.74mm and 37.96mm), three different in-plane strains (0%, 0.175~0.350%, and 0.325~0.650%) including a no strain condition were applied to the composites. Three different thermal loading experiments, 1) 23^{o}C to –196^{o}C to 250^{o}C, 2) 23^{o}C to 250^{o}C, and 3) 23^{o}C to -196^{o}C were

performed as a function of mechanical in-plane strain levels. The apparatus was excellent enough to generate cracks related to the in-plane stresses (or strains) on plies.

The upper 90^o ply under thermo-cycling combined with bending was proved to be the optimal layer to monitor crack densities considering a combined large temperature difference thermal cycling plus mechanical loading. The upper 90^o layer was proved to be under tensile stress which is a dominant condition initiating matrix transverse cracking, considering both the in-plane stresses by bending and the high temperature cure induced thermal residual stress conditions. A 2^k factorial design was applied to determine the principal factors and their interactions from thermo-cycling temperature profiles, number of cycles, pre-mechanical loading conditions, and heating rates for microcrack development.

8.3 Results and Conclusions

From the free edge and half sectioned crack density observations, the thermo cycling profiles was the most important factor causing microcracking. The number of cycles was the second most important factor causing damage related to the cyclic thermal stress.

The damage modes include initiation and propagation. The modes can be explained both at an initial thermal cycle condition and an increased number of cycles one under the three different thermo-cycling temperature profiles.

1) Conclusions obtained after the initial thermal exposure are as follows.

- Cryogenic thermo-cycling

- The high temperature difference induced thermal residual stresses during cryogenic thermo-cycling was found to affect microcrack formation by the thermal expansion mismatch in both fiber/matrix and adjacent plies of a laminate.
- Micrographs showed the interfacial initial cracking at -196^{o}C.

- High temperature thermo-cycling
  - Microcracks were initiated at the fiber-matrix interface during high temperature cycling. The ductile matrix having both the strength and modulus reduction at high temperature induced the interface failure.
  - The transverse loading combined with the matrix strength modulus reduction at high temperatures made the composite easer to have the interfacial debonding.
- Cryogenic and high temperature combined thermo-cycling
  - Initial crack sites by thermal expansion mismatch at cryogenic temperature grow at high temperature and high temperature itself induces additional interface initial cracking. This combined thermo-cycling causes accelerated damage.
  - Combined cryogenic and high temperature thermo-cycling was the most severe thermo-cycling condition.

2) Modulus, thermal expansion coefficient, and strength degradation associated with the accumulated cracks helped further cracking with an increasing number of thermo-cycles. These three factors associated with the existing microcracks also helped lead to further

cracking with an increasing number of thermo-cycles. Brief conclusions made from the experiment with an increasing number of thermo-cycles are as follows.

- Cryogenic thermo-cycling
    - Thermal fatigue with the matrix's lower toughness condition at the cryogenic temperature accelerated the crack propagation through the matrix.
- High temperature thermo-cycling
    - The initial interfacial failure at the high temperature does not appear to propagate through the matrix as fast as in the case of cryogenic thermo-cycling.
    - The thermal fatigue effect still gives the initial interfacial failure a chance to propagate through the matrix when it is combined with mechanical transverse stresses.
- Cryogenic and high temperature combined thermo-cycling
    - The subsequent exposure to higher thermal residual stresses at the cryogenic temperatures after the interfacial failure at the high temperatures resulted in cracks propagating faster and the highest temperature difference induced thermal fatigue accelerated mirocracking.

The viscoelastic relaxation effect at high temperature does not seem to significantly affect the crack density considering no drastic crack density differences between higher (4^{o}C/min) and lower(1^{o}C/min) heating rate condition under thermo-cycling.

REFERENCES

1. Amatore, D. (1998). First Major X-33 Component Arrives, *Aerospace Technology Innovation,* **6**(2):13-14.

2. Morgan, R. J., Li, D., Lu, J., Moon, S. and Ribeiro, R. (2002). Development and Characterization of Non-Autoclave Processes for Composites, In: *Proceedings of 47th International SAMPE Symposium*, May 10-14, Long Beach, CA, pp. 585-595.

3. Paillous , A. and Pailler, C. (1994). Degradation of Multiply Polymer-Matrix Composites Induced by Space Environment, *Composite*, **25**(4): 287-295.

4. Heydenreich, R. (1998), Cryotanks in Future Vehicles, *Cryogenics*, **38**(1): 125-130.

5. Vendroux, G., Auberon, M. and Dessaut, J. (1997). Cryogenic Composite Tanks: Structural Analysis and Manufacturing Concepts, In: *Proceedings of 42nd International SAMPE Symposium*, May 4-8, Long Beach, CA, pp. 828-838.

6. Kessler, S., McManus, H. and Matuszeski, T. (2001). The Effects of Cryocycling on the Mechanical Properties of IM7/977-2, In: *Proceedings of the American Society for Composites*, September 12-14, Blacksburg, VA, pp. 93-111.

7. Stokes, E. S., Shin, E. E. and Sutter, J. K. (2002). Mechanical Testing of PMCs under Simulated Rapid Heat-Up Propulsion Environments (I. Temperature Measurement), In: *Proceedings of 47th International SAMPE Symposium*, May 10-14, Long Beach, CA, pp. 356-370.

8. Hahn, H. T. and Pagano, N.J. (1975). Curing Stresses in Composite Laminates, *Journal of Composite Materials*, **9**:91-106.

9. Hahn, H. T. (1976), Residual Stresses in Polymer Matrix Composite Laminates, *Journal of Composite Materials*, **10**:266-278.

10. Tsotsis, T.K. and Lee, S.M. J. (1998). Long Term Thermo-Oxidative Aging in Composite Materials: Failure Mechanism, *Composite Science and Technology*, **58**:355-368.

11. Shin, E. E., Morgan, R. J., Zhou, J., Sutter, K. and Meador, M.A. (1999), High Temperature Polymer Matrix-Carbon Fiber Composites – Critical Degradation Mechanisms and Test Methodologies, In: *Proceedings of 44th International SAMPE Symposium*, May 23-27, Long Beach, CA, pp. 2382-2396.

12. Nizar, K., Laurent M. and Epiphane R. (1999). Temperature Effect on the Damage Development of a CFRP Laminate under Cyclic Loading, In: *Proceedings of the 12th International Conference on Composite Materials*, July 5-9, Paris, France, pp. 960-965.

13. Owens, G. A. and Schofield, S.E. (1988). Thermal Cycling and Mechanical Property Assessment of Carbon Fiber Fabric Reinforced PMR-15 Polyimide Laminates, *Composite Science and Technology*, **33**:177-190.

14. Eggers, H., Hartung, W. and Knaak, S. (1991). Damage in Carbon Fiber Reinforced Epoxy after Thermal Cycling and T-Fatigue Loading, *Cryogenics*, **31**:265-268.

15. Ahlborn, K. (1991), Durability of Carbon Fiber Reinforced Plastics with Thermoplastic Matrices under Cyclic Mechanical and Cyclic Thermal Loads at Cryogenic Temperatures, *Cryogenics*, **31**:257-260.

16. Park, C. H. and McManus, H. L. (1996). Thermally Induced Damage in Composite laminates: Predictive Methodology and Experimental Investigation, *Composite Science and Technology*, **56**:1209-1219.

17. Reynolds, T.G. and McManus, H. L. (1998). Understanding and Accelerating Environmentally Induced Degradation and Microcracking, In: *AIAA/ASME/ASCE/AHS/ASC Structure, Structural Dynamics, and Materials Conference and Exhibition,* April 23-25, Long Beach, CA, pp. 2106-2113.

18. Baschek, G. and Hartwig, G. (1998). Parameters Influencing the Thermal Expansion of Polymers and Fibre Composite, *Cryogenics*, **38**(1):99-103.

19. Biernacki, K., Szyszkowski, W. and Yannacopoulos, S. (1999). An Experimental Study of Large Scale Model Composite Materials under Thermal Fatigue, *Composites Part A: Applied Science and Manufacturing*, **30**:1027-1034.

20. Kobayashi, S., Terada, K. Ogihara, S. and Takeda, N. (2001). Damage-Mechanics Analysis of Matrix Cracking in Cross-Ply CFRP Laminates under Thermal Fatigue, *Composite Science and Technology*, **61**:1735-1742.

21. Shimokawa, T., Katoh, H., Hamaguchi, Y., Sanfongi, S. and Mizuno, H. (2002). Effect of Thermal Cycling on Microcracking and Strength Degradation of High-Temperature Polymer Composite Materials for Use in Next-Generation SST Structures, *Journal of Composite Materials*, **36**(7): 885-895.

22. Henaff-Gardin, C. and Lafarie-Frenot, M.C. (2002). Specificity of Matrix Cracking Development in CFRP Laminates under Mechanical or Thermal Loadings, *International Journal of Fatigue*, **24**:171-177.

23. Timmerman, J.F., Tillman, M.S., Hayes, B.S. and Seferis, J.C. (2002). Matrix and Fiber Influences on the Cryogenic Microcracking of Carbon Fiber/Epoxy Composites, *Composites Part A: Applied Science and Manufacturing*, **33**:323-329.

24. Bechel, V. T., Fredin, M.B., Donaldson, S.L., Kim, R.Y. and Camping, J.D. (2003). Effect of Stacking Sequence on Micro-Cracking in a Cryogenically Cycled Carbon/Bismaleimide Composite. *Composites Part A: Applied Science and Manufacturing*, **34**:663-672.

25. Bechel V.T. and Kim, R.Y. (2004). Damage Trends in Cryogenically Cycled Carbon/Polymer Composites, *Composite Science and Technology*, **64**:1773-1784.

26. Bechel V.T., Camping J.D. and Kim R.Y. (2005). Cryogenic/Elevated Temperature Cycling Induced Leakage Paths in PMCs, *Composites Part B: Engineering*, **36**:171-182.

27. Ray, B.C. (2005). Thermal Shock and Thermal Fatigue on Delamination of Glass-Fiber-Reinforced Polymeric Composites, *Journal of Reinforced Plastics and Composites*, **24**(1):111-116.

28. Kim, R. Y., Rice, B. P. and Donaldson, S. L. (2002). Microcracking in Composite Laminates under Thermal Environments: 150 to -196^{o}C, In: *Proceedings of 47th International SAMPE Symposium*, May 10-14, Long Beach, CA, pp.833-842.

29. Garmong, G., (1974). Elastic-Plastic Analysis of Deformation Induced by Thermal Stress in Eutectic Composites: I. Theory, *Metallurgical Transactions*, **5**:2183-2190.

30. Garmong, G., (1974). Elastic-Plastic Analysis of Deformation Induced by Thermal Stress in Eutectic Composites: II. Thermal Expansion, *Metallurgical Transactions*, **5**:2191-2196.

31. Ju, J. and Morgan, R.J. (2004). Characterization of Microcrack Development in BMI-Carbon Fiber Composite under Stress and Thermal Cycling, *Journal of Composite Materials*, **38**(22):2007-2024.

32. Steven, L.D. and Kim R.Y. (2002), Fatigue of Composite at Cryogenic Temperatures, In: *Proceedings of 47th International SAMPE Symposium*, Long Beach, May 10-14, CA, 1248-1253.

33. Noda,K., Takahara, A. and Kajiyama, T. (2001). Fatigue Failure Mechanism of Short Glass-Fiber Reinforced Nylon 66 Based on Nonlinear Dynamic Viscoelastic Measurements, *Polymer*, **42:** 5803-5811.

34. Ha, J.C., Yokobori, A.T. Jr. and Takeda, H. (1999). The Effect of Fatigue Damage on Toughening of Short-Fiber-Reinforced Polymer Composites, *Journal of Materials Science*, **34**(9): 2103-2111.

35. Li, Y., Tang, X., Miranda, J. A., Sue, H. and Witcomb, J. D. (2000). Damage in Hygrothermally Aged Hybrid IM7/BMI Composites, In: *Proceedings of the American Society for Composites*, 15th Annual Technical Conference, September 24-27, College Station, TX, pp. 558-566.

36. Gautier, L., Mortaigne, B. and Bellenger V. (1999). Interface Damage Study of Hydrothermally Aged Glass-Fiber-Reinforced Polyester Composites, *Composites Science and Technology*, **59**(16): 2329-2337.

37. Pipes, B.R., Vinson, J.R. and Chou, T.W. (1976). On the Hygrothermal Response of Laminated Composite Systems, *Journal of Composite Materials*, **10**:129-148

38. Li, Y., Miranda, J. and Sue, H.J. (2001). Hygrothermal Diffusion Behavior in Bismaleimide Resin, *Polymer*, **42**:7791-7799

39. Nairn, J. A. (1989). The Strain Energy Release Rate of Composite Microcracking – A Variational Approach, *Journal of Composite Materials*, **23**:1106-1129.

40. Fukunga, H. and Chou,T. (1984). Probabilistic Failure Strength Analyses of Graphite/Epoxy Cross-Ply Laminates, *Journal of Composite Materials*, **18**:339-356.

41. Sato, N., Kurauchi, T., Sato, S. and Kamigaito, O. (1984). Mechanism of Fracture of Short Glass Fiber-Reinforced Polyamide Thermoplastic, *Journal of Materials Science*, **19**: 1145-1152.

42. Sato, N., Kurauchi, T., Sato, S. and Kamigaito, O, (1991). Microfailure Behavior of Randomly Dispersed Short Fiber Reinforced Thermoplastic Composites Obtained by Direct SEM Observation, *Journal of Materials Science*, **26**: 3891-3898.

43. Renard, J., Favre, J. P. and Jeggy, T. (1993). Influence of Transverse Cracking on Ply Behavior: Introduction of a Characteristic Damage Variable, *Composite Science and Technology*, **46**: 29-37.

44. McCartney, L. N. (1993). The Prediction of Cracking in Bi-Axially Loaded Cross-Ply Laminates Having Brittle Matrixes, *Composites*, **24**(2): 84-92.

45. Henaff-Gardin, C., Lefarie-Frenot, M. C. and Gamby, D. (1996). Doubly Periodic Matrix Cracking in Composite Laminates Part 2: Thermal Biaxial Loading, *Composite Structure*, **36**: 131-140.

46. Chaoui, K., Chudnovsky, A. and Moet, A. (1987). Effect of Residual Stress on Crack Propagation in MDPE Pipes, *Journal of Materials Science*, **22**: 3873-3879.

47. Nairn, J.A. (1997). Fracture Mechanics of Composites with Residual Thermal Stresses, *Journal of Applied Mechanics*, **64**:804-815.

48. Peters, P. W. M. and Andersen, S. I., (September 1989). The Influence of Matrix Fracture Strain and Interface Strength on Cross-Ply Cracking in CFRP in the Temperature Range of -100^{o}C to +100^{o}C, *Journal of Composite Materials*, **23**:944-960.

49. Drzal, L.T., Rich, M. J. and Koenig, M. F. (1985). Adhesion of Graphite Fibers to Epoxy Matrices: III. The Effect of Hygrothermal Exposure, *Journal of Adhesion*, **18**(1): 49-72.

50. Biro, D.A., Plezier, G. and Deslandes, Y. (1993). Application of the Microbond Technique: Effects of Hygrothermal Exposure on Carbon-Fiber/Epoxy Interfaces, *Composite Science and Technology*, **46**:293-301.

51. Scola, D.A. (2002). *ASM Handbook Composites*, ASM International, Dayton, OH.

52. Shin, E.E., Sutter, J.K., Eakin H., Inghram L., McCorkle, L., Scheiman, D., Papadopoulos, D. and Kerze, F. (2002). Design and Fabrication Issues of High Temperature PMCS for Aerospace Propulsion Applications, In: *Proceedings of 47th International SAMPE Symposium*, May 10-14, Long Beach, CA, pp. 314-355.

53. Devore, J.L. and Farnum, N.R. (1999). *Applied Statistics for Engineering and Scientists*, Duxbury Press, Pacific Grove, CA.

54. Fisher, R.A. (1951). *Design of Experiments*, 6th edition, Oliver & Boyd, London.

55. Taguchi G. (1986). *Introduction to Quality Engineering*, Quality Resources, White Plains, New York.

56. Wroblewska, A., Rzepkowska M. and Milchert, E. (2004). Optimization of the Technological Parameters of Epoxidation of Allyl Alcohol by Hydrogen Peroxide over Ti-BETA Catalyst, *Journal of Chemical Technology and Biotechnology*, **79**:343-353.

57. Shih, I.L., Van, Y.T. and Chang Y.N. (2002).Application of Statistical Experimental Methods to Optimize Production of Poly(γ-glutamic Acid) by *Bacillus Licheniformis* CCRC 12826, *Enzyme and Microbial Technology*, **31**:213-220.

58. Chacon, M., Berges, L. Molpeceres, J., Aberturas, M.R. and Guzman, M. (1996). Optimized Preparation of Poly D,L (Lactic-Glycolic) Microspheres and Nanoparticles for Oral Administration, *International Journal of Parmaceutics*, **141**:81-91.

59. Gupta, V.K. Assmus, M.W., Beckert, T.E. and Price, J.C. (2001). A Novel pH- and Time-Based Multi-Unit Potential Colonic Drug Delivery System. II. Optimization of Multiple Response Variables, *International Journal of Parmaceutics*, **213**:93-102.

60. Baeten S. and Verpoest, I. (1999). Optimization of a GMT-Based Cold Pressing Technique for Low Cost Textile Reinforced Thermoplastic Composites, *Composites Part A: Applied Science and Manufacturing*, **30**:667-682.

61. McGarva, L.D. and Astrom, B.T. (1999). Experimental Investigation of Compression Molding of Glass/PA12-PMI Foam Core Sandwich Components, *Composites Part A: Applied Science and Manufacturing*, **30**:1171-1185.

62. Liu, S.-J. and Chen, Y.-S. (2004). The Manufacturing of Thermoplastic Composite Parts by Water-Assisted Injection-Molding Technology, *Composites Part A: Applied Science and Manufacturing*, **35**:171-180.

63. Cohen, D. (1997). Influence of Filament Winding Parameters on Composite Vessel Quality and Strength, *Composites Part A: Applied Science and Manufacturing*, **28**:1035-1047.

64. Dvir, H., Gottlieb, M., Daren, S. and Tartakovsky, E. (2003). Optimization of a Flame-Retarded Polyproplene Composite, *Composite Science and Technology*, **63**:1865-1875.

65. Sutherland L. S. and Soares, C. G. (2003). The Effects of Test Parameters on the Impact Response of Glass Reinforced Plastic Using Experimental Design Approach, *Composites Science and Technology*, **63**:1-18.

66. Russ, J.C. (2002), *The Image Processing Handbook*, 4th Edition, CRC Press, Boca Raton, FL.

67. Landis, E.N., Nagy E.N., Keane D.T. and Nagy G. (1999). Technique to Measure 3D Work-of-Fracture of Concrete in Compression, *Journal of Engineering Mechanics*, **125**:599-605.

68. Landis, E.N. and Nagy, E.N. (2000). Three-Dimensional Work-of-Fracture for Mortar in Compression, *Engineering Fracture Mechanics*, **65**:223-234.

69. Landis, E.N., Nagy, E.N. and Keane, D.T. (2000). Microstructure and Fracture in Three Dimensions, *Engineering Fracture Mechanics*, **70**:911-925.

70. Muller, M., Toussaint, E., Destrebecq, J. and Grediac, M. (2004). Experimental and Numerical Study of Reinforced Concrete Specimens Strengthened with Composite Plates, *Composites Part A: Applied Science and Manufacturing*, **35**:885-893.

71. Chermant J., Boitier, G., Darzens, S., Coster, M. and Chermant, L. (2001). Damage Morphological Parameters, *Image Analysis and Stereology*, **20**:207-211.

72. Shen, C. and Springer, G.S. (1976). Moisture Absorption and Desorption of Composite Materials, *Journal of Composite Materials*, **10**:2-20.

73. Apicella, A., Tessieri, R. and de Cataldis, C. (1984). Sorption Modes of Water Glassy Epoxies, *Journal of Membrane Science*, **18**: 211-225.

74. Roy, S. and Xu, W. (2001). Modeling of Diffusion in the Presence of Damage in Polymer Matrix Composite, *International Journal of Solids and Structures*, **38**:115-125.

75. Roy, S., Xu, W., Patel, S. and Case, S. (2001). Modeling of Moisture Diffusion in the Presence of Bi-Axial Damage in Polymer Matrix Composite Laminates, *International Journal of Solids and Structures*, **38**:7627-7641.

76. Gentz, M., Armentrout, D., Rupnowski, P., Kumosa, L., Shin, E., Sutter, J. K. and Kumosa, M. (2004). In-Plane Shear Testing of Medium and High Modulus Woven Graphite Fiber Reinforced/Polyimide Composites, *Composite Science and Technology*, **64**:203-220.

77. Gentz, M., Benedikt, B., Sutter, J. K. and Kumosa, M. (2004). Residual Stresses in Unidirectional Graphite Fiber/Polyimide Composites as a Function of Aging, *Composite Science and Technology*, **64**:1671-1677.

78. Zhou, Y. and Xia, Y. (2001). In Situ Strength Distribution of Carbon Fibers in Unidirectional Metal Matrix Composites Wires, *Composite Science and Technology*, **61**:2017-2023.

79. Donnet J. B. (1998). *Carbon Fibers*, 3rd Edition, Marcel Dekker, New York.

80. Rupnowski, P., Gentz, M., Sutter, J. K. and Kumosa, M. (2005). An Evaluation of the Elastic Properties and Thermal Expansion Coefficient of Medium and High Modulus Graphite Fibers, *Composites Part A: Applied Science and Manufacturing*, **36**:327-338.

81. Timoshenko, S. P. (1953). *History of Strength of Materials*, McGraw-Hill, New York.

82. Reddy, J. N. (2004). *Mechanics of Laminated Composite Plate: Theory and Analysis*, 2nd Edition, CRC Press, Boca Raton, FL.

83. Reddy, J.N. (2002). *Energy Principles and Variational Methods in Applied Mechanics*, 2nd Edition, John Wiley & Sons, Inc, New York.

84. Schapery, R. A. (1966). An Engineering Theory of Nonlinear Viscoelasticity with Applications, *International Journal of Solids and Structures*, **2**:407-425.

85. Pagano, N. J., Schoeppner, G. A., Kim, R. and Abrams, F. L. (1998). Steady-State Cracking and Edge Effects in Thermo-Mechanical Transverse Cracking of Cross Ply Laminates, *Composite Science and Technology*, **58**:1881-1825.

86. Gao, F., Boniface, L., Orin, S. L., Smith, P. A. and Greaves, R. P. (1999). Damage Accumulation in Woven-Fabric CFRP Laminates under Tensile Loading: Part 1. Observations of Damage Accumulation, *Composite Science and Technology*, **59**:123-136.

87. Karandikar, P. and Chou, T. W. (1993). Characterization and Modeling of Microcracking and Elastic Moduli Changes in NICALON/CAS Composites, *Composite Science and Technology*, **46**:253-263.

88. Drukker, E., Green, A. K. and Marom, G. (2003). Mechanical and Chemical Consequence of Through Thickness Thermal Gradients in Polyimide Matrix Composite Materials, *Composites Part A: Applied Science and Manufacturing*, **34**:125-133.

89. Morgan, R.J., Shin, E. E. and Lincoln, J. E., (2002). Thermal Properties of High Temperature Polymer Matrix Fibrous Composites, in *Handbook of Thermal Analysis and Calorimetry*, *Vol.3: Applications to Polymers and Plastics*, Cheng, S.Z.D., Elsevier Science, New York, pp. 491-518.

90. Chen, T. (2000). Determining a Prony Series for a Viscoelastic Material from Time Varying Strain Data, NASA/TM-2000-210123, NASA Langley Research Center, Hampton, VA.

91. Aicher, S. and Klock, W. (2001). Linear Versus Quadratic Failure Criteria for Inplane Loaded Wood Based Panels, *Otto-Graf-Journal*, **12**:187-199.

92. Bowman, C.L., Sutter, J.K., Thesken, J.C. and Rice, B.P. (2001). Characterization of Graphite Fiber/Polyimide Composites for RLV Applications, In: *46th International SAMPE Symposium*, May 6-10, Long Beach, CA, pp. 1515-1520.

93. Vidal-Steif, M.H., Lancin, M., Valle, R., Raviart, J.L., Daux, J.C. and Rabinovitch, M. (1999). On the Role of Brittle Interfacial Phases on the Mechanical Properties of Carbon Fiber Reinforced Al-Base Matrix Composites, *Materials Science and Engineering A*, **272**:321-333.

94. Ahlborn, K. and Knaak, S. (1988). Cryogenic Mechanical Behavior of a Thick-Walled Carbon Fiber Reinforced Plastic Structure, *Cryogenic*, **28**:273-277.

95. Kim, R.Y. (1988). Fatigue behavior, In: Tsai, S. W., Editor, *Composite Design,* Technomic Publication, Dayton, OH, pp. 195-197.

96. Whitley, K.S. and Gates, T.S. (2003). Thermal/Mechanical Response of a Polymer Matrix Composite at Cryogenic Temperature, NASA/TM-2003-212171, NASA Langley Research Center, Hampton, VA.

97. VanLandingham, M.R., Dagastine P.R., Eduljee. R.F., McCullough, R. L. and Gillespie, J.W.Jr., (1999). Characterization of Nanoscale Property Variations in Polymer Composite System: 1. Experimental Results, *Composites Part A: Applied Science and Manufacturing*, **30**:75-83.

98. Bogetti, T.A., Wang, T., VanLandingham, M.R. and Gillespie, J.W.Jr. (1999). Characterization of Nanoscale Property Variations in Polymer Composite Systems: 2. Numerical Modeling, *Composites Part A: Applied Science and Manufacturing*, **30**:85-94.

99. Hashin, Z. (1985). Analysis of Cracked Laminates: A Variational Approach, *Mechanics of Materials*, **4**:121-136.

100. Narin, J.A. and Hu, S. (1992). The Formation and Effect of Outer-Ply Microcracks in Cross-Ply Laminates: A Variational Approach, *Engineering Fracture Mechanics*, **41**(2):203-221.

101. Fox, B. L., Hodgkin, J. H., Jar, B., Lowe, A. and Morton, T. C. (1999). Isothermal Ageing of An Advanced High Temperature Carbon Fiber Composite. In: *ICCM12, 12th International Conference on Composite Materials*, July 5-9, Paris, France, pp. 94-102.

102. Otieno-Alego, V., Creagh, D., Jar. B., Fox, B. L. and Lowe, A. (2001). Characterization of the Moisture Adsorption and Thermal Ageing Behavior of Polymeric Composite Systems Using Raman Spectroscopy. In: Mallinson, B., Editor, *Ageing Studies and Lifetime Extension of Materials*, Kluwer/Plenum Press, Dordrecht//New York, pp. 113-122.

103. Bowels, K.J. Papadopoulos, D.S., Inghram, L.L., McCorkle, L.S. and Klan, O.V, (2001). Long Time Durability of PMR-15 Matrix Polymer at 204, 260, 288 and 316^{o}C, NASA/TM-2001-210602, NASA Glenn Research Center, Cleveland, OH.

104. Jost, W. (1960). Diffusion in Solids, Liquids, Gases, Academic Press, New York.

105. Bao, L., Yee, A. F. and Lee, C. (2001). Moisture Absorption and Hygrothermal Aging in a Bismaleimide Resin, *Polymer*, **42**:7327-7333.

106. Wong, T. C. and Broutman, L. J. (1985). Moisture Diffusion in Epoxy Resins: Part I. Non-Fickian Sorption Processes, *Polymer Engineering and Science*, **25**:521-528.

107. Wu, J. C. and Peppas, N. A. (1993). Modeling of Penetrant Diffusion in Glassy Polymers with an Integral Sorption Deborah Number, *Journal of Polymer Science*, **31:**1503-1518.

108. Cai, L. W. and Weitsman, Y. (1994). Non-Fickian Moisture Diffusion in Polymeric Composites, *Journal of Composite Materials*, **28**:130-154.

109. Weisman, Y. (1987). Coupled Damage and Moisture Transport in Fiber Reinforced Polymeric Composites, *International Journal of Solids and Structures*, **23**:1003-1025.

110. Lundgren, J. E. and Gudmundson, P. (1999). Moisture Absorption in Glass Fiber/Epoxy Laminates with Transverse Matrix Cracks, *Composite Science and Technology*, **59**:1983-1991.

VITA

Name: Jaehyung Ju

Address: 116 Leemae-Dong, Sungji-APT 703-1207,
Sungnam City, Republic of Korea

Email Address: jaehyung@tamu.edu
jaehyung.ju@gmail.com

Education: B.S., Mechanical Engineering, Korea Aviation University, 1996
M.S., Mechanical Engineering, Korea University, 1998